(13)

SYNTHESIS AND CHARACTERIZATION OF NEW LAYERED MAIN GROUP - TRANSITION METAL OXIDES

by

DANIEL M. GIAQUINTA

B.A., Northwestern University, Evanston, Illinois
(1989)

SUBMITTED TO THE DEPARTMENT OF CHEMISTRY
IN PARTIAL FULFILLMENT OF THE REQUIREMENTS
FOR THE DEGREE OF DOCTOR OF PHILOSOPHY

at the

MASSACHUSETTS INSTITUTE OF TECHNOLOGY

February 1994

Signature of Author _____
Department of Chemistry
October 14, 1993

Certified by _____
Hans-Conrad zur Loye
Thesis Supervisor

Accepted by _____
Glenn A. Berchtold
Chairman, Departmental Committee on Graduate Students

This doctoral thesis has been examined by a Committee of the Department of Chemistry as follows:

Professor Mark S. Wrighton _____
Chairman

Professor Hans-Conrad zur Loye _____
Thesis Supervisor

Professor Moungi G. Bawendi _____

SYNTHESIS AND CHARACTERIZATION OF NEW LAYERED MAIN GROUP - TRANSITION METAL OXIDES

by

DANIEL GIAQUINTA

submitted to the Department of Chemistry on October 14, 1993,
in partial fulfillment of the requirements
for the Degree of Doctor of Philosophy in Chemistry

ABSTRACT

The preparation of new layered main group - transition metal oxides has been pursued through the modification of existing layered oxides and through the use of chemical concepts, specifically ionicity, to prepare new materials using rational methods. The materials were characterized structurally, using single crystal and polycrystalline X-ray diffraction and polycrystalline neutron diffraction. Magnetic characterization was performed using Mössbauer spectroscopy, magnetic susceptibility measurements, and magnetic neutron diffraction measurements.

The layered bismuth - transition metal oxide systems $Bi_2Fe_{4-x}Ga_xO_9$ and $Bi_2Fe_{4-x}Al_xO_9$ were structurally and magnetically characterized to study the chemistry of site-specific substitution in layered magnetic systems. The new ordered compound $Bi_2Fe_2Mn_2O_{10}$ was prepared and the single crystal

structure is reported as an example of successful site-specific substitution through the modification of an existing layered material.

The materials $InMnO_3$ and $InFeO_3$, compounds with a previously unreported transition metal oxide structure, were prepared and characterized both structurally and magnetically. The solid solution $InMn_{1-x}Fe_xO_3$ was prepared in order to study the magnetic effects of systematic variation between the parent compounds $InMnO_3$ and $InFeO_3$.

Ionicity concepts were used in order to prepare a predictive method for structure-types in the ABO_3 phase diagram. This method successfully delineated the different structural regions in the ABO_3 phase diagram and aided in the preparation of new materials and structures.

Thesis Supervisor: Dr. Hans-Conrad zur Loye

Title: Paul Cook Career Development Professor of Chemistry

ACKNOWLEDGMENTS

I would like to thank my advisor, Hanno zur Loye, for giving both financial support and the freedom to pursue various areas of research which may not have been originally planned. I would also like to thank the zur Loye group, especially Tu, for instruction on the precession camera.

Special thanks go to Georgia Papeafthymiou for collecting and interpreting all of my Mössbauer spectroscopy and for helpful conversations during orals. Professor John Greedan was very helpful during the collection and interpretation of all neutron diffraction experiments. Thanks to Professor Bernie Wuensch for several very informative conversations concerning precession photography and crystallography in general. Most of all, mucho thanks and indebtedness to Bill Davis for instruction and patience and beers during all my time in the X-ray Lab. Evenings at the Muddy with Mike, Jen, Neil and Erica were enjoyed. Thanks to mom and dad for love and support even though sometimes my letters home were few and far between, and to Peter, Shashi, Mr. Buh and Mayu.

Finally, thanks, appreciation and love to Chris for putting up with me when I was irritating, waking me up in the morning and for cleaning the apartment more than I did. Without you the last four years would certainly have been dreary.

To Christine

"I have no data yet. It is a capital mistake to theorize before one has data. Insensibly one begins to twist facts to suit theories, instead of theories to suit facts.

-- A Scandal in Bohemia, from The Adventures of Sherlock Holmes, by Sir A. Conan Doyle

For page count only

TABLE OF CONTENTS

LIST OF FIGURES

CHAPTER 2

CHAPTER 4

LIST OF TABLES

CHAPTER 2

CHAPTER 1

INTRODUCTORY CONCEPTS IN THE STUDY OF LAYERED MAIN GROUP - TRANSITION METAL OXIDES

Section 1.1: Introduction

The rational design of technologically useful materials requires an understanding of the interrelations between crystal structure, chemical composition, and physical properties. Specifically, the preparation of advanced materials relies on the study of the basic composition-structure and structure-property relationships of binary, ternary, and quaternary compounds and the ability to use this basic information in the study of applied problems. The work in this thesis can best be summarized as the study of several problems posed by the preparation of advanced materials with predictable properties, including crystal chemistry, site-specific substitution, structure-property relationships of low dimensional structures, and methods for structural prediction. Chapter 1 describes basic introductory concepts necessary for the study of site-specific substitution, structural prediction and the chemical modification of known structures. Solid state techniques used in the following chapters are discussed including synthesis and characterization methods common to the research described in Chapters 2 and 3. Chapter 2 describes site-specific substitutions within the $Bi_2M_4O_{9+\delta}$ system, where M = Al, Fe, Ga, and Mn. The structural and magnetic features of the $Bi_2M_4O_{9+\delta}$ system are described as the magnetic interactions of the parent compound are modified by the substitution of diamagnetic elements. Chapter 3 describes the structural and magnetic characterization of two previously unreported materials, $InMnO_3$ and $InFeO_3$, and their solid solution $InMn_{1-x}Fe_xO_3$. In Chapter 4 the ABO_3 structural phase diagram is discussed and a new method for predicting the structure types of ternary oxides is introduced.

Crystal chemistry can be defined as the study of how the packing of atoms in natural and synthetic materials influences physical and chemical properties.[1] In other words, crystal chemistry is concerned with the discovery and the explanation of structure-property relationships in solids. An important link between a given structure and the properties of a compound having this structure is the nature of the bonding interactions. A pure covalent bond can be formed only between atoms of equal electronegativity; therefore, the bonding in metal-oxygen compounds is, by necessity, of mixed ionic-covalent character, which is evident in the structural and magnetic properties exhibited by many oxides.[1] Additional contributions from lattice and crystal-field stabilization energies result in properties, such as magnetic ordering and metallic electrical conductivity, that are difficult to model and to predict, particularly in complex structures. Consequently, improving our understanding of crystal chemistry is eminently important to current fields of applied solid state research, such as the preparation of new high-temperature superconducting materials[2,3] as well as the device materials research of the semiconductor industry.[4]

A. Site-specific substitution

The tailoring of advanced materials with predictable properties relies on the ability to substitute a desired element directly into a specific crystallographic site. Substitution chemistry of this nature is described in Chapter 2. Theoretically, coordination preferences can be generalized based on size, oxidation state, and electronegativity of the substituent element. In practice, however, the chemistry of site-specific substitution remains largely experimental in nature. In compounds with several inequivalent cation coordination sites, substitution experiments afford the only means for

ascertaining which elements can be inserted into a certain site. The $Bi_2M_4O_9$ system, where M = Al, Fe, Ga, and Mn, (Chapter 2), has been investigated to improve our understanding of the crystal chemistry of structure types that contain both octahedral and tetrahedral cation coordination sites. Substitutions of both main group and transition metals into the octahedral and tetrahedral coordination sites were performed to study the effects of site-specific substitution in a complex magnetic system.

B. Structural prediction

The rational design of materials also requires an understanding of the correlation between basic crystal chemistry and simple structure-property relationships. Implicit in such a relationship is an understanding of the connection between chemical composition and crystal structure in solid state materials. This seemingly simple relationship has been addressed, with varying success, by a number of workers[5-23] who have used parameters such as electronegativity, radii, valence electron count, and principal quantum number, to establish this link between structure types and atomic properties for different classes of materials. Establishing such a link is particularly difficult due to the large number of parameters which affect structures, *e.g.* the charge and coordination preference of metals, the existence of energetically close-lying structure types, as well as synthetic parameters such as temperature. The use of high pressure or low temperature synthesis further complicates the problem because of kinetic considerations and the synthesis of metastable phases. Numerous attempts have been made to correlate structural stability with chemical or physical variables derived from atomic properties of the constituent elements. For different classes of materials, different atomic properties must be used to achieve good

correlation.[24] Chapter 4 describes the formulation of a new method of structural prediction in which several old concepts, size and ionicity, were combined for the first time. This new method has certain advantages over the use of either concept alone. The utility of this new method for segregating similar structures is demonstrated and an explanation of exceptions is provided. In addition, using this method, predictions for previously unreported structures and stoichiometries are presented.

C. Chemical modification of existing structures

Often the preparation of new materials is driven by the desire to improve the properties of known materials. For example, superconductors contain layered structures and copper-oxygen planes.[3] Generally, structurally related compounds with multiple copper oxide planes display higher transition temperatures than compounds with a single copper-oxygen plane. Consequently, approaches for the preparation of new superconductors have often concentrated on the chemical modification of familiar structure types by the addition of copper-oxygen layers. Rational synthesis of this type may be aided by the use of basic radius-ratio rules and existing phase diagrams. Synthesis of new materials with previously unreported structures, however, is more difficult.

An easier approach by which to discover new properties in a somewhat predictable fashion is through the preparation of solid solutions. The systematic variation of known materials and the characterization of changes which occur with substitution provide a pathway through which basic structure-property relationships may be understood. Only by understanding composition-structure and structure-property relationships can the rational

design of materials with desirable properties may achieved. Both Chapters 2 and 3 discuss the systematic variation of materials through the preparation of solid solutions.

Section 1.2: Experimental methods

A Synthetic techniques[25,26]

1. Polycrystalline samples

The choice of methods used for the synthesis of materials with extended structures has a great deal of influence on the resulting stoichiometry and structure. Solid state reactions, the direct reaction of a stoichiometric mixture of solid starting materials, are commonly used for preparation of polycrystalline samples. The limiting factor for a solid state reaction is the interdiffusion of solid starting materials until intimate contact of reactants is achieved. Although rapid initially, further reaction goes more slowly as the product layer grows and diffusion lengths increase. Since the reaction rate is limited by solid-solid diffusion, high temperatures (800°C or higher) are necessary. Consequently, the major products are often the most thermodynamically stable phase of a given system. Because of the extreme differences between room temperature and the temperatures often used in solid state synthesis, metastable or kinetic phases may be stable at room temperature but difficult to prepare by standard methods. Often metastable phases have interesting structures and properties, *e.g.* $YBa_2Cu_3O_{6+\delta}$. In order to synthesize kinetic phases sometimes other synthetic techniques must be employed.

The use of precursor methods are one way in which the high temperatures associated with solid state reactions may be avoided.[27] For example, in the solid state preparation of $ZnFe_2O_4$, temperatures on the order of 1000°C must be used to cause the binary oxide starting materials to react. Molecular mixing of oxalate precursors may be achieved by dissolving zinc and iron oxalates in water and gradually evaporating the solution. By this route, homogeneous precipitates of mixed zinc and iron oxalates are obtained. Such intimate mixing produces shorter diffusion lengths and the product can be prepared at significantly lower temperatures.

2. *Single crystals*

Single crystals can be prepared using fluxes of molten salts or molten metals. Flux crystallization, or crystallization from a high temperature solution, utilizes the advantages of solution mixing for materials that would be solids at ambient temperatures. Vapor phase transport employs the advantages of the gas phase in the preparation of solids. Electrolysis within molten salts may be used to prepare both single and polycrystalline samples. This method has several advantages over flux crystallization. Crystals grown using an electrochemical gradient instead of a temperature gradient may be of extremely high quality. Another advantage of electrolysis is the accessibility of unusual oxidation states. Since the product is formed directly at the cathode or anode, materials may be crystallized in extremely oxidized or reduced states without resorting to harsh techniques to reach highly oxidizing or reducing conditions.

2. *Measurement techniques*

The tools necessary for the study of the important properties of solids with extended structures *vide supra* must allow the researcher to distinguish between the gross structural features of the material in question and the more subtle features of bonding that contribute to variations in coordination geometries, variation in bond lengths and angles, and the variations of properties between isostructural materials. An example from *Crystal Chemistry and Refractivity* by Jaffe,[1] describes the differences between structure and bonding which must be interpreted if the types of experiments described in this thesis are to provide the researcher with useful information. Aluminum oxide, α-Al_2O_3, (corundum) and iron oxide, Fe_2O_3, (hematite) both crystallize in the corundum structure. Both aluminum(III) and iron(III) are in octahedral coordination with similar but relatively small ionic radii for 6-fold coordination, 0.53 and 0.64Å, respectively. The smaller Al^{3+} ion reduces the volume of the AlO_6 octahedron with respect to the FeO_6 octahedron of hematite. Aluminum uses $3s^23p^1$ orbitals to bond to oxygen in corundum, whereas iron uses $4s^23d^1$ orbitals to bond to oxygen in hematite. The colorless, completely transparent nature of pure corundum, compared with the deep red, poorly transparent, almost metallic nature of hematite suggests that $3d$ orbitals of Fe^{3+} form π bonds with the unused p-orbitals of oxygen in hematite. The properties of two materials crystallizing in the same structure-type might be expected to be similar, but in fact are very different. For corundum and hematite, the packing of atoms in space--the crystal structure--may be very similar but the bonding--the physical and chemical properties--is very different. Different probes are necessary to elucidate the effects of structure and bonding.

Structural analysis, particularly single-crystal structure determination can provide information directly about many features which are of interest to the experimental solid state chemist. Structural analysis can give information about the gross features of bonding: coordination geometries, bond lengths and angles, *i.e.* the manner in which the component elements of the structure are packed. Single crystal structures, however, will not directly provide any information on why a certain structure crystallizes for a given stoichiometry or why certain layered copper oxides display superconducting behavior. Analysis of the magnetic structure can complement the basic crystal structure by providing information about bonding through an interpretation of the magnetic ordering. Together, structural and magnetic analysis allows for full characterization of a given material.

Conclusions

Transition metal oxides are a technologically important class of materials. The substitution chemistry of such materials, however, is largely experimental in nature. Through exploratory chemistry based on the systematic variations of known and new materials, the composition-structure and structure-property relationships of transition metal oxides may be understood. Obtaining this type of understanding is imperative for preparation of materials with predictable, technologically useful properties. The work in this thesis describes such exploratory research concerning problems of crystal chemistry, including site-specific substitution, structure-property relationships, and structural prediction.

References

(1) Jaffe, H. W. *Crystal Chemistry and Refractivity;* Cambridge University Press: Cambridge, 1988.

(2) Goodenough, J. B.; Manthiram, A. In *Chemistry of High Temperature Superconductors;* C. N. R. Rao, Ed.; World Scientific Publishing Co.: Singapore, 1991; pp. 1.

(3) Yvon, K.; François, M. Z. Phys. B. - Condensed Matter (1989) **76,** 413 and references therein.

(4) *The Chemistry of the Semiconductor Industry;* Moss, S. J.; Ledwith, A., Ed.; Blackie: London, 1987.

(5) Adams, D. M. *Inorganic Solids;* John Wiley & Sons: London, 1974; Vol. Ch. 5 p.105.

(6) Brewer, L. Science (1968) **161,** 115.

(7) Goldschmidt, V. M. Mat.-Naturv. Kl. (1926) **2,** 117.

(8) Gorter, E. W. J. Solid State Chem. (1970) **1,** 279.

(9) Hume-Rothery, W. *Electrons, Atoms, Metals and Alloys;* 3rd ed.; Dover: New York, 1963.

(10) Laves, F. *Theory of Alloy Phases;* American Society for Metals: Cleveland, 1955; Vol. p. 124.

(11) Mooser, E.; Pearson, W. B. Acta Crystallogr. (1959) **12**, 1015.

(12) Phillips, J. C.; Van Vechten, J. A. Phys. Rev. B (1970) **2**, 2147.

(13) Phillips, J. C. Rev. Mod. Phys. (1970) **42**, 317.

(14) Roth, R. S. J. Research NBS (1957) **58**, 75.

(15) Van Vechten, J. A. Phys. Rev. (1969) **187**, 1007.

(16) Van Vechten, J. A.; Phillips, J. C. Phys. Rev. B (1970) **2**, 2160.

(17) Villars, P. J. Less Common-Met. (1986) **119**, 175.

(18) Villars, P.; Hulliger, F. J. Less-Common Met. (1987) **132**, 289.

(19) Villars, P. J. Less Common-Met. (1984) **102**, 199.

(20) Villars, P. J. Less-Common Met. (1984) **99**, 33.

(21) Villars, P. J. Less-Common Met. (1983) **92**, 215.

(22) Villars, P.; Mathis, K.; Hulliger, F. In *Structures of Binary Compounds*; F. de Boer and D. Pettifor, Ed.; North-Holland: Amsterdam, 1989; Vol. 2; pp. 1.

(23) Villars, P.; Phillips, J. C.; Rabe, K. M.; Brown, I. D. Ferroelectrics (1992) **130**, 129.

(24) Kiselyova, N. N. MRS Bulletin (1993) **18**, 40.

(25) *Solid State Chemistry: Techniques*; Cheetham, A. K.; Day, P., Ed.; Oxford University Press: Oxford, 1987.

(26) West, A. R. *Solid State Chemistry and its Applications*; John Wiley & Sons Ltd.: New York, 1984.

(27) Horowitz, H. S.; Longo, J. M. Mat. Res. Bull. (1978) **13**, 1359.

CHAPTER 2

SITE-SPECIFIC SUBSTITUTION WITHIN THE $Bi_2Fe_{4-x}M_xO_{9+\delta}$ SYSTEM, M = Al, Ga, Mn

Section 2.1: Introduction

Layered bismuth transition metal oxides (LBTMOs), such as the Aurivillius phases[1-3] and many high T_c superconductors,[4-9] have attracted attention because of their electronic and magnetic properties. LBTMOs are also known to be oxygen ion conductors including doped members of the Aurivillius family[10] and several brownmillerite and Aurivillius-related intergrowth compounds.[11-13] The Aurivillius phases are a family of ferroelectrics[14-16] with the potential for superconductivity,[17] while a number of layered bismuth copper oxides and the analogous thallium compounds exhibit superconductivity with transition temperatures as high as 125K.[4,18] These systems contain transition metals in octahedral, tetrahedral and square pyramidal coordination geometries. The site-specific substitution study of layered systems with similar coordination sites is of interest in order to improve the properties of these technologically interesting systems through doping.

LBTMOs are of interest not only because of the novelty of superconductivity, but because of their unique and complex magnetic behavior,[19,20] often caused by structural and magnetic two-dimensionality. The size difference between bismuth and the first row transition and main group metals often promotes segregation of bismuth atoms from the transition and smaller main group metals within a given structure *via* the formation of Bi-O structural units *e.g.* sheets that separate transition metal oxide motifs, such as the perovskitic regions in the Aurivillius compounds and planar CuO_2 regions in the superconducting bismuth copper oxides. The structural segregation thus creates two-dimensional structures. Low-dimensional properties are

necessarily related to low-dimensional bonding and systems with structures resulting from the stacking of slabs or chains often display unique properties, such as low-dimensional magnetism, charge density waves, and superlative conductivity properties. Layered structures often display such properties since, due to the high anisotropy present in the chemical bonding, the properties themselves also display a high degree of anisotropy as well.[21] Because the bismuth oxide units are diamagnetic and not electronically conductive, both magnetic and electronic communication through the Bi-O units is limited or nonexistent. Consequently, the magnetic and electronic characteristics of the transition metal-oxide region are dimensionally limited, effecting interesting properties that are often low-dimensional in nature.

One structure-type with pronounced structural stacking is the family $Bi_2M_4O_9$ M = Fe, Mn, Al, and Ga.[22-24] This structure contains bismuth oxide planes that sandwich a metal oxide slab consisting of two cation coordination sites. The metal oxide cation coordination sites, octahedral and tetrahedral, can accept both transition and main group metals. This chapter describes the study of the magnetic interactions that arise *via* a superexchange mechanism, which couples the octahedral and tetrahedral sites. A systematic examination of $Bi_2M_{4-x}M'_xO_9$-type solid solutions was performed in order to elucidate how the metal-metal interactions effect the observed complex magnetic behavior, as well as to ascertain if the observed magnetic properties can be systematically altered through elemental substitutions.

The chemistry of the $Bi_2M_{4-x}M'_xO_9$-type structure is of interest as an example of site-specific substitution in a layered material with both octahedral and tetrahedral cation coordination sites. Structure-property relationships of the transition metal oxide structural unit and the complicated magnetism of this

system were investigated by substituting diamagnetic elements, in this case aluminum and gallium, for the magnetic element, iron. In this way, the integrity of the parent structure was maintained while the magnetic properties of the transition metal oxide region were probed by measuring the differences in the magnetic behavior between the parent compound, $Bi_2Fe_4O_9$, and the substituted solid solution phases, $Bi_2Fe_{4-x}M_xO_9$, M = Al, Ga.

The metal oxide region in the $Bi_2Fe_{4-x}M_xO_9$ structure containing the octahedral and tetrahedral sites is related structurally to the previously studied solid solution, $Ga_{2-x}Fe_xO_3$ ($0 \leq x \leq 1.6$).[25] The structure of $(Ga,Fe)_2O_3$ is a 3D array consisting of two octahedrally and two tetrahedrally coordinated metal atoms.[25-27] Although the transition metal regions in these two structures are similar, the Bi-O sheets in $Bi_2M_4O_9$ create an essentially two-dimensional structure. It is therefore of interest to make comparisons between the electronic and magnetic properties of the solid solutions, $Bi_2Fe_{4-x}Ga_xO_9$, which has not been investigated, and $Ga_{2-x}Fe_xO_3$, which has been studied extensively since the first structural and magnetic characteristics were reported in 1960.[25,28]

The ability to tailor the properties of advanced materials often relies on the ability to substitute a specific element directly into a specific crystallographic site. Coordination preferences may be generalized based on size, oxidation state, and electronegativity; however, the chemistry of site-specific substitution remains largely experimental in nature. Substitution experiments in compounds with several different cation coordination sites are useful for determining which elements may be substituted into a certain coordination site. The solid solution $Bi_2M_{4-x}M'_xO_{9+\delta}$, with the $Bi_2M_4O_{9+\delta}$ structure, M, M' = Fe, Ga, and Mn,[29,30] specifically lends itself to this type of

investigation. In three parts, this chapter will describe the crystal chemistry and attempts to study site-specific substitution in the $Bi_2M_4O_{9+\delta}$ structure. In Section 2.2, the substitution of diamagnetic gallium for magnetic iron will be described. A previously unreported spin rearrangement as a function of temperature in $Bi_2Fe_4O_9$ will be presented. Section 2.3 entails a similar study of the substitution of aluminum for iron. The differences in crystal chemistry between gallium and aluminum will be discussed. In the final section of this chapter, the successful site-specific substitution of manganese for iron is described.

Section 2.2: $Bi_2Fe_{4-x}Ga_xO_9$

A. Experimental

1. Preparation of single crystals

Well-formed single crystals of the solid solution $Bi_2Fe_{4-x}Ga_xO_9$ with integral values of x were grown from a 5 gram charge of Bi_2O_3 flux using a five-fold excess of Bi_2O_3 (ÆSAR, 99.9%) and stoichiometric ratios of Fe_2O_3 (Cerac 99.99%) and Ga_2O_3 (Cerac, 99.99%) in a platinum crucible. While the use of alumina crucibles often resulted in aluminum contamination of the crystals, no platinum contamination was detected. The flux was heated to 950°C, soaked for 12 hours, slow cooled to 700°C at a rate of 5° per hour and then rapidly cooled to room temperature. The flux was washed with dilute nitric acid and crystals smaller than 0.1 mm with an orthorhombic habit were mechanically separated from the flux matrix. The crystals grew as small brown prisms.

2. *Crystallographic studies*

Crystallographic data are summarized in Table 2.2.1. Single-crystal diffraction studies of the x = 2 member, $Bi_2Fe_2Ga_2O_9$, were performed on an Enraf-Nonius CAD-4 diffractometer with graphite monochromated Mo Kα radiation (λ = 0.71069 Å). Cell constants and an orientation matrix for data collection were obtained from a least-squares refinement using the setting angles of 25 carefully centered reflections in the range of $18.00 < 2\Theta < 24.00°$. Based on the systematic absences of 0kl : k≠2n and h0l : h≠2n, packing considerations, a statistical analysis of intensity distribution, and the successful solution and refinement of the structure, the space group was determined to be Pbam (#55), the previously reported space group of $Bi_2Fe_4O_9$ and $Bi_2Ga_4O_9$.[23,24] A total of 1046 reflections were collected. The intensities of three representative reflections, measured after every 60 minutes of X-ray exposure time, remained constant throughout data collection indicating crystal and electronic stability. Data were corrected for Lorentz, polarization, absorption[31] and secondary extinction. Data were further corrected for absorption by means of DIFABS.[32]

All calculations were performed on a MicroVAX 3500 with the use of TEXSAN crystallographic software.[33] The structure was solved by direct methods,[34] and refinement was performed using a full-matrix least-squares calculation. The final values of the discrepancy factors were R = 0.053 ($R = \Sigma \| |F_o| - |F_c| \| / \Sigma |F_o| = 0.053$) and $R_w = 0.063$ ($R_w = \{(\Sigma w (|F_o| - |F_c|)^2 / \Sigma w F_o^2)\}^{1/2} = 0.063$), $w = 4F_o^2/\sigma^2(F_o^2)$. The goodness of fit was 2.15 and the highest peak in the final difference map was 4.19 e/Å^3. The atomic scattering

TABLE 2.2.1

Summary of Crystallographic data for $Bi_2Fe_2Ga_2O_9$

Empirical Formula	$Bi_2Fe_2Ga_2O_9$
Formula weight	813.09
Crystal color, habit	amber, prismatic
Crystal dimensions (mm)	0.080 x 0.030 x 0.030
Crystal system	orthorhombic
Space group	Pbam (No. 55)
No. reflections used for unit cell Determination (2Θ range)	25 (18.0 - 24.0 °)
Omega scan peak width at half height	0.32
Lattice parameters (Å)	
a	7.946 (1)
b	8.335 (1)
c	5.929 (1)
Volume ($Å^3$)	392.7
Z	2
D_{calc} (g/cm^3)	6.876
F_{000}	704
μ(Mo Kα) (cm^{-1})	549.16
Diffractometer	Enraf-Nonius CAD-4
Radiation	Mo Kα (λ = 0.71069 Å)
Temperature (°C)	24
Scan type	ω
$2\Theta_{max}$	69.9°
No. of Reflections Measured	1046
No. Observations (I > 3.00 σ(I))	555
No. Variables	24
Corrections	Lorentz-polarization Absorption (trans. factors: 0.87 - 1.29) Secondary Extinction (coefficient: 0.74117E-06)
Residuals: R; R_W	0.053; 0.063
Goodness of fit Indicator	2.15
Max.peak in Final Difference Map	4.19 e^-/ $Å^3$

factors were those of Cromer and Waber and corrections for anomalous dispersion were from Cromer.[31,35]

Precession photos of the other solid solution members were obtained on an Enraf-Nonius Diffractis 581 X-ray generator equipped with a Charles Supper Co. precession camera using a precession angle of 10° and a film to crystal distance of 59 mm. Stoichiometry was verified using a JEOL 733 wavelength dispersive microprobe with EDS capabilities.

3. *Preparation of polycrystalline samples*

Polycrystalline samples of the solid solution $Bi_2Fe_{4-x}Ga_xO_9$ were prepared in increments of 0.1 for values of $x = 0$ to 1 and in increments of 0.25 for values of $x = 1$ to 4. Stoichiometric amounts of the oxides Bi_2O_3 (ÆSAR, 99.9%) Fe_2O_3 (Cerac 99.99%) and Ga_2O_3 (Cerac, 99.99%) were ground under acetone, pressed into pellets and heated at 850°C in air for two weeks with frequent grindings. The pellets were heated in Al_2O_3 crucibles on platinum foil to prevent aluminum contamination. Polycrystalline samples were structurally characterized by powder X-ray diffraction on a Rigaku RU300 at 10 kW with Cu Kα radiation (λ = 1.54184Å). NBS mica (SRM 675) was used as a standard for accurate peak positions. Lattice parameters were determined using least-squares.

4. *Magnetic measurements*

Magnetic data were collected on sintered pieces using a Quantum Design MPMS SQUID magnetometer at temperatures ranging from 5 to 400K and in applied fields ranging from 0.1 to 50kG. A scan length of 6 cm was used and 20 measurements were performed over the scan length. A total of 3 scans

were averaged for each data point. All data were corrected for the diamagnetic contribution of a Kel-F sample holder. Samples were zero-field cooled to 5K and measured by heating unless otherwise noted.

5. Mössbauer spectroscopy

Mössbauer spectra of various gallium doping levels for $1 \leq x \leq 3$ were obtained using a conventional constant acceleration spectrometer. Sample temperatures in the range $4.2 \leq T \leq 300K$ were achieved by the use of a Janis Supervaritemp dewar and a Lake Shore temperature controller. The source was $^{57}Co(Rh)$ maintained at room temperature. Isomer shifts are reported relative to metallic iron at room temperature.

B. Results

1. Structural

A small well-formed amber crystal of $Bi_2Fe_2Ga_2O_9$ with the approximate dimensions 0.080 x 0.030 x 0.030 mm was used for the structure determination. The final positional and thermal parameters are listed in Table 2.2.2. Selected interatomic bond distances are shown in Table 2.2.3.

A view parallel to the **ab**-plane of $Bi_2Fe_2Ga_2O_9$ is shown in Figure 2.2.1 (the bismuth-oxygen bonds have been omitted for clarity). The structure consists of columns of edge-sharing octahedra which are corner-shared with corner-sharing tetrahedra as shown in Figure 2.2.2. The octahedra are located in layers that are separated by doubly packed tetrahedral layers. These layers form slabs of alternating octahedral-tetrahedral-octahedral coordination. The slabs in turn are separated from each other by planes of bismuth and oxygen. The octahedra are connected across the tetrahedral and bismuth oxide layer

TABLE 2.2.2

Positional and Isotropic Equivalent Thermal Parameters for $Bi_2Fe_2Ga_2O_9$

Atom	x	y	z	B(eq)
Bi	0.1761(1)	0.1734(1)	0	0.41(3)
Ga	0.3515(4)	0.3364(4)	1/2	0.44(5)
Ga*	1/2	0	0.2578(6)	0.42(4)
Fe	1/2	0	0.2578(6)	0.4
Fe*	0.3515(4)	0.3364(4)	1/2	0.4
O(1)	1/2	1/2	1/2	1.9(6)
O(2)	0.365(2)	0.206(1)	0.240(3)	0.6(2)
O(3)	0.133(3)	0.405(2)	1/2	0.4(3)
O(4)	0.153(3)	0.429(2)	0	0.4(3)

TABLE 2.2.3

Intramolecular distances for $Bi_2Fe_2Ga_2O_9$

Atom	Atom	distance	Atom	Atom	distance
Bi	O(2)	2.084(14)	Ga*	Ga*	2.873(8)
Bi	O(4)	2.141(20)	Ga*	Fe*	3.364(2)
Bi	O(4)	2.445(20)	Fe	O(2)	2.025(13)
Ga	O(1)	1.803(3)	Fe	O(3)	1.951(14)
Ga	O(2)	1.892(15)	Fe	O(4)	2.041(14)
Ga	O(3)	1.828(21)	Fe	Fe	2.873(8)
Ga	Ga*	3.364(4)	Fe	Fe*	3.364(2)
Ga*	O(2)	2.025(13)	Fe*	O(1)	1.803(3)
Ga*	O(3)	1.951(14)	Fe*	O(2)	1.892(15)
Ga*	O(4)	2.041(14)	Fe*	O(3)	1.828(21)

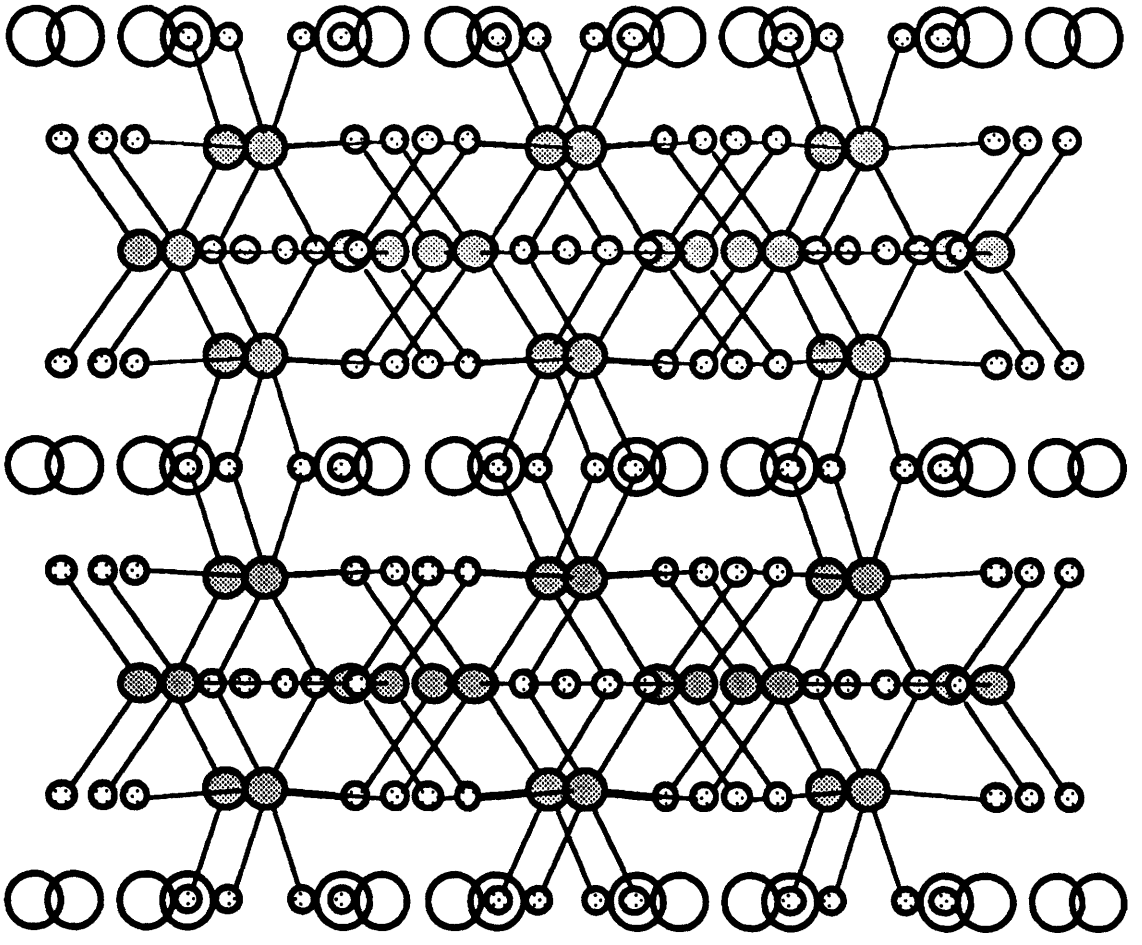

Figure 2.2.1: 2 x 2 x 2 unit cells of $Bi_2Fe_2Ga_2O_9$ viewed parallel to the **ab**-plane. Bismuth: ◯ ; Iron: ◍ ; Gallium: ◍ ; Oxygen: ◉ .

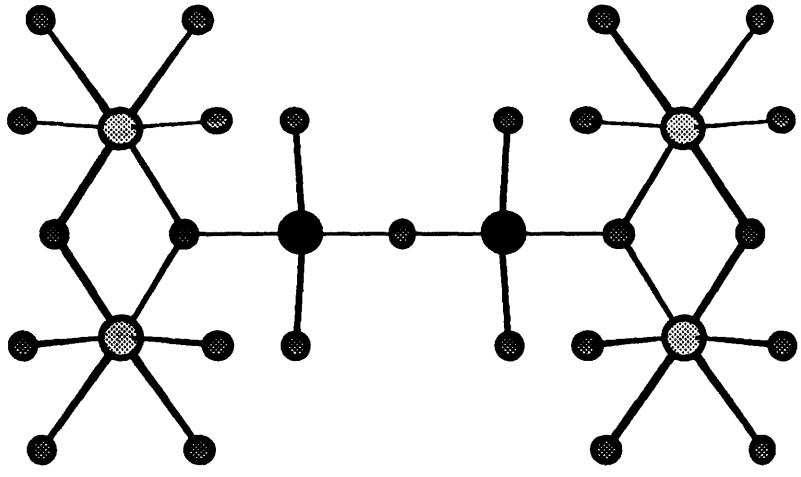

Figure 2.2.2: A view of edge-shared octahedral and corner-shared tetrahedral cation coordination sites. Octahedral site: ◎ ; tetrahedral site: ● ; oxygen: ●.

via edge-sharing oxygens located in the tetrahedral and bismuth oxide plane, respectively. The octahedra are tetragonally distorted; the longest and shortest metal oxygen distances are to the edge-shared oxygens in the bismuth oxide and the tetrahedral plane, respectively. The metal oxygen bond lengths in the slightly distorted tetrahedra vary from 1.80Å to 1.89Å, as shown in Table 2.2.2. The shortest metal oxygen bond of the tetrahedra, 1.80Å, is directed towards an oxygen which corner-shares two adjacent tetrahedra. In contrast, the bond to the oxygen which corner shares one octahedron and one tetrahedron is the longest metal oxygen bond, 1.89Å. The bismuth atoms are located at the apices of trigonal pyramids formed by mutually orthogonal, short (2.1 Å) Bi-O bonds. If the second- and third-nearest neighbors are included the bismuth ions are surrounded by eight oxygens. All oxygens in the structure are tetrahedrally coordinated.

A view perpendicular to the **ab**-plane, Figure 2.2.3, shows a complicated packing network of distorted 5-fold symmetry. The five-fold rings are made up of corner-shared polygons in repeating groups of corner shared tetrahedra, tetrahedra, octahedra, tetrahedra, octahedra. The order of planes going into the page is bismuth - octahedral sites - tetrahedral sites - octahedral sites - bismuth (the bismuth-oxygen bonds have been omitted for clarity).

The iron and gallium are nonstatistically distributed over the octahedral and tetrahedral sites. In comparison with the solid solution $Ga_{2-x}Fe_xO_3$, where the gallium sits exclusively on one tetrahedral site while the other somewhat distorted tetrahedron is randomly populated by both iron and gallium,[26,27] one might have expected either an ordered arrangement of gallium on the tetrahedral site or a statistical distribution of iron and gallium over the two

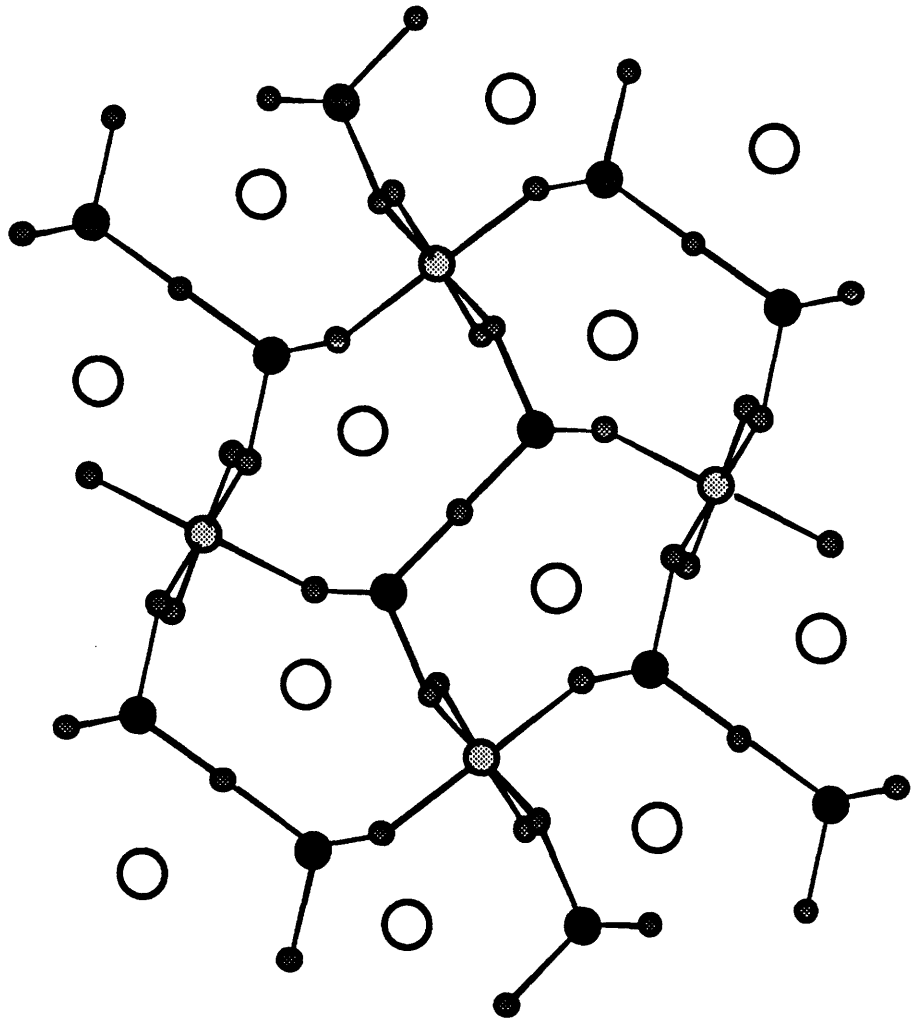

Figure 2.2.3 A view of distorted fivefold nets perpendicular to the **ab**-plane. The order of planes going into the page is bismuth-octahedral sites-tetrahedral sites-octahedral sites-bismuth (the bismuth-oxygen bonds have been omittedfor clarity). Bismuth: ○ ; Iron: ◎ ; Gallium: ● ; Oxygen: ●.

sites. Mössbauer spectroscopy was used to determine the distribution of iron on the octahedral and tetrahedral sites. The refined population ratio of iron to gallium on the octahedral sites is 60:40, as determined by Mössbauer spectroscopy *vide infra* and X-ray crystallography.

Lattice parameters for all members of the solid solution were determined from powder X-ray diffraction patterns. The powder pattern of $Bi_2Fe_4O_9$, peak positions listed in Table 2.2.4, is virtually identical to that of the isostructural $Bi_2Ga_4O_9$. The powder patterns of all members of the solid solution $Bi_2Fe_{4-x}Ga_xO_9$ could therefore be readily indexed and their lattice parameters determined. The lattice parameters follow Vegard's law[36] across the range of **x**, as shown in Figure 2.2.4. The compounds gradually changed color across the solid solution from $Bi_2Fe_4O_9$, red-brown, to $Bi_2Ga_4O_9$, yellow-white.

2. *Magnetism*

Magnetic measurements showed that the solid solution $Bi_2Fe_{4-x}Ga_xO_9$, for $0 \leq x \leq 2$ orders antiferromagnetically. This data is in agreement with the previously reported antiferromagnetic behavior of $Bi_2Fe_4O_9$.[24] The susceptibility plots display a very broad maximum, as shown for $Bi_2Fe_4O_9$ in Figure 2.2.5a which is often associated with either lower dimensional magnetic ordering[37] or a second order 3D magnetic phase transition.[38] The Néel temperature, T_N, was determined to be the temperature of the point of inflection below the maximum.[38] Using this method our T_N of 245K agrees with the data published by Tutov.[24]

TABLE 2.2.4

X-ray powder data[a] for $Bi_2Fe_4O_9$

d_{obs}(Å)	h	k	l	I/I_O
6.0479	0	0	1	25
4.2299	0	2	0	15
4.0044	2	0	0	10
3.7246	1	2	0	2
3.6143	2	1	0	2
3.1701	1	2	1	100
3.0920	2	1	1	85
2.8949	2	2	0	76
2.6652	1	3	0	48
2.5337	3	1	0	21
2.4390	0	2	2	12
2.3975	2	0	2	20
2.3073	2	1	2	21
2.0347	1	4	0	22
1.9317	3	3	0	50
1.8407	4	1	1	44

[a] lattice positions were corrected with NBS mica (SRM 675)

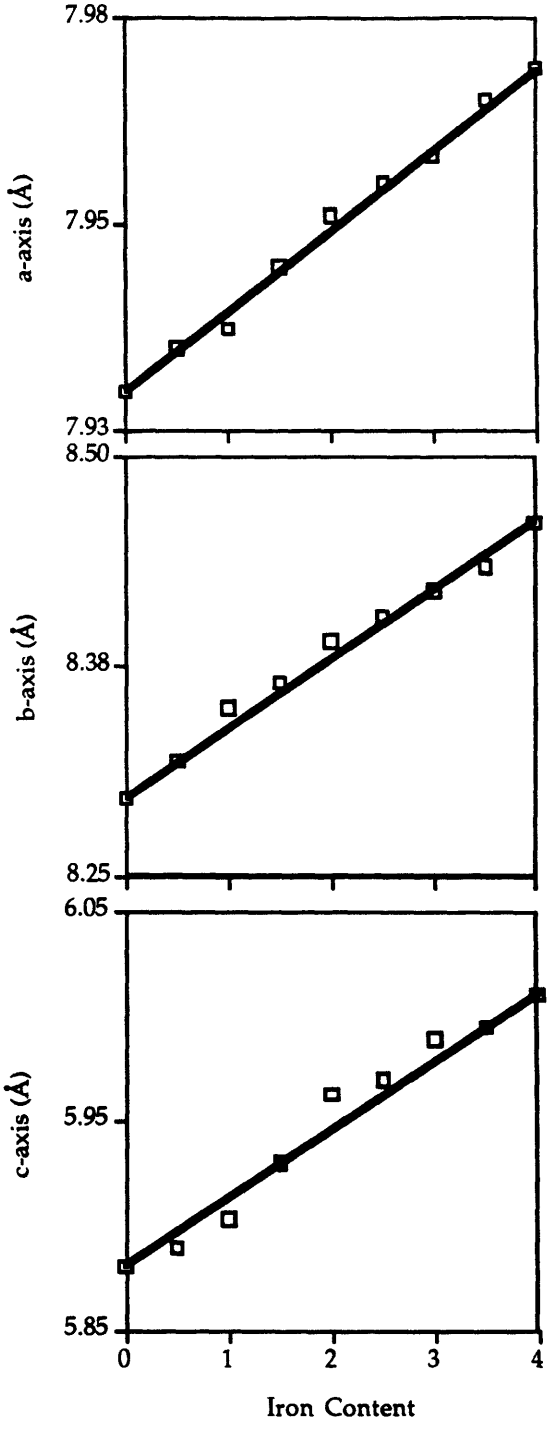

Figure 2.2.4 Lattice parameters for the solid solution $Bi_2Fe_{4-x}Ga_xO_9$. The solid line represents change expected according to Vegard's Law.

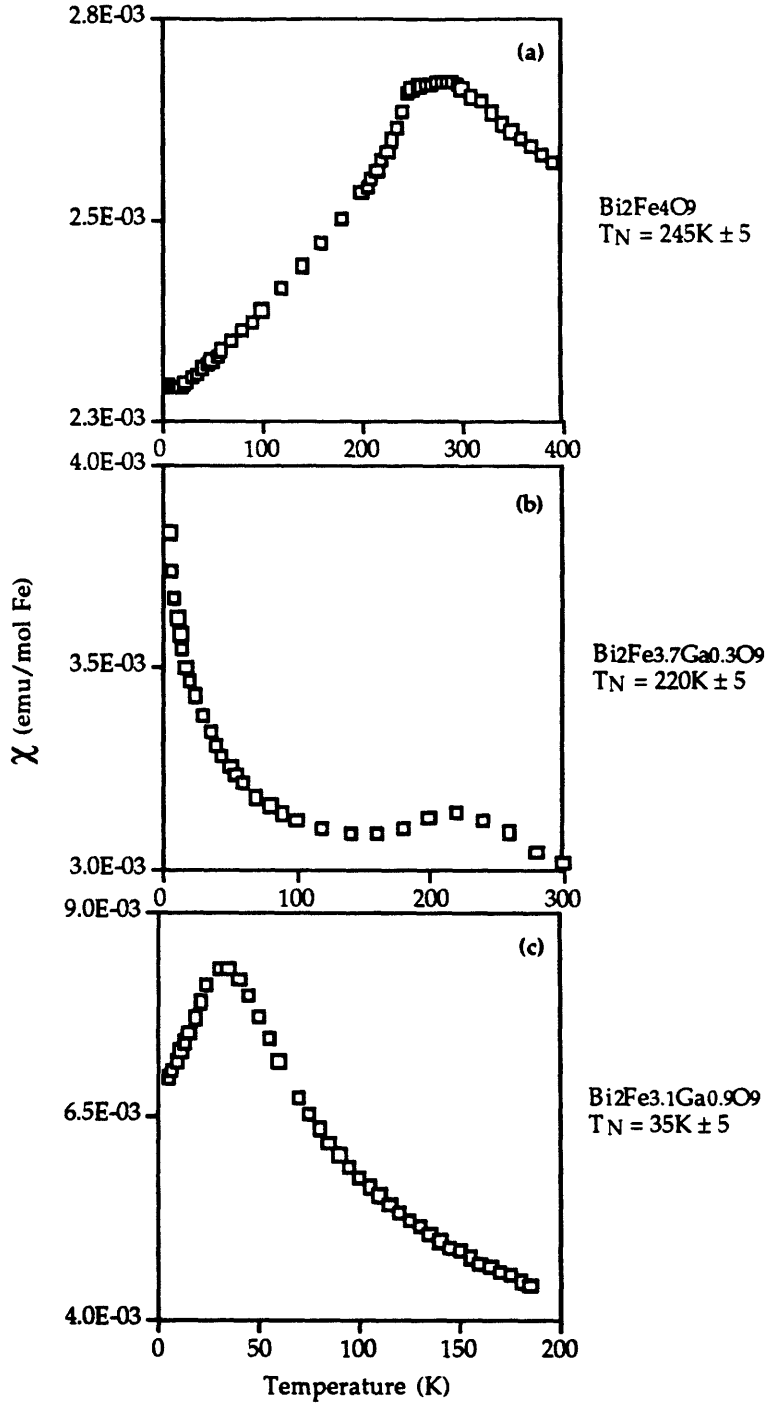

Figure 2.2.5 Magnetic susceptibility as a function of temperature of (a) $Bi_2Fe_4O_9$, T_N = 245 K ± 5; (b) $Bi_2Fe_{3.7}Ga_{0.3}O_9$, T_N = 220 K ± 5; (c) $Bi_2Fe_{3.1}Ga_{0.9}O_9$, T_N = 35 K± 5.

The change in T_N with gallium doping in $Bi_2Fe_{4-x}Ga_xO_9$ is shown in Figure 2.2.6. Small amounts of doping, up to x = 0.2, cause very little change in T_N. Additional gallium, x = 0.2 to 0.6, however, causes a precipitous drop in T_N from 230K to 60K. Further addition of gallium, x = 0.6 to 3, causes T_N to drop slowly but steadily towards zero. The susceptibility plots for this region of the solid solution, x = 0.6 to 3, where the transition temperatures are between 0 and 50K, show paramagnetic behavior up to a broad maximum and subsequent decrease, as expected for an antiferromagnet.(Figure 2.2.5c) In the region x = 0.2 to 0.6, (Figure 2.2.5b and 2.2.6) where T_N changes by about 170K, the susceptibility plots show characteristic second order antiferromagnetic behavior, with a broad maximum.[39] A Curie tail is also observed at low temperatures.

The susceptibility below the antiferromagnetic ordering temperature shows a field dependence and hysteresis, particularly in the region x = 0.6 to 3, as shown in Figure 2.2.7. The magnetic behavior observed when heating a sample from 5K to room temperature depends on whether or not the initial cooling of the sample was performed in the presence or absence of a magnetic field. Loading a sample into the magnetometer with the applied field already on results in magnetic behavior that is ferrimagnetic in appearance, while zero field produces behavior that is characteristic of an antiferromagnet. If a sample is cycled through zero-field and field cooling, an intermediate behavior is observed in the susceptibility plot.

3. *Mössbauer*

a) $Bi_2Fe_4O_9$

Mössbauer spectra were collected between room temperature and 4.2K.

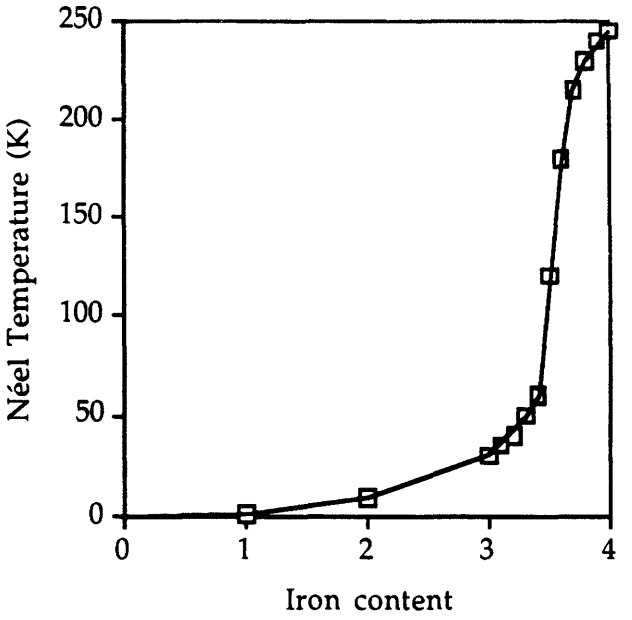

Figure 2.2.6 Transition temperature, T_N, of the solid solution $Bi_2Fe_{4-x}Ga_xO_9$ as a function of iron content. The solid line is added to guide the eye.

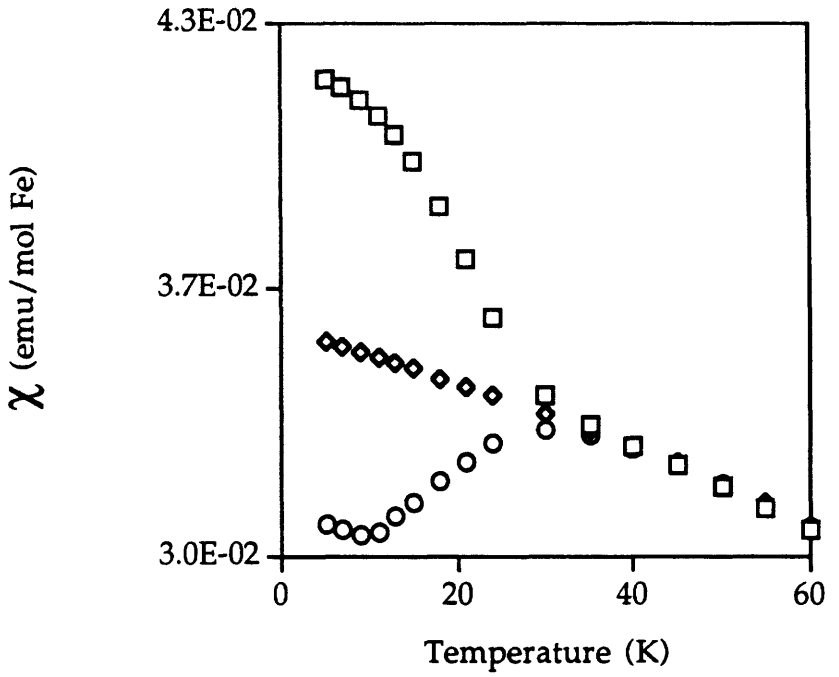

Figure 2.2.7 Hysteresis effect from spin-glass-like behavior of $Bi_2Fe_{3.1}Ga_{0.9}O_9$. Cooling in the presence of a 40kG field, , resulted in ferromagnetic-like behavior, while cooling in the absence of a field, o, resulted in antiferromagnetic behavior, T_N = 35K ± 5. Cooling in the absence of a field after previously cooling in a field, ◊, resulted in an intermediate behavior.

Representative spectra at selected temperatures are shown in Figure 2.2.8. Mössbauer parameters derived from least-square fits of the experimental data to theoretical models are tabulated in Table 2.2.5.

At high temperatures, $T \geq 250K$, the spectra are composed of the superposition of two well resolved quadrupole doublets with isomer shifts and quadrupole splittings $\delta_1 = 0.19$ mm/sec, $\Delta E_{Q1} = 0.78$ mm/sec, and $\delta_2 = 0.48$ mm/sec, $\Delta E_{Q2} = 0.54$ mm/sec, consistent with high spin Fe^{+3} ions at 250K in tetrahedral and octahedral environments, respectively. The intensity ratio of the two signals is 1:1 in agreement with the crystallographic structure of the compound which contains equal numbers of tetrahedral and octahedral sites. With decreasing temperature a complex magnetic behavior is observed within three distinct temperature regions, Figure 2.2.8.

The onset of magnetic hyperfine interactions occurs at $T_N = 245K \pm 5$ in agreement with the magnetic measurements. The functional dependence of the magnitude of the magnetic hyperfine field on the temperature is shown in Figure 2.2.9. At T = 220K a dramatic broadening of the Mössbauer spectra sets in. By T = 180K sharp 6-line magnetic spectra are recovered. With further decrease in temperature, as the magnetization of the compound approaches saturation, two magnetic subcomponents which are associated with the octahedral and tetrahedral iron sites, become discernible. There is a slight difference in the local saturation magnetic moments between the two subsites that is reflected in the magnitudes of their saturated magnetic hyperfine fields of $H_{sat}(oct) = 505$ kOe and $H_{sat}(tet) = 467$ kOe at T = 4.2K. (Figure 2.2.9 and Table 2.2.5)

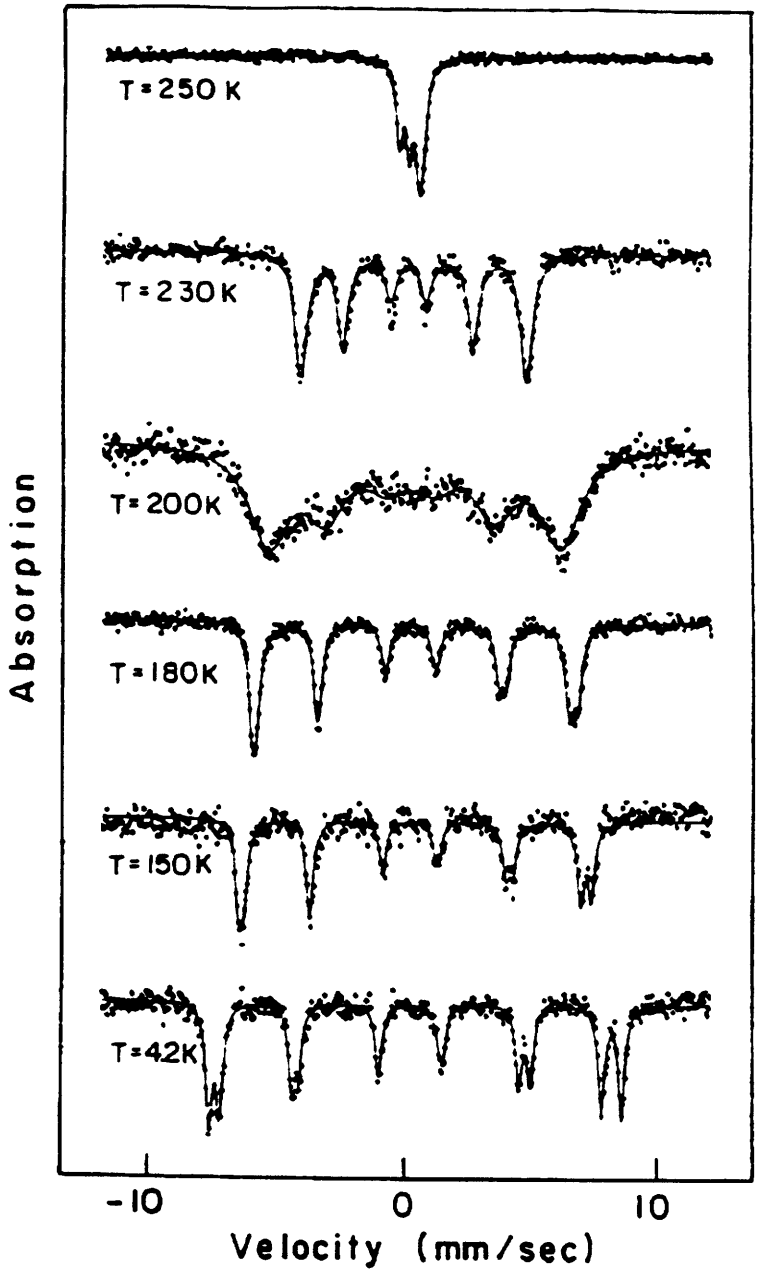

Figure 2.2.8 Mössbauer spectra of $Bi_2Fe_4O_9$ at several temperatures. The solid line is the least-squares fit of the data to theoretical models with the parameters given in Table 2.2.5.

TABLE 2.2.5

Mössbauer parameters for the solid solution $Bi_2Fe_{4-x}Ga_xO_9$

	T (K)	δ[a] (mm/sec)	ΔE_Q or ε (mm/sec)	H_{hf} (kOe)	$\Gamma/2$ (mm/sec)	%Area	T_N (K)
x=0	250	0.48[b]	0.54	--	0.15	48	245
		0.19[c]	0.78	--	0.15	52	
	230	0.34[d]	0.225	277	0.27	100	
	200	0.38[d]	0.18	358	0.95	100	
	150	0.45	0.15	432	0.14	42	
		0.34	0.16	412	0.18	58	
	4.2	0.48	0.15	505	0.16	50	
		0.34	0.16	467	0.17	50	
x=1	80	0.50	0.54	--	0.17	55	40
		0.26	0.79	--	0.16	45	
	4.2	0.48	-0.01	484	0.27	42	
		0.37	0.07	442	0.40	58	
x=2	80	0.53	-0.56	--	0.15	62	8
		0.24	0.80	--	0.14	38	
	4.2	0.49[d]	--	437	0.59	100	
x=3	80	0.50	0.57	--	0.16	69	< 4.2
		0.24	0.80	--	0.12	31	
	4.2	0.50	0.60	--	0.25	62	
		0.24	0.86	--	0.22	38	

[a] Isomer shifts are reported relative to metallic iron at room temperature.
[b] Octahedral sites
[c] Tetrahedral sites
[d] Single, averaged site fits due to unresolved octahedral and tetrahedral magnetic subsites.

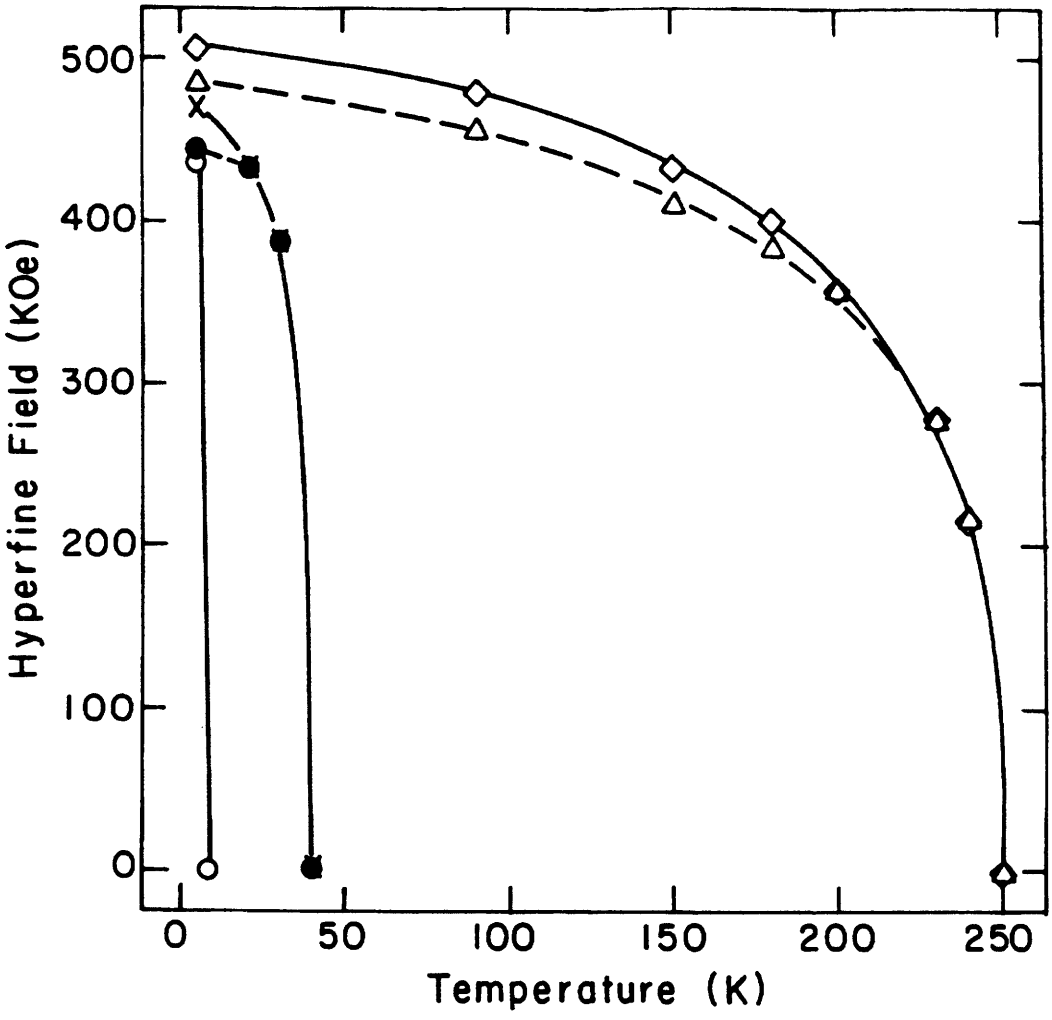

Figure 2.2.9 Magnetic hyperfine field measured by Mössbauer spectroscopy for the solid solution $Bi_2Fe_{4-x}Ga_xO_9$ as a function of temperature. ◊ : $Bi_2Fe_4O_9$ octahedral sites; Δ : $Bi_2Fe_4O_9$ tetrahedral sites; X: $Bi_2Fe_3GaO_9$ octahedral sites; • : $Bi_2Fe_3GaO_9$ tetrahedral sites. Coincident points are the result of averaged site fits due to poorly resolved subsites. o : $Bi_2Fe_2Ga_2O_9$ average sites.

With the exception of the anomalous spectral broadening at T ~ 220K the overall magnetic behavior is consistent with a 3D antiferromagnetic phase transition. The observed anomalous broadening can be a result of a spin reorientation[40-42] towards a close lying (in energy) different easy direction of magnetization. Another possibility is a structural phase transition, such as a second order displacive transition.

The theoretical analysis of the Mössbauer spectra reveals that the quadrupolar interaction, ε, a small perturbation to the dominant magnetic interaction below T_N, changes continuously from ε = 0.225 mm/sec for T ≥ 230K to ε = 0.155 mm/sec for T ≤ 150K (here an average between tetrahedral and octahedral sites is cited. See Table 2.2.4). For a magnetic phase transition, in the absence of a structural change

$$\varepsilon = \Delta E_Q/4\,(3\cos^2\theta - 1) \qquad (1)$$

where ΔE_Q is the quadrupole splitting above T_N and θ is the angle of the magnetic hyperfine field, H_{hf}, with respect to the principal component of the electric field gradient, V_{zz}, at a given crystallographic site. For ΔE_{Qave} = 0.66 mm/sec between the octahedral and tetrahedral sites at T = 250 K the change in ε observed would predict a spin reorientation of about 10° from $\theta°$ = 27° between H_{hf} and V_{zz} at T > 200K to $\theta°$ = 37° for T < 200K. Such a spin reorientation process is certainly plausible given the structural complexity of the compound. Magnetic structure determination by neutron diffraction measurements[22] at 80K has revealed a complex magnetic order with collinear antiferromagnetic pairs of moments defining three magnetic sublattices within the unit cell. However, if a structural phase transition has also taken place equation (1) would not be applicable and no prediction on $\theta°$ can be

made. Nevertheless, the broadening of the Mössbauer spectra is consistent with spin fluctuations between easy directions of magnetization with a relaxation frequency close to the Lamor precession frequency, $\nu_L = (g_n\mu_n/\hbar)H_{hf} = 2.8 \times 10^7\ sec^{-1}$, of the ^{57}Fe nuclear spin in the effective magnetic field of 358 kOe observed at T = 200K.

b) $Bi_2Fe_{4-x}Ga_xO_9$ solid solution

For low gallium doping the relative intensity of octahedral to tetrahedral quadrupole doublets observed above T_N indicate that there is no preferential ordering between the iron and the gallium. For higher gallium doping, however, the iron preferentially occupies the octahedral sites, with the octahedral to tetrahedral ratio of iron occupation being 2.225 at x = 3 and approaching 1 as x goes to zero, see Figure 2.2.10.

The Mössbauer spectra for all values of x showed temperature behavior consistent with 3D magnetic ordering; T_N decreases with increasing x, as shown in Figure 2.2.6. No anomalous spectral broadening was observed for these samples at any temperature. The temperature dependence of the normalized hyperfine fields $H_{hf}(T)/H_{hf}(sat)$ are plotted *vs.* reduced temperature T/T_N in Figure 2.2.11. Here it is assumed that saturation magnetic fields, similar to those of $Bi_2Fe_4O_9$, would have been obtained for all values of x if low enough values of T could be achieved experimentally. We observe that for all values of x the experimental data follow an S = 5/2 Brillouin function as expected for a 3D magnetic phase transition which can be described by molecular field theory.[38,39]

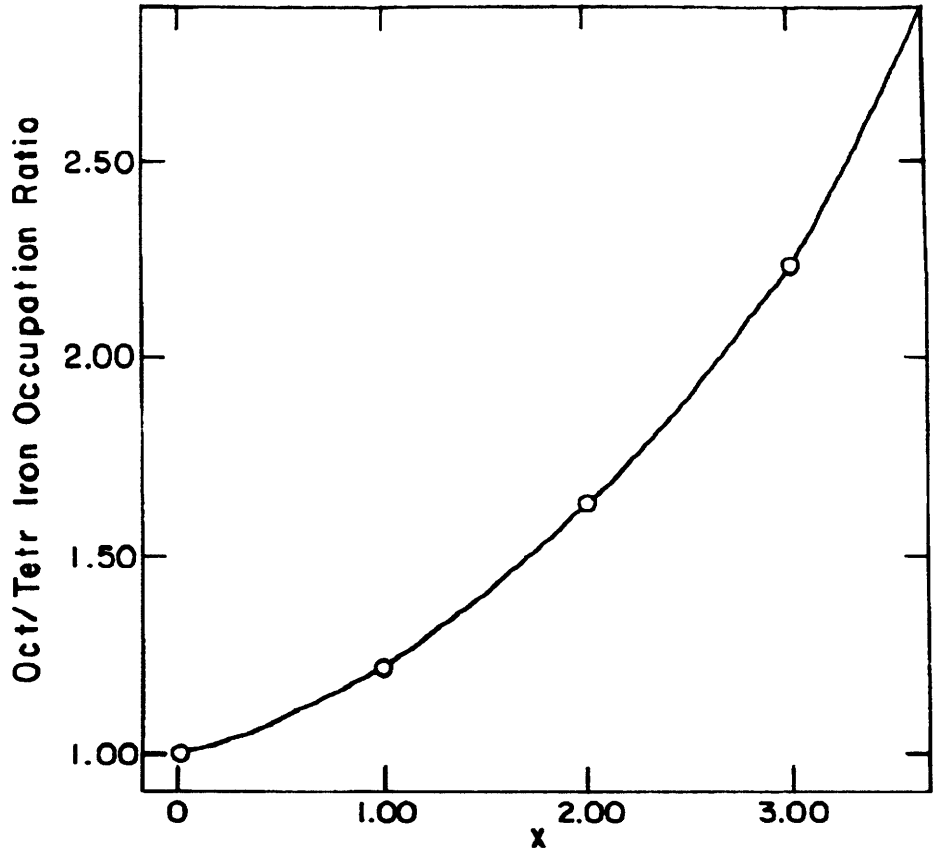

Figure 2.2.10 Octahedral/tetrahedral occupation ratio for iron in $Bi_2Fe_{4-x}Ga_xO_9$ as a function of x.

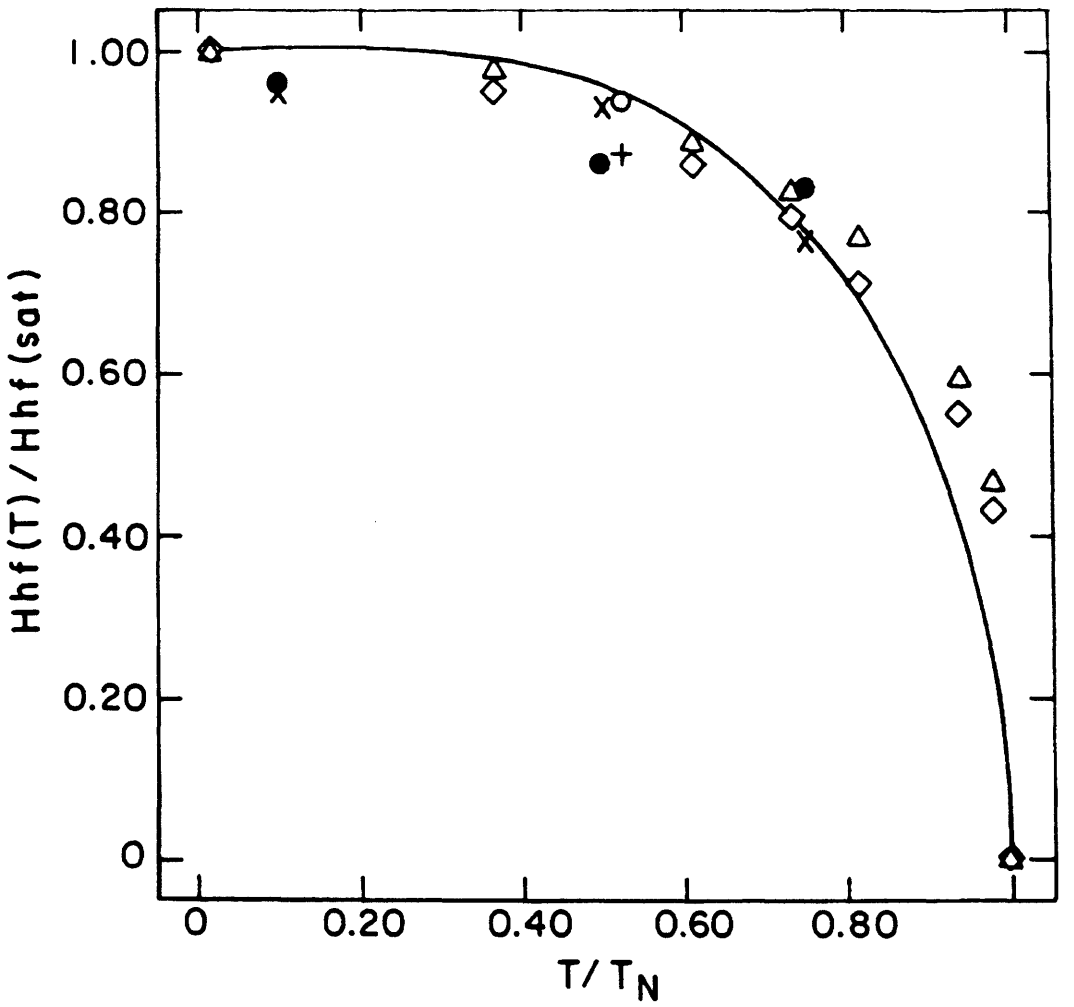

Figure 2.2.11 Normalized magnetic hyperfine field *vs.* reduced temperature for $Bi_2Fe_{4-x}Ga_xO_9$. ◊ : $Bi_2Fe_4O_9$ octahedral sites; Δ : $Bi_2Fe_4O_9$ tetrahedral sites; X: $Bi_2Fe_3GaO_9$ octahedral sites; • : $Bi_2Fe_3GaO_9$ tetrahedral sites; o : $Bi_2Fe_2Ga_2O_9$ average sites. The solid line is the theoretical fit for the Brillouin function with S = 5/2.

C. *Discussion*

The values of T_N obtained from the Mössbauer study agree with those of the magnetic measurements. The broadness of the transition in the susceptibility plots might be interpreted as low dimensional magnetic ordering, however, its shape is more akin to those due to 3-dimensional, 2nd order transitions, which result in no discontinuity in the χ *vs.* T plots at T_N.[38,39] This interpretation is supported by the Mössbauer data, described above, which is also consistent with a 3D magnetic phase transition.

The effect of gallium doping on the transition temperature, T_N, in $Bi_2Fe_{4-x}Ga_xO_9$ shows a strong concentration dependence for x between 0.2 and 0.6, see Figure 2.2.6, where T_N drops from 230 to 60K. Rapid drops in the antiferromagnetic transition temperature for doping levels exceeding some small threshold value have been observed in other iron containing oxides[41] and are characteristic of systems having competing magnetic interactions.[43]

In systems with non-competing magnetic interactions the magnetic ordering temperature is gradually reduced with increasing dilution until, at the percolation limit, there is no longer any infinite cluster of atoms connected by magnetic interactions, and consequently long range magnetic order ceases. In systems having competing magnetic interactions, on the other hand, the magnetic order of the pure system breaks down more quickly with dilution and spin glass phenomena can occur.

The breakdown in the magnetic order in $Bi_2Fe_{4-x}Ga_xO_9$ is not a simple percolation effect, as indicated by the rapid drop in T_N with gallium doping, but more likely a spin frustration phenomenon, such as a spin glass-like

behavior, due to competing next nearest neighbor exchange interactions. These interactions have the effect of destabilizing the magnetic long range order produced by the nearest neighbor exchange interactions. The effects of spin frustration are observed below the transition temperature in the magnetic susceptibility data, see Figure 2.2.7, in the form of field and magnetic history dependent behavior, due to uncompensated spins created by the dilution of magnetic iron with non-magnetic gallium.(Figure 2.2.5b)

These changes in the magnetic order are also noticeable in the Mössbauer data, where a change in the spin direction is observed as a function of gallium doping. Theoretical fits of the sample with composition $Bi_2Fe_3GaO_9$ result in a value of the quadrupolar perturbation ε close to zero, indicating that $\theta° \sim 54°$. This is quite different from the spin direction $\theta° \sim 37°$ in the all iron composition, $Bi_2Fe_4O_9$. The magnetic structure in terms of the direction of the magnetization relative to the crystalline axes, therefore, depends on, and changes with, the degree of gallium doping. A new local magnetic order is established as an increasing number of nonmagnetic Ga^{+3} ions replace the magnetic Fe^{+3} ions in the crystal lattice, perhaps precipitating the sharp decline in T_N for $0.2 \leq x \leq 0.6$. This doping region may represent the regime in which the new local order is being established. For smaller doping levels, $0 \leq x \leq 0.2$, the system retains its long range magnetic order, with only a small decrease in the strength of the exchange interaction energy due to the introduction of nonmagnetic Ga^{+3} ions. For doping levels exceeding $x = 0.6$, only short range magnetic interactions remain with a concomitant change in the Néel temperature that subsequently decreases to zero at the percolation limit as most of the Fe^{+3} has been replaced by Ga^{+3}. This loss of long range magnetic order in favor of only short range order would result in a spin-glass

type of magnetic structure which is consistent with the observation of increasingly broader magnetic Mössbauer spectral widths of $\Gamma/2$ = 0.16, 0.34 and 0.59 for x = 0, 1, and 2, respectively.(Table 2.2.5)

The spin reorientation in $Bi_2Fe_4O_9$ can be explained without invoking a structural change. In centrosymmetric structures it is possible to lose the inversion symmetry during a magnetic transition, such as antiferromagnetic ordering. In such cases the appearance of ferroelectricity and piezoelectricity is expected. In fact, according to Goshen[44] magnetic symmetry changes brought on by antiferromagnetic ordering can induce ferroelectric transitions. This behavior has been predicted to occur in the isostructural $Bi_2Mn_4O_{10}$, and, if similar behavior were to occur in $Bi_2Fe_4O_9$, the observed broadening of the Mössbauer spectrum would not be unexpected.

It has been suggested based on neutron data on $Bi_2Fe_4O_9$ that at 4.2K all the spins are aligned anti-parallel within the plane of the transition metal slabs.[22] The spin rearrangement that we have observed, therefore, indicates that above 220K the spins are oriented in a different fashion. From the data collected, however, it is not possible to determine exactly what the spin orientation is above 220K. Neutron diffraction measurements would be necessary in order to ascertain the nature of this spin rearrangement, which could be due to a structural or magnetic transition in the material.

D. Conclusions

The complete solid solution $Bi_2Fe_{4-x}Ga_xO_9$ has been synthesized and investigated structurally and magnetically. The crystal structure of the x = 2 member, $Bi_2Fe_2Ga_2O_9$, was solved and determined to be isostructural with the end members, $Bi_2Fe_4O_9$ and $Bi_2Ga_4O_9$. Polycrystalline samples were seen

to follow Vegard's law. The doping of nonmagnetic Ga^{3+} for magnetic Fe^{3+} caused a precipitous drop in the antiferromagnetic transition temperature, T_N, and spin glass-like behavior was observed by Mössbauer spectroscopy. A change in the spin direction and consequently the magnetic structure was also observed by Mössbauer spectroscopy as a result of gallium doping. A previously unreported spin rearrangement was discovered for the x = 0 sample.

Section 2.3: $Bi_2Fe_{4-x}Al_xO_9$

A. Experimental

1. Sample preparation

Polycrystalline samples of the solid solution $Bi_2Fe_{4-x}Al_xO_9$ were prepared in increments of 0.25 for values of x = 0 to 1 and in integral increments for values of x = 1 to 4. Stoichiometric amounts of the oxides Bi_2O_3 (Cerac, 99.9%), Fe_2O_3 (Cerac, 99.99%) and Al_2O_3 (ÆSAR, 99.99%) were ground under acetone, pressed into pellets and heated at 850°C in air for two weeks with frequent grindings. The pellets were heated in Al_2O_3 crucibles on platinum foil to prevent aluminum contamination.

2. Structural characterization

Polycrystalline samples were structurally characterized by powder X-ray diffraction on a Rigaku RU300 at 10 kW with Cu K_α radiation (λ = 1.54184Å). NBS mica (SRM 675) was used as a standard for accurate peak positions. A polycrystalline sample of $Bi_2Fe_2Al_2O_9$ was used for the structure determination. An X-ray powder diffraction step scan was collected from 5° - 120° 2Θ, using a step size of 0.02° 2Θ and a time of 5 sec/step. A Rietveld

refinement of the powder X-ray diffraction data was performed using the refinement package GSAS.[45] The single crystal structure of $Bi_2Fe_2Ga_2O_9$[30] was used as the starting model.

3. Magnetic measurements

Magnetic data were collected on sintered pieces using a Quantum Design MPMS SQUID magnetometer at temperatures ranging from 5 to 400K and in applied fields ranging from 5 to 40kG. A scan length of 6 cm was used and 20 measurements were performed over the scan length. A total of 3 scans were averaged for each data point. All data were corrected for the diamagnetic contribution of the Kel-F sample holder. Samples were zero-field cooled unless otherwise noted.

4. Mössbauer spectroscopy

Mössbauer spectra of various aluminum doping levels between $0 \leq x \leq 2$ were obtained using a conventional constant acceleration spectrometer. Sample temperatures in the range $100K \leq T \leq 300K$ were achieved by the use of a Janis Supervaritemp dewar and a Lake Shore temperature controller. The source was $^{57}Fe(Rh)$ maintained at room temperature. Isomer shifts are reported relative to metallic iron at room temperature.

B. Results

1. Structural

Structure refinement parameters are shown in Table 2.3.1. The final positional and thermal parameters are listed in Table 2.3.2 and selected interatomic bond distances are shown in Table 2.3.3 The structure of $Bi_2Fe_2Al_2O_9$ is shown in Figure 2.3.1.

TABLE 2.3.1

Crystal Structure Determination Parameters for $Bi_2Fe_2Al_2O_9$

Empirical Formula			$Bi_2Fe_2Al_2O_9$		
Formula weight			727.61		
Crystal system			orthorhombic		
Space group			Pbam (No. 55)		
Lattice parameters (Å)					
a			7.8611 (3)		
b			8.2753 (3)		
c			5.8535 (3)		
Volume ($Å^3$)			380.80		
Z			2		
Diffractometer			Rigaku RU300		
Radiation			Cu Kα (λ = 1.54 Å)		
Temperature (° C)			24		
2Θ range			$10 \leq 2\Theta \leq 100$		
Number of Observations			4250		
Refinement			Rietveld; program: GSAS[a]		
Peak shape function			pseudo-Voigt[b]		
Peak shape coefficients					
GU	1.675E+3	GV	-5.292E+2	GW	1.106E+2
LX	3.669E+0	LY	3.951E+1	stec	2.633E+0
ptec	-1.094E-1				
Background			10 coeff. cosine Fourier series		
Residuals: wRp; Rp			0.0944; 0.0671		

[a] GSAS: General Structure Analysis System, LANSCE, Los Alamos National Laboratory.

[b] J. Appl. Cryst. **15**, 615-620, 1982.

TABLE 2.3.2

Atomic coordinates for $Bi_2Fe_2Al_2O_9$

Atom	x	y	z	U_{iso}
Bi	0.1736(1)	0.1713(1)	0	0.015
Al(1)	1/2	0	0.2594(8)	0.019
Al(2)	0.3550(6)	0.3414(6)	1/2	0.007
Fe(1)	0.3550(6)	0.3414(6)	1/2	0.019
Fe(2)	1/2	0	0.2594(8)	0.007
O(1)	0	0	1/2	0.012
O(2)	0.3699(9)	0.215(1)	0.238(1)	0.005
O(3)	0.134(2)	0.408(2)	1/2	0.004
O(4)	0.148(2)	0.435(2)	0	0.016

TABLE 2.3.3

Selected bond lengths(Å) and angles(°) for $Bi_2Fe_2Al_2O_9$

Bi - O(2)	2.110(7) x 2	O(2) - Bi - O(2)	82.7(4)
Bi - O(2)	2.921(7) x 2	O(2) - Bi - O(4)	84.2(4) x 2
Bi - O(4)	2.187(14)	O(2) - Bi - O(4)	73.3(3) x 2
Bi - O(4)	2.410(13)	O(4) - Bi - O(4)	149.7(2)
Bi - oct.	3.301(2) x 4	O(2) - oct. - O(2)	173.1(5)
Bi - oct.	3.401(2) x 2	O(2) - oct. - O(3)	96.7(4)
oct. - O(2)	2.054(8) x 2	O(2) - oct. - O(3)	88.4(4)
oct. - O(3)	1.917(9) x 2	O(2) - oct. - O(4)	84.2(4)
oct. - O(4)	1.988(9) x 2	O(2) - oct. - O(4)	90.5(5)
oct. - oct.	3.036(9) x 2	O(3) - oct. - O(3)	85.4(7)
oct. - oct.	2.817(9) x 2	O(3) - oct. - O(4)	97.6(4)
tet. - O(1)	1.738(5)	O(3) - oct. - O(4)	172.3(5)
tet. - O(2)	1.861(8) x 2	O(4) - oct. - O(4)	80.4(7)
tet. - O(3)	1.823(12)	O(1) - tet. - O(2)	112.5(3)
		O(1) - tet. - O(3)	113.5(5)
		O(2) - tet. - O(2)	110.9(6)
		O(2) - tet. - O(3)	103.3(4)

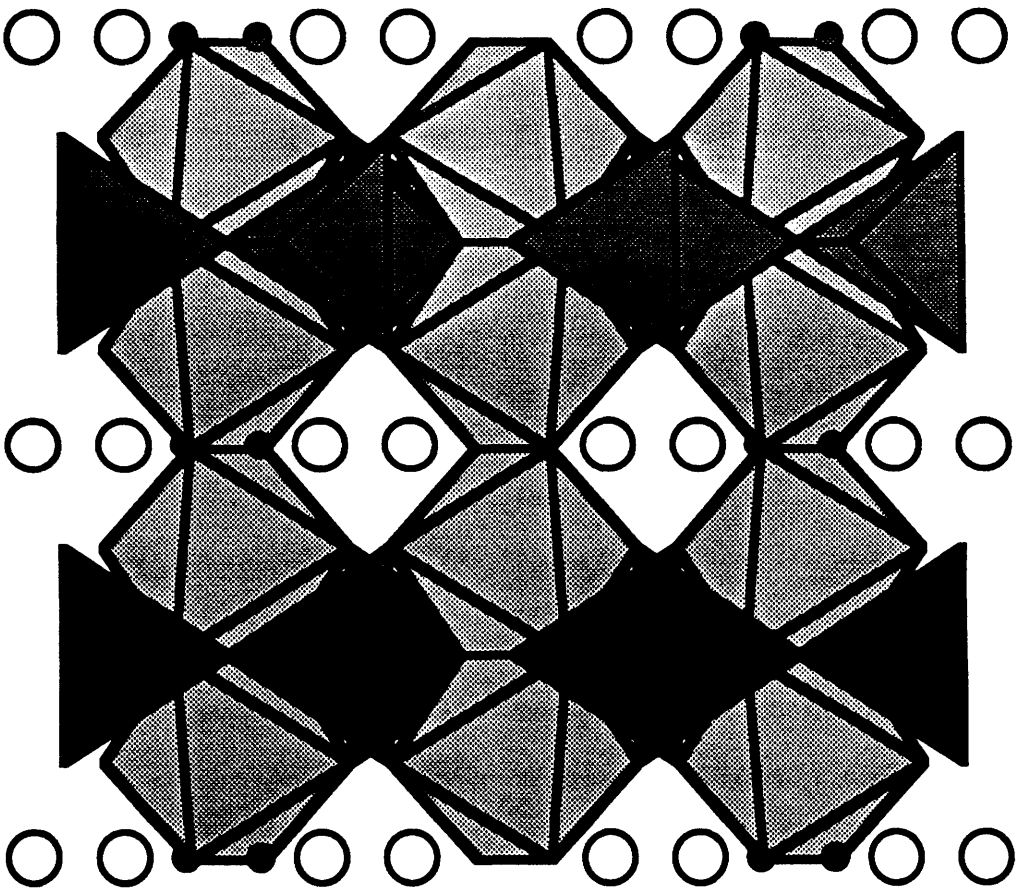

Figure 2.3.1 Polyhedral representation of the octahedral and tetrahedral cation coordination geometries of $Bi_2Fe_2Al_2O_9$. The view is identical to that shown in Figure 2.2.1. Oxygen atoms are located at the apices of each polyhedron.

The structure of $Bi_2Fe_2Al_2O_9$ consists of columns of edge-sharing octahedra which are corner-shared with corner-sharing tetrahedra as shown in Figure 2.3.2. The octahedra are located in layers perpendicular to the **c**-axis that are separated by doubly packed tetrahedral layers. These layers form slabs of alternating octahedral-tetrahedral-octahedral coordination. The slabs in turn are separated from each other by planes of bismuth and oxygen. The octahedra are connected across the tetrahedral and bismuth oxide layer *via* edge-sharing oxygens located in the tetrahedral and bismuth oxide plane, respectively. The corner-shared tetrahedra are coupled perpendicular to the octahedral chains, linking chains to each other. A view down the length of the octahedral chains is shown in Figure 2.3.3.

The octahedral metal-oxygen bonds vary from 1.92Å to 2.05 Å, with the shortest octahedral metal-oxygen distance, 1.92 Å, edge-sharing within the octahedral chains. The metal-oxygen bond lengths in the slightly distorted tetrahedra vary from 1.74Å to 1.86Å, as shown in Table 2.3.2. The shortest metal-oxygen bond length in the tetrahedra, 1.74Å, corner-shares two adjacent tetrahedra. All oxygens in the structure are tetrahedrally coordinated.

The iron and aluminum atoms are statistically distributed over the octahedral and tetrahedral sites, in contrast with the solid solution $Bi_2Fe_{4-x}Ga_xO_9$, where the gallium sits preferentially on the tetrahedral sites in a ratio of 3:2. The powder pattern of $Bi_2Fe_2Al_2O_9$ is shown in Figure 2.3.4 and hkl values are listed in Table 2.3.4. Lattice parameters for all members of the solid solution were also determined from powder X-ray diffraction patterns. The lattice parameters were found to follow Vegard's law[36] across

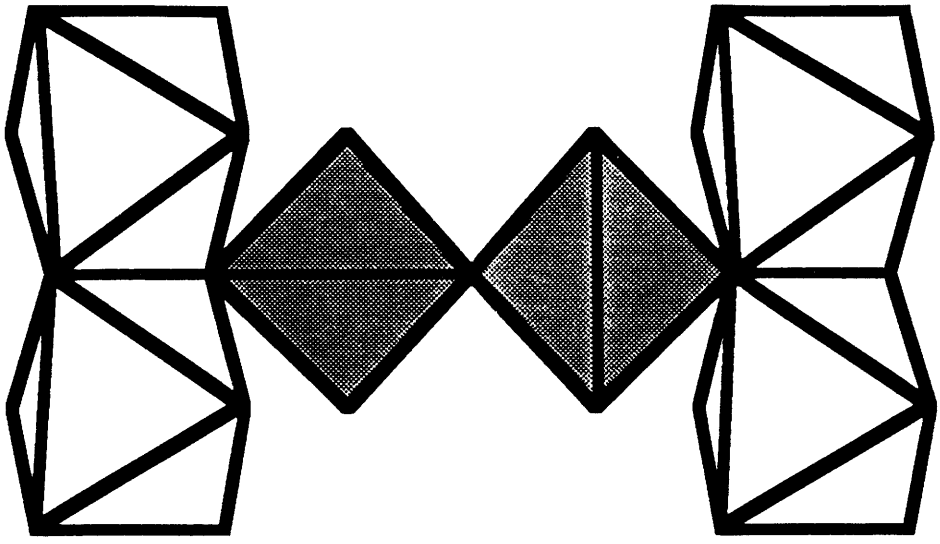

Figure 2.3.2a Polyhedral representation of the local symmetry surrounding the tetrahedral and the octahedral cation coordination geometries.

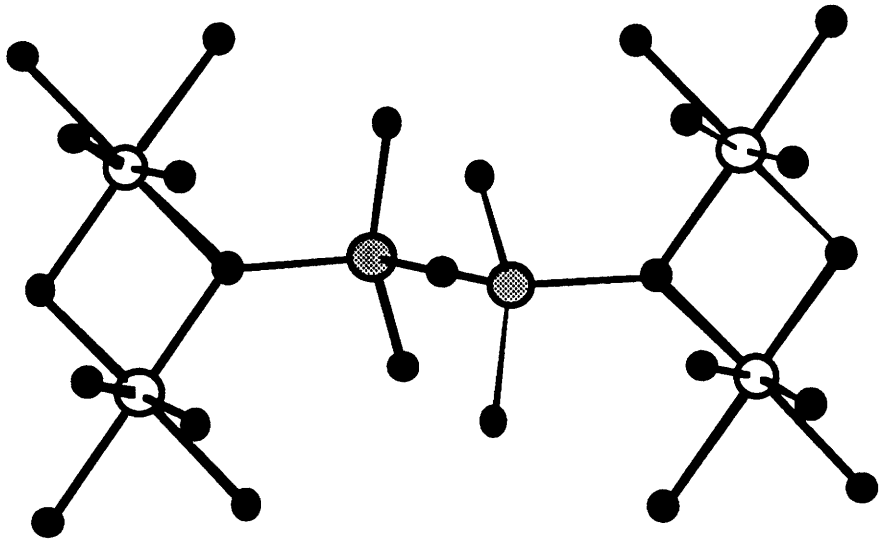

Figure 2.3.2b Atomic view of the local symmetry seen in Figure 2.3.2a. Octahedral atoms: ○; Tetrahedral atoms: ◎; Oxygen: ●.

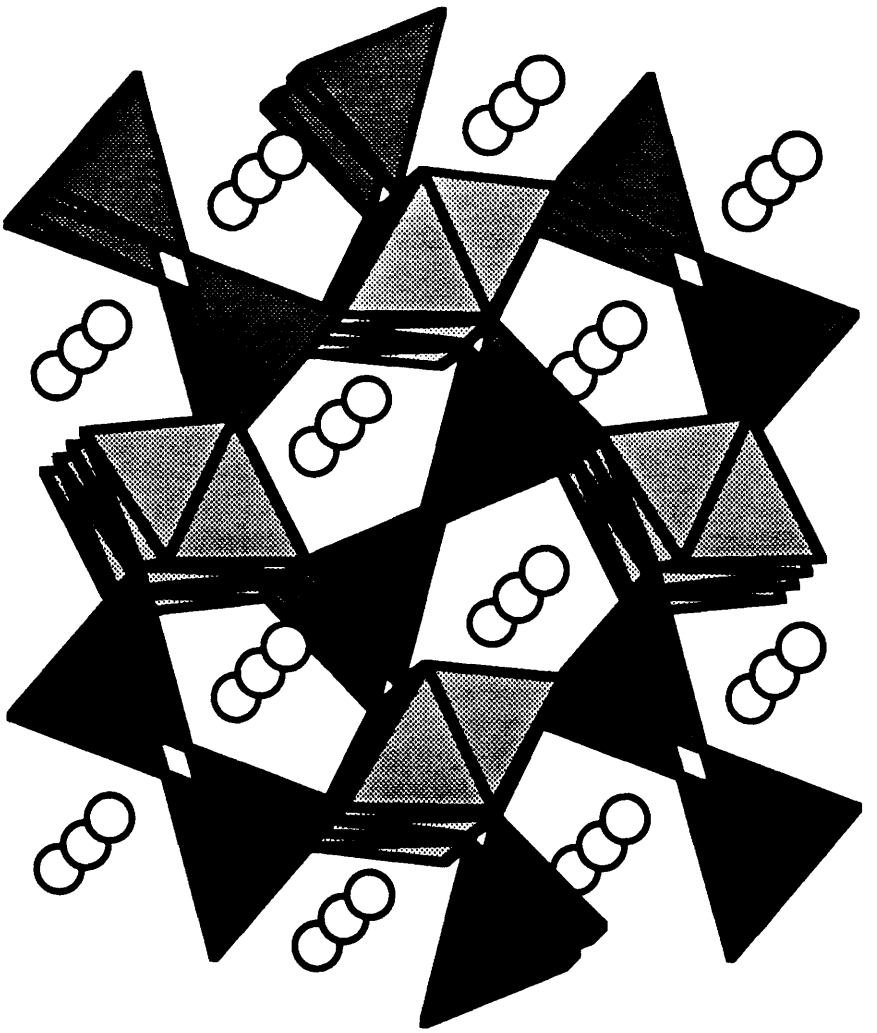

Figure 2.3.3 Polyhedral representation of $Bi_2Fe_2Al_2O_9$ viewed perpendicular to the **ab**-plane.

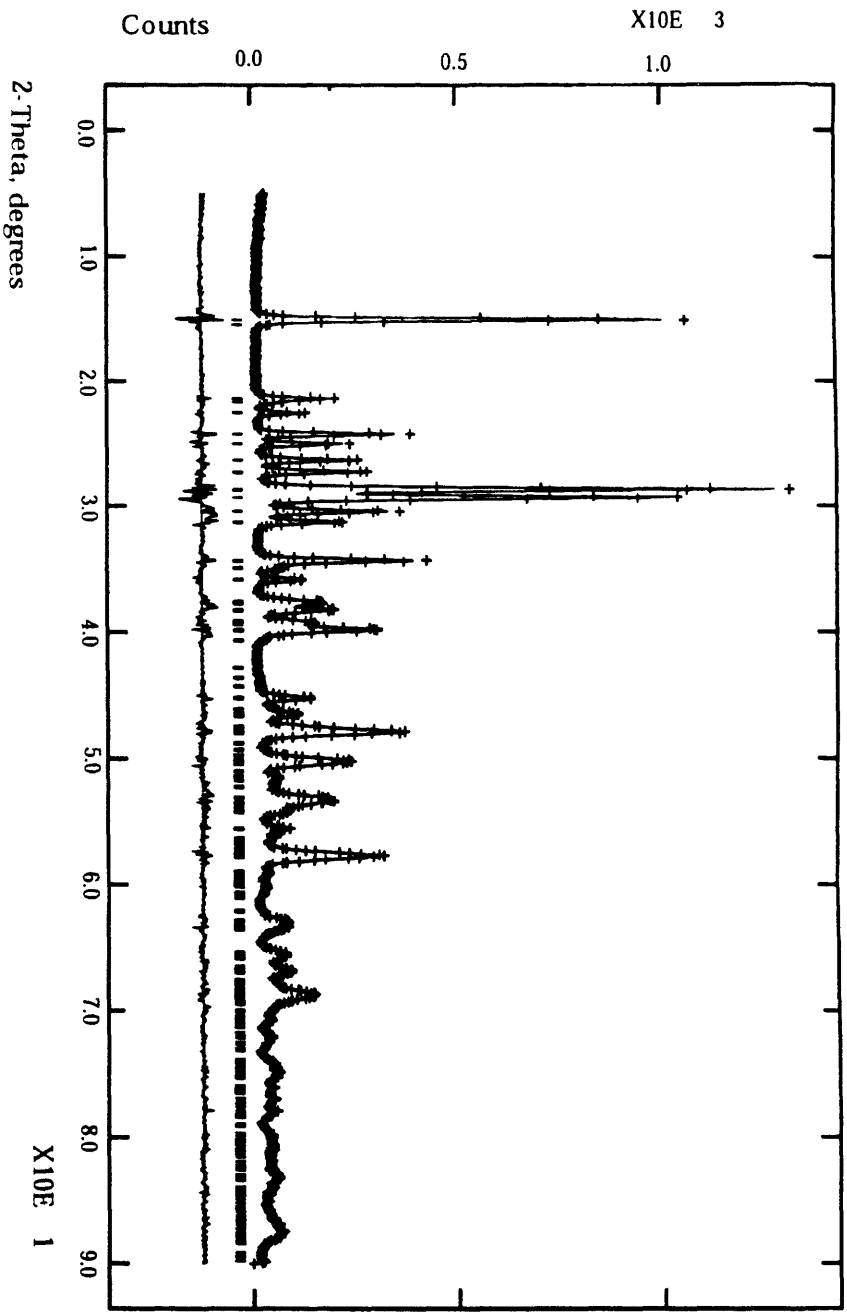

Figure 2.3.4 The observed, calculated and difference profiles of the powder X-ray diffraction Rietveld refinement of $Bi_2Fe_2Al_2O_9$. Peak positions are listed in Table 2.3.4.

TABLE 2.3.4

X-ray powder data for $Bi_2Fe_2Al_2O_9$ from Figure 2.3.4*

d_{calc} (Å)	h	k	l	I_{calc}	I_{obs}
5.853	0	0	1	79	82
4.138	0	2	0	13	15
4.083	1	1	1	3	5
3.931	2	0	0	10	11
3.661	1	2	0	26	29
3.550	2	1	0	17	17
3.379	0	2	1	19	19
3.263	2	0	1	25	22
3.104	1	2	1	100	100
3.036	2	1	1	85	82
2.9267	0	0	2	28	26
2.8497	2	2	0	16	17
2.6035	1	1	2	33	32
2.5622	2	2	1	3	3
2.4981	3	1	0	11	9
2.3894	2	2	9	13	10
2.3475	2	0	2	17	15
2.2976	3	1	1	7	10
2.2583	2	1	2	27	24
2.0007	1	4	0	11	10
1.9450	1	3	2	4	6
1.9121	4	1	0	7	7
1.8932	1	4	1	21	25
1.8176	4	1	1	16	15
1.7249	1	2	3	12	9
1.7100	2	1	3	12	11
1.6517	1	4	2	7	4
1.6008	4	1	2	10	14
1.5935	3	3	2	24	22
1.4761	2	5	1	5	5
1.4634	0	0	4	5	5
1.4255	5	2	1	4	4
1.3993	3	5	0	2	4
1.3657	4	1	3	4	6
1.3589	1	2	4	2	3
1.1151	1	2	5	2	3

*Calculated peaks which were unobserved in the powder pattern are not included

the range of x. The compounds gradually changed color across the solid solution from $Bi_2Fe_4O_9$, orange-brown, to $Bi_2Al_4O_9$, pale yellow.

2. Magnetic

Magnetic measurements showed that the solid solution $Bi_2Fe_{4-x}Al_xO_9$, for $3 \leq x \leq 4$ orders antiferromagnetically. This is in agreement with the previously reported antiferromagnetic behavior of $Bi_2Fe_4O_9$,[23] and our solid solution $Bi_2Fe_{4-x}Ga_xO_9$.[30] The susceptibility plots display broad maxima, as shown in Figure 2.3.5, but not as broad as those seen in either the undoped $Bi_2Fe_4O_9$ system or the solid solution $Bi_2Fe_{4-x}Ga_xO_9$.[30] Broadness of susceptibility maxima is often associated with either lower dimensional magnetic ordering[37] or a second-order 3D magnetic phase transition.[38] The presence of uncompensated spins is seen as a rise in magnetic susceptibility at low temperatures in the susceptibility *vs.* temperature plot of the $x = 0.25$ compound.

The change in T_N with aluminum doping in $Bi_2Fe_{4-x}Al_xO_9$ is shown in Figure 2.3.6. The Néel temperature, T_N, was determined as the temperature of the point of inflection below the maximum.[38] The observed behavior is similar to that which we have reported on $Bi_2Fe_{4-x}Ga_xO_9$.[30] Small amounts of Al doping, up to $x = 0.25$, cause very little change in T_N. Although the presence of diamagnetic aluminum must cause some disruption in the network of superexchange interactions between the iron atoms, the ordering temperature is affected only slightly for such low dopant levels. When the exchange interactions are sufficiently disrupted the ordering temperature drops, as is observed when T_N drops from 240K to 25K for $x = 0.5$ to 1 . At this doping level, the interaction network critical for the high antiferromagnetic

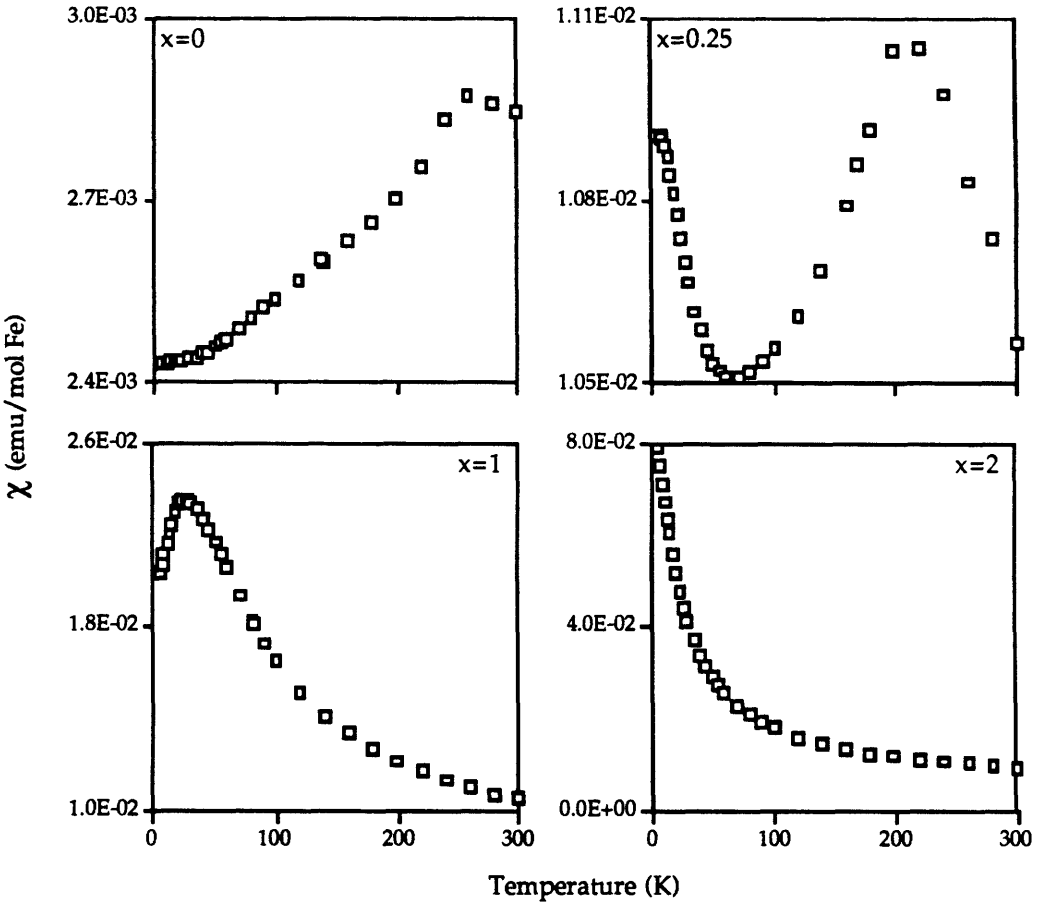

Figure 2.3.5 Susceptibility *vs.* temperature plots for various values of x for the solid solution $Bi_2Fe_{4-x}Al_xO_9$.

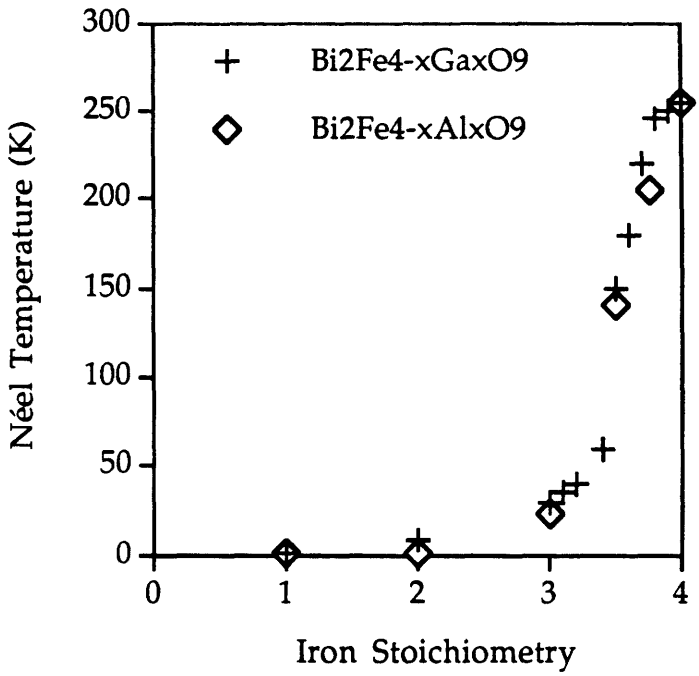

Figure 2.3.6 Néel temperature *vs.* iron stoichiometry for the solid solution $Bi_2Fe_{4-x}Al_xO_9$. Values are compared with $Bi_2Fe_{4-x}Ga_xO_9$ (Section 2.2).

transition temperature is being disrupted. Additional doping causes the transition temperature to decrease gradually toward zero.

The susceptibility below the antiferromagnetic ordering temperature shows field dependence and hysteresis as shown in Figure 2.3.7. Placing a sample into the magnetometer with the applied field on results in magnetic behavior that is ferrimagnetic in appearance, while placing a sample into the magnetometer with the magnetic field off produces behavior that is characteristic of an antiferromagnet. No field history dependent behavior was observed for samples with $0 \leq x \leq 0.5$ as zero-field-cooled and field-cooled samples exhibited identical susceptibility curves.

3. *Mössbauer*

Mössbauer spectra were collected between room temperature and 20K. The spectra are qualitatively similar to that seen for $Bi_2Fe_{4-x}Ga_xO_9$ in Section 2.2.(Figure 2.2.8) Mössbauer parameters for $Bi_2Fe_{4-x}Al_xO_9$, derived from least-square fits of the experimental data to theoretical models are tabulated in Table 2.3.5. At high temperatures (T = 200K) the spectrum of $Bi_2Fe_{3.5}Al_{0.5}O_9$ is composed of the superposition of two quadrupole doublets with isomer shifts and quadrupole splittings δ_1 = 0.21 mm/sec, ΔEQ_1 = 0.85 mm/sec, and δ_2 = 0.46 mm/sec and ΔEQ_2 = 0.56 mm/sec consistent with high spin Fe^{+3} ions in tetrahedral and octahedral environments,[46] respectively. The intensity ratio of the two signals is 47:53 in agreement with the crystallographic structure of the compound which contains equal numbers of tetrahedral and octahedral sites.

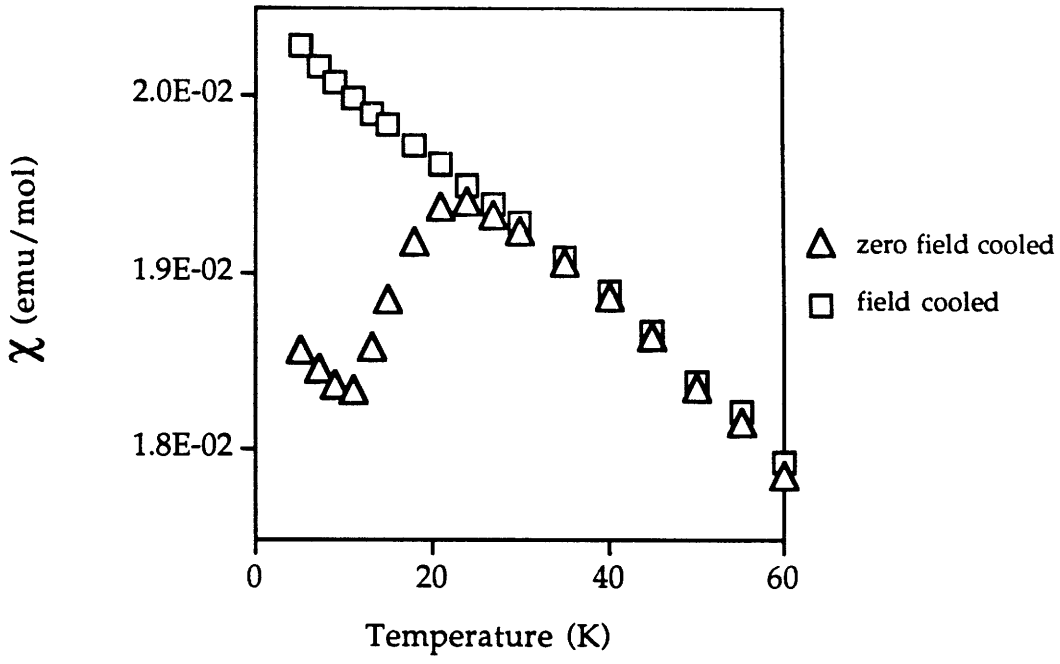

Figure 2.3.7 Hysteresis effect for $Bi_2Fe_3AlO_9$ of susceptibility when cooled in the presence or absence of a magnetic field.

TABLE 2.3.5

Mössbauer parameters for the solid solution $Bi_2Fe_{4-x}Al_xO_9$

x	T (K)	δ (mm/sec)	ΔE_Q or ε (mm/sec)	H_{hf} (kOe)	Γ/2 (mm/sec)	% Area	T_N (K)
0.5	200	0.46	0.56		0.24	53	140
		0.21	0.85		0.21	47	
	120	0.45	0.14	366	0.30	57	
		0.34	0.06	311	0.30	43	
1.0	200	0.48	0.60		0.18	47	25
		0.21	0.83		0.18	53	
	20	0.43	-0.01	455	0.30	48	
		0.34	0.06	400	0.30	52	
2.0	200	0.47	0.64		0.19	50	
		0.21	0.88		0.17	50	

The onset of magnetic hyperfine splitting in the Mössbauer spectra occurs at T_N ~ 140K in agreement with our magnetic measurements. As the temperature decreases, the magnetic hyperfine splitting increases as the magnetization of the compound approaches saturation. At low temperatures, two magnetic subcomponents, which are associated with the octahedral and tetrahedral iron sites, become discernible. There is a slight difference in local saturation magnetic moments between the two subsites that is reflected in the difference of the magnetic hyperfine fields, H(oct) = 366 kOe and H(tet) = 311 kOe at T = 120K.(See Table 2.3.5) The overall magnetic behavior is similar to $Bi_2Fe_{4-x}Ga_xO_9$[30] and is consistent with a 3D antiferromagnetic phase transition. The anomalous broadening behavior indicative of a spin rearrangement phase transition in the Mössbauer spectra of $Bi_2Fe_4O_9$, was not observed in the spectra of the $Bi_2Fe_{4-x}Al_xO_9$ solid solution.[30]

The Mössbauer spectra for all values of **x** showed temperature behavior consistent with 3D magnetic ordering with T_N decreasing with increasing **x**. As was the case for the gallium-doped system,[30] (Figure 2.2.9) it was observed that for all values of **x**, the experimental H_{hf} data followed an S = 5/2 Brillouin functional temperature dependence as expected for a 3D magnetic phase transition described by molecular field theory.[38,39]

C. Discussion

Structurally, the $Bi_2Fe_{4-x}Al_xO_9$ solid solution is similar to the $Bi_2Fe_{4-x}Ga_xO_9$ solid solution discussed in Section 2.2.[30] The lattice parameters are slightly smaller in the aluminum compound due to the smaller radius of aluminum. Lattice parameters change in a linear fashion across the solid solution in the manner described by Vegard's Law.[36] This is to be expected since according to

both diffraction and Mössbauer data, the iron and aluminum atoms are randomly distributed on the octahedral and tetrahedral coordination sites. In $Bi_2Fe_{4-x}Ga_xO_9$, on the other hand, where the gallium had a 3:2 preference for the tetrahedral site. This slight structural difference is characteristic of the crystal chemistry similarities between aluminum and iron and not likely due to the smaller radius of aluminum *vs.* gallium.[47,48]

Rapid drops in the antiferromagnetic phase transition temperature for doping levels exceeding some small threshold level are characteristic of systems having competing magnetic interactions,[43] and have been observed in other iron containing compounds.[49] In the presence of competing magnetic interactions, the magnetic order of the undoped system breaks down rapidly with spin dilution and spin-glass phenomena can occur. The magnetic trends seen in both the $Bi_2Fe_{4-x}Al_xO_9$ solid solution and the $Bi_2Fe_{4-x}Ga_xO_9$ solid solution are consistent with such behavior. The disruption of magnetic order in both systems beyond a threshold dopant level is most likely the result of a spin frustration phenomenon due to competing exchange interactions. The effects of the spin frustration may be seen both in the uncompensated spin region of the $x = 0.25$ compound in Figure 2.3.5 and in the magnetic field history of the $x = 1$ compound shown in Figure 2.3.7.

D. Conclusions

The solid solution $Bi_2Fe_{4-x}Al_xO_9$ has been investigated structurally and magnetically, using X-ray powder diffraction, magnetic susceptibility and Mössbauer spectroscopy. A statistical distribution of aluminum and iron over the octahedral and tetrahedral cation coordination sites was observed. The magnetic ordering behavior, as seen by susceptibility and Mössbauer

measurements, is 3-dimensional in nature, with the ordering temperature dropping rapidly with increasing aluminum doping. This behavior is consistent with the disruption of several competing magnetic exchange interactions and qualitatively analogous with that we have reported previously reported for $Bi_2Fe_{4-x}Ga_xO_9$ in Section 2.2.

Section 2.4: $Bi_2Fe_{4-x}Mn_xO_{9+\delta}$ and $Bi_2Fe_2Mn_2O_{10}$

A. Introduction

Materials with the general formula $Bi_2M_4O_{9+\delta}$ where M = Al, Fe, Ga, and Mn, were first synthesized in 1964.[23,24,50-53] The structural solution was reported in 1968 by Niizeki *et. al.*,[23] who noted that while very closely related, the compound $Bi_2Mn_4O_{10}$ is not actually isostructural to the other three compositions, $Bi_2M_4O_9$ (M = Al, Ga, Fe). The two structures differ only in the position of one oxygen, which, when M = Al, Fe, and Ga, is situated on an inversion center (0, 0, 1/2). When M = Mn, Niizeki found that there is an additional oxygen and the two atoms are related by mirror symmetry, above and below the inversion center at (0, 0, ± 0.281). This extra oxygen changes the coordination of two of the manganese ions from tetrahedral to square pyramidal, resulting in two octahedrally and two square pyramidally coordinated manganese ions. Consequently, the general formulas of the two structures may be written as $Bi_2Mn^{oct}_2Mn^{sqr\ pyr}_2O_{10}$ and $Bi_2M^{oct}_2M^{tet}_2O_9$ where M = Al, Fe, Ga. The manganese is mixed valent and Bertaut *et. al.* [54,55] has inferred that the Mn(IV) is located on the octahedral sites and Mn(III) is located on the square pyramidal sites.

No ordered quaternary phases of the structure type $Bi_2M_4O_{9+\delta}$ have been synthesized and characterized previously. The solid solution

$Bi_2Fe_{4-x}Ga_xO_9$, described in Section 2.2, which has a 60% preferential ordering of iron on the octahedral site [30] has been synthesized and structurally and magnetically characterized. Although the solid solution $Bi_2Fe_{4-x}Mn_xO_{9+\delta}$ has been described in the literature,[51,53] the materials were only poorly characterized and the reports are conflicting. According to Masuno *et. al.*,[51] there exists only limited miscibility on either side of the phase diagram, where $0 \leq x \leq 0.9$ and $3.6 \leq x \leq 4.0$, while in the center a multi-phase region exists containing $Bi_2Fe_4O_9$, $Bi_2Mn_4O_{10}$ and $Bi(Fe,Mn)O_3$. According to Jimenez,[53] a complete solid solution exists across the entire range of x, however, it was assumed that the two end members were actually isostructural, and that therefore their X-ray powder diffraction patterns were identical. This assumption is, in fact, incorrect since upon altering the oxygen coordination, both the structure and the powder pattern change noticeably. In this section, site-specific substitution is described in the $Bi_2Fe_{4-x}Mn_xO_{9+\delta}$ system. The synthesis and single crystal structure of the ordered material $Bi_2Fe_2Mn_2O_{10}$ is presented.

B. Experimental

1. Sample preparation

Crystals of $Bi_2Fe_2Mn_2O_{10}$ were grown in a Bi_2O_3 flux using stoichiometric amounts of Fe_2O_3 (Cerac 99.99%) and Mn_2O_3 (Cerac 99.99%) in a five-fold excess of Bi_2O_3 (Cerac 99.9%). The resulting 12 gram charge was thoroughly mixed in a platinum crucible and heated at 5°/minute to 1000°C. The flux was soaked for five days and slow-cooled at a rate of 5°/hour to 700°C. The furnace was then rapidly cooled to room temperature. The black, shiny crystalline product was separated from the flux matrix by dissolving the flux

in dilute HNO_3. Single crystals which grew as prisms, some up to 1 mm on edge, were isolated mechanically. It should be noted, however, that the flux experiment crystallized multiple products. Crystals of $Bi_2Mn_4O_{10}$ and $Bi(Fe,Mn)O_3$ were also isolated from the flux matrix.

2. *Crystallographic studies*

The crystals obtained from the flux growth were first analyzed by precession photos using a Charles Supper Co. precession camera with a crystal to film distance of 59 mm, and a precession angle of 10° mounted on an Enraf-Nonius 581 Diffractis X-ray generator. Careful selection enabled a single, untwinned crystal of the appropriate stoichiometry to be chosen for structure solution. The diffraction patterns seen by precession photos were consistent with the structure of the related material $Bi_2Mn_4O_{10}$ but the lattice parameters differed.

A crystal of $Bi_2Fe_2Mn_2O_{10}$ having the approximate dimensions of 0.060 x 0.050 x 0.040 mm was chosen for the single-crystal structure determination. All measurement were made on a Rigaku AFC6R diffractometer with graphite monochromated Mo Kα radiation (λ = 0.71069 Å) and a 12kW rotating anode generator. Crystallographic data are summarized in Table 2.4.1.

Energy dispersive spectroscopy, (EDS), was performed to determine the presence of bismuth, iron and manganese using the same crystal that was analyzed crystallographically. Wavelength dispersive spectroscopy, (WDS), was performed using a JEOL 781 microprobe to ascertain the exact metal stoichiometry.

TABLE 2.4.1

Summary of Crystallographic data for $Bi_2Fe_2Mn_2O_{10}$

Empirical Formula	$Bi_2Fe_2Mn_2O_{10}$
Formula weight	799.52
Crystal color, habit	black, prismatic
Crystal dimensions (mm)	0.060 x 0.050 x 0.040
Crystal system	orthorhombic
Space group	Pbam (No. 55)
No. reflections used for unit cell Determination (2Θ range)	24 (12.8 - 27.3 °)
Omega scan peak width at half height	0.30
Lattice parameters (Å)	
a	7.617 (3)
b	8.548 (4)
c	5.830 (3)
Volume ($Å^3$)	379.6(3)
Z	2
D_{calc} (g/cm^3)	6.994
F_{000}	696
Diffractometer	Rigaku AFC6R
Radiation	Mo Kα (λ = 0.71069 Å)
μ (Mo Kα) (cm^{-1})	529.43
Temperature (° C)	23
Scan type	ω–2Θ
$2\Theta_{max}$	54.9°
No. of Reflections Measured	549
No. Observations (I > 3.00 σ(I))	358
No. Variables	31
Corrections	Lorentz-polarization Absorption (trans. factors: 0.72 - 1.41) Secondary Extinction (coefficient: 0.55208E-06)
Residuals: R; R_W	0.042; 0.052
Goodness of fit Indicator	1.82
Max. peak in Final Difference Map	3.69 e^-/ $Å^3$

Cell constants and an orientation matrix for data collection, obtained from a least-squares refinement using the setting angles of 24 carefully centered reflections in the range of $12.79 < 2\Theta < 27.30°$ correspond to an orthorhombic cell with the dimensions: a = 7.617(3) Å, b = 8.548(4) Å, c = 5.830(3) Å, V = 379.6(3) $Å^3$. For Z = 2 and the F.W. 799.52, the calculated density is 6.994 g/cm^3. Based on the systematic absences of: 0kl : $k \neq 2n$ and h0l: $h \neq 2n$, packing considerations, a statistical analysis of intensity distribution and the successful solution and refinement of the structure, the space group was determined to be Pbam (#55).

The data were collected at a temperature of 23 ± 1°C, using the $\omega-2\Theta$ scan technique to a maximum 2Θ value of 54.9°. Omega scans of several intense reflections, made prior to data collections, had an average width at half-height of 0.30° with a take-off angle of 6.0°. Scans of $(1.21 + 0.35 \tan\Theta)°$ were made at a speed of 8.0°/minute (in omega). The weak reflections ($I < 10.0\sigma(I)$) were rescanned (maximum of eight rescans) and the counts were accumulated to assure good counting statistics. Stationary background counts were recorded on each side of the reflection. The ratio of peak counting time to background counting time was 2 : 1. A total of 549 reflections were collected. The intensities of three representative reflections which were measured after every 150 reflections remained constant throughout data collection indicating crystal and electronic stability (no decay correction was applied). Data were corrected for Lorentz, polarization, absorption[31] and secondary extinction. Data were empirically corrected for absorption by means of DIFABS.[32]

All calculations were performed on a MicroVAX 3500 with the use of TEXSAN crystallographic software.[33] The structure was solved by direct

methods,[34] and refinement was performed using a full-matrix least-squares calculation. The final values of the discrepancy factors were R = 0.042 ($R = \Sigma \| |F_o| - |F_c| \| / \Sigma |F_o| = 0.042$) and $R_w = 0.052$ ($R_w = \{(\Sigma w (|F_o| - |F_c|)^2 / \Sigma w F_o^2)\}^{1/2} = 0.052$), $w = 4F_o^2/\sigma^2(F_o^2)$. The goodness of fit was 1.82 and the highest peak in the final difference map was 3.69 $e^-/Å^3$. The atomic scattering factors were those of Cromer and Waber and corrections for anomalous dispersion were from Cromer.[31,35]

C. Results

Final atomic positions and anisotropic U values are listed in Table 2.4.2 and Table 2.4.3, respectively. Selected interatomic distances are listed in Table 2.4.4.

A view parallel to the **ab**-plane of $Bi_2Fe_2Mn_2O_{10}$ is shown in Figure 2.4.1 (the bismuth-oxygen bonds have been omitted for clarity). It consists of columns of edge-sharing octahedra which are corner-shared with edge-sharing square pyramids as shown in an expanded view in Figure 2.4.2. The octahedra are located in layers that are separated by doubly packed square pyramidal layers. These layers form slabs of alternating octahedral-square pyramidal-octahedral coordination. The slabs in turn are separated from each other by planes of bismuth and oxygen which are regularly modulated in the **b**-direction (Figure 2.4.3). The octahedra are connected across the square pyramid and bismuth oxide layer *via* edge-sharing oxygens located in the square pyramidal and bismuth oxide plane, respectively. The transition metal cations are segregated to a single site. The manganese ions are located only on the square pyramidal sites and the iron ions are located only on octahedral sites. The iron octahedra are slightly tetragonally distorted, the longest bond being only 0.09Å

TABLE 2.4.2

Positional and Isotropic Equivalent Thermal Parameters for $Bi_2Fe_2Mn_2O_{10}$

Atom	x	y	z	B(eq)
Bi	0.15798(12)	0.16424(13)	0	0.74(5)
Fe	1/2	0	0.2574(6)	0.3(1)
Mn	0.3924(5)	0.3489(5)	1/2	0.7(1)
O(1)	0	0	0.291(4)	1.7(4)
O(2)	0.384(2)	0.200(2)	0.250(2)	1.0(2)
O(3)	0.639(2)	0.078(2)	1/2	1.1(3)
O(4)	0.156(2)	0.441(2)	0	0.3(3)

TABLE 2.4.3

u_{ij} or U values (x 100) for $Bi_2Fe_2Mn_2O_{10}$ in $Å^2$

Atom	u_{11} (U)	u_{22}	u_{33}	u_{12}
Bi	0.93(6)	0.96(6)	0.94(6)	0.11(4)
Fe	0.19(13)	0.5(2)	0.4(2)	0.1(2)
Mn	1.4(2)	0.9(2)	0.3(2)	0.5(2)
O(1)	2.2(5)			
O(2)	1.3(3)			
O(3)	1.3(4)			
O(4)	0.4(4)			

TABLE 2.4.4

Bond distances in $Bi_2Fe_2Mn_2O_{10}$

Atom	Atom	distance	Atom	Atom	distance
Bi	O(1)	2.508(15)	Fe	O(4)	1.978(11)
Bi	O(2)	2.275(13)	Fe	Fe	2.829(7)
Bi	O(4)	2.369(18)	Fe	Fe	3.001(7)
Bi	O(4)	2.375(17)	Fe	Mn	3.401(5)
Bi	Fe	3.318(2)	Fe	Mn	3.550(4)
Bi	Fe	3.455(2)	Mn	O(1)	1.957(14)
Bi	Mn	3.550(3)	Mn	O(2)	1.940(14)
Fe	O(2)	1.923(14)	Mn	O(3)	2.026(19)
Fe	O(3)	1.891(13)			

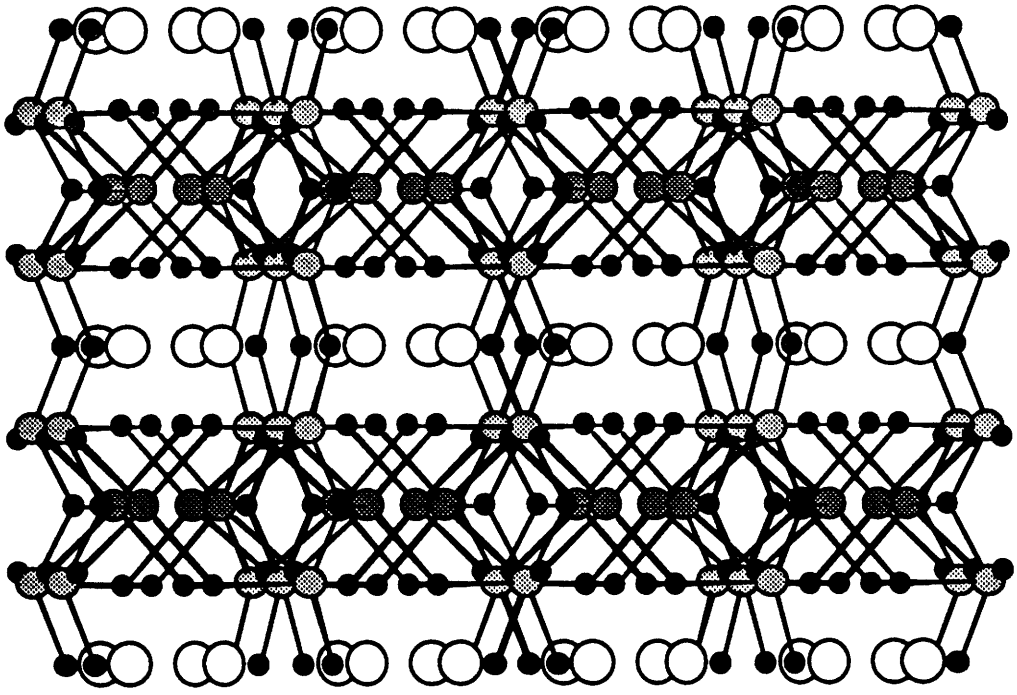

Figure 2.4.1 View of the structure of $Bi_2Fe_2Mn_2O_{10}$ parallel to the ab-plane. Bismuth: ◯ ; Iron: ◍ ; Manganese: ● ; Oxygen: ◍ .

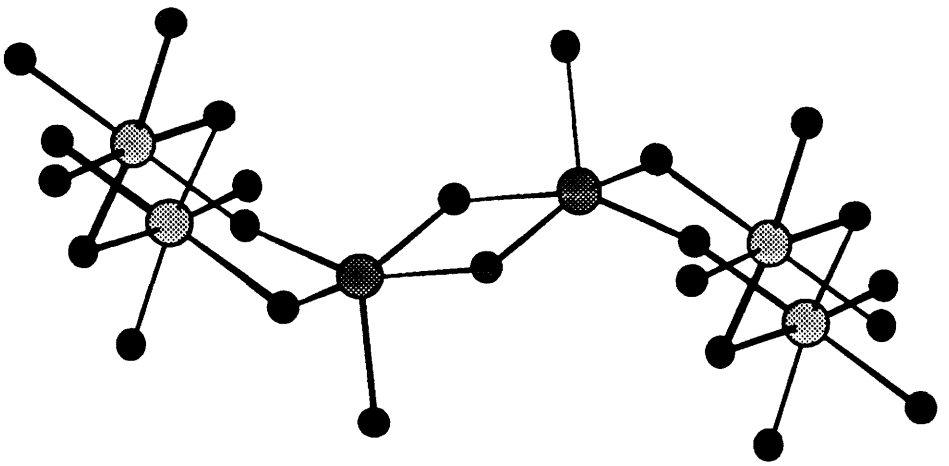

Figure 2.4.2 View of the local symmetry of the edge-shared square pyramids and edge-shared octahedra in $Bi_2Fe_2Mn_2O_{10}$. Iron: ◎ ; Manganese: ● ; Oxygen: ◎.

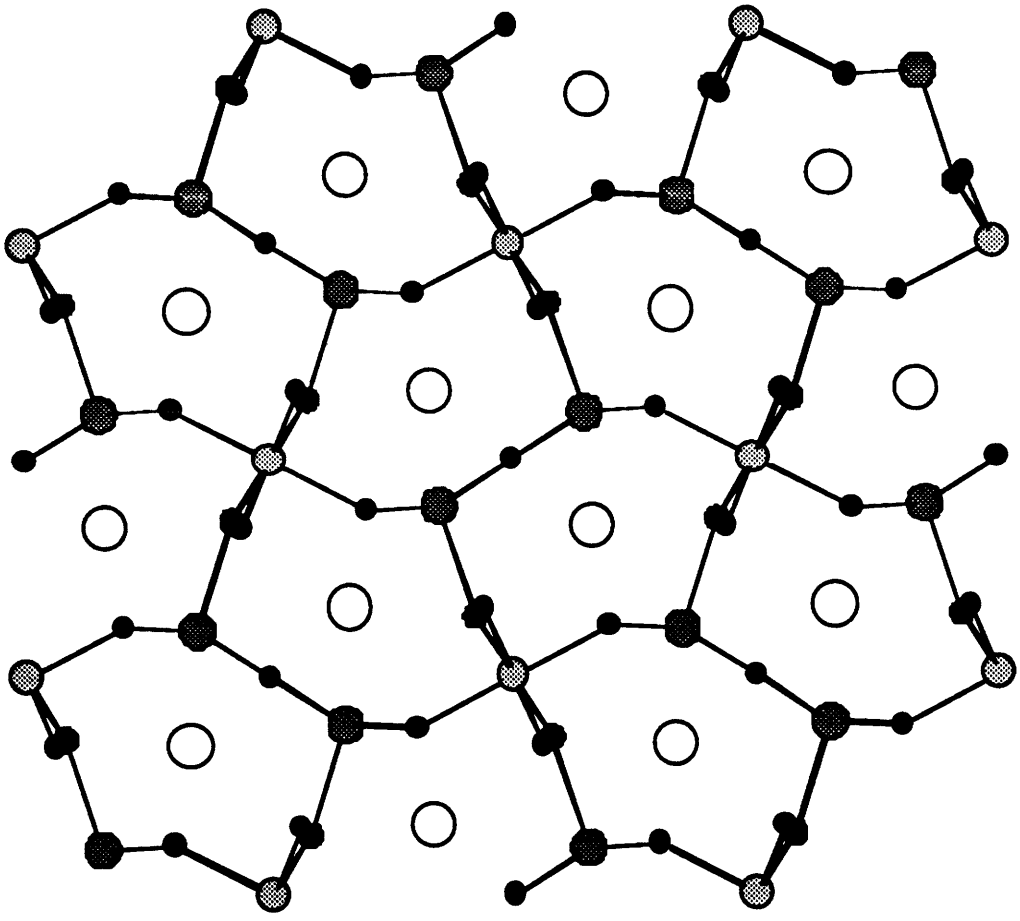

Figure 2.4.3 View perpendicular to the **ab**-plane in $Bi_2Fe_2Mn_2O_{10}$. Planes are more modulated than in either $Bi_2Fe_{4-x}Ga_xO_9$ or $Bi_2Fe_{4-x}Al_xO_9$ due to the extra oxygen which makes the square pyramidal coordination of manganese. Bismuth: ◯ ; Iron: ◍ ; Manganese: ● ; Oxygen: ⊙.

longer than the shortest bond, which point toward the bismuth oxide plane and the next edge-shared octahedron, respectively. The Fe-O bond which corner-shares with the square pyramids is slightly bent toward the square pyramid, which are virtually undistorted in bond lengths and angles; the apical oxygen bond is 0.09 Å longer than the basal oxygen bonds. The bismuth atoms are located at the apices of trigonal pyramids formed by three Bi-O bonds of varying lengths from 2.27 to 2.38Å. If second- and third-nearest neighbors are included the bismuth ions are surrounded by ten oxygen atoms. All oxygens in the structure are tetrahedrally coordinated.

A view perpendicular to the **ab**-plane, Figure 2.4.3, shows a complicated packing network of distorted ten-membered rings of metal and oxygen atoms. The ten-fold rings are made up of polygons in repeating groups of octahedron - square pyramid - square pyramid - octahedron - square pyramid. The two middle square pyramids are edge-shared to each other, however, the remaining contacts are *via* corners. The order of planes going into the page is bismuth - octahedral sites - square pyramidal sites - octahedral sites - bismuth (the bismuth-oxygen bonds have been omitted for clarity).

EDS results from the crystal used for crystallography showed the concentrations of bismuth, manganese and iron to be approximately equal. WDS analysis determined the resulting stoichiometry to be $Bi_{2.0}Fe_{2.1}Mn_{1.9}O_{10}$. The two coordination sites in the structural solution were analyzed with iron and manganese in both sites and with both iron and manganese mixed in a single site. The site multiplicities were refined, and the residual values which resulted from these refinements were found to be lowest when iron and manganese were placed only on the octahedral and square pyramidal site, respectively.

D. Discussion

The manganese in the $Bi_2Mn_4O_{10}$ structure is mixed valent with the two oxidation states of manganese reported to be segregated in specific coordination sites.[54,55] Although the manganese atoms are indeed segregated by oxidation state, from the results based on the structure of $Bi_2Fe_2Mn_2O_{10}$, it is believe that the previously reported assignment is incorrect. From a careful analysis of the two transition metal sites in the $Bi_2Mn_4O_{10}$ and the $Bi_2Fe_4O_9$ structures it is believed that the Mn(III) is located in the octahedral sites while the Mn(IV) is located in the square pyramidal sites. The distortion present in the octahedral sites of $Bi_2Mn_4O_{10}$ *vs.* $Bi_2Fe_4O_9$, and the knowledge that Fe(III), d^5, sits in the octahedral sites of $Bi_2Fe_4O_9$ implies that a Jahn-Teller ion, Mn(III), d^4, may occupy the site in $Bi_2Mn_4O_{10}$. Although Mn(III) may prefer square pyramidal geometry over Mn(IV) in some cases, it is unlikely that Mn(IV) would sit in the distorted octahedral geometry seen in $Bi_2Mn_4O_{10}$. Supporting this assignment are the similarities of the octahedral sites of $Bi_2Fe_2Mn_2O_{10}$ and $Bi_2Fe_4O_9$.

Assuming the manganese(IV) atoms in $Bi_2Mn_4O_{10}$ reside only on square pyramidal sites, the manganese in $Bi_2Fe_2Mn_2O_{10}$ should also be square pyramidal Mn(IV). The octahedra are then occupied strictly by iron atoms suggesting that certain similarities should exist between the octahedral sites in $Bi_2Fe_2Mn_2O_{10}$ and those in $Bi_2Fe_4O_9$. In fact, the octahedral angles are more akin to those found in the all iron compound than in the all manganese compound.(Table 2.4.5)

The O(3) - Fe - O(4) angle is the widest found in all of the compounds. O(4) is located in the Bi - O layer, while O(3) is an edge-shared octahedral oxygen as

well as the apical oxygen for the square pyramid. This angle is widened for two reasons: (1) unlike the all iron compound, O(3) is attached to a square pyramid which has a broader basal plane than the tetrahedron found in $Bi_2Fe_4O_9$, widening the angle, and (2) in $Bi_2Mn_4O_{10}$ a Jahn-Teller ion, Mn(III), is situated in the octahedral sites instead of Fe(III) causing greater distortion. The Jahn-Teller ion distorts the octahedra in $Bi_2Mn_4O_{10}$ away from the more ideal situation found in $Bi_2Fe_2Mn_2O_{10}$. The octahedral bond lengths are also similar to those present in $Bi_2Fe_4O_9$, except for the bonds shared between octahedra and square pyramids; these bonds are more similar to those found in $Bi_2Mn_4O_{10}$, where the basal plane of the square pyramid contacts more closely with the octahedra due to the presence of the extra oxygen site, as compared to a tetrahedral-octahedral contact.

The square pyramid is more regular in $Bi_2Fe_2Mn_2O_{10}$ than in $Bi_2Mn_4O_{10}$. The four lengths in the basal plane are all equal, unlike in $Bi_2Mn_4O_{10}$, where one side of the base is longer than both the opposite side and the apical bond. The base plane angles are slightly contracted toward the edge-sharing (square pyramidal) direction and expanded in the corner-shared(octahedral) direction. The apical metal-oxygen bond is approximately 0.1 Å longer than the metal-oxygen bond in the base plane.

The Bi-O planes are regularly modulated in the **b** -direction, as has been seen in other layered bismuth oxides.[56] The modulation is more pronounced in $Bi_2Fe_2Mn_2O_{10}$ than either $Bi_2Fe_4O_9$ or $Bi_2Mn_4O_{10}$. This is due to the edge-sharing square pyramids allowing for smoother modulation in comparison with the corner-sharing tetrahedra. The absence of the Jahn-Teller distortion in the $Bi_2Fe_2Mn_2O_{10}$ octahedra also contributes to the enhanced modulation.

TABLE 2.4.5

Comparison of cation coordination angles and bond lengths

oct. angles(°)	$Bi_2Mn_4O_{10}$[a]	$Bi_2Fe_4O_9$[a]	$Bi_2Fe_2Mn_2O_{10}$	$Bi_2Fe_2Ga_2O_9$[b]
O(3) - Fe - O(4)	96.1	97.4	98.2	96.4
O(4) - Fe - O(4)	80.5	82.1	81.2	83.0
O(2) - Fe - O(3)	93.4	92.7	94.4	95.4
O(2) - Fe - O(4)	88.4	91.0	91.8	91.9
O(2) - Fe - O(3)	89.9	88.8	87.8	89.0
O(2) - Fe - O(4)	88.1	87.4	86.0	83.6
oct. lengths (Å)	$Bi_2Mn_4O_{10}$	$Bi_2Fe_4O_9$	$Bi_2Fe_2Mn_2O_{10}$	$Bi_2Fe_2Ga_2O_9$
Fe - O(2)	1.83	1.95	1.923(14)	2.025(13)
Fe - O(3)	1.90	1.95	1.891(13)	1.951(14)
Fe - O(4)	1.98	2.05	1.978(11)	2.041(14)
sq. pyr. angles(°)	$Bi_2Mn_4O_{10}$		$Bi_2Fe_2Mn_2O_{10}$	
O(1) - Mn - O(1)	82.9		77.0	
O(2) - Mn - O(2)	86.7		97.6	
O(3) - Mn - O(1)	97.0		101.4	
O(3) - Mn - O(2)	100.4		99.8	
O(1) - Mn - O(2)	92.6		88.8	
sq. pyr. lengths(Å)	$Bi_2Mn_4O_{10}$		$Bi_2Fe_2Mn_2O_{10}$	
Mn - O(1)	1.91		1.957(14)	
Mn - O(2)	2.10		1.940(14)	
Mn - O(3)	2.04		2.026(19)	

[a] values from Niizeki, *et al*; [23] the final R values are 0.11 and 0.10 for the Mn and Fe compounds, respectively,
[b] values from Giaquinta, *et al*; [30] the final R value is 0.053.

E. Conclusions

The crystal structure of $Bi_2Fe_2Mn_2O_{10}$ was determined by single crystal X-ray diffraction. The structure has ordered transition metals which are located in octahedral and square pyramidal sites for iron and manganese, respectively. This is the first truly ordered compound with the $Bi_2M_4O_{9+\delta}$, (M = Al, Fe, Ga, Mn) structure. Since Fe(III) is located on octahedral site, there is no Jahn-Teller distortion of the octahedra as is observed in $Bi_2Mn_4O_{10}$. The oxidation state of the manganese is +4, accounting for the extra oxygen found in $Bi_2Fe_2Mn_2O_{10}$ *vs.* $Bi_2Fe_4O_9$. The Bi-O planes are regularly modulated in the **b**-direction as has been seen in other layered bismuth oxides. This modulation is more pronounced in $Bi_2Fe_2Mn_2O_{10}$ than in either $Bi_2Fe_4O_9$ or $Bi_2Mn_4O_{10}$. Based on the structure of $Bi_2Fe_2Mn_2O_{10}$, it is believed that the previously reported cation arrangement in $Bi_2Mn_4O_{10}$ is, in fact, incorrect.

Section 2.5: Comparisons within the $Bi_2Fe_{4-x}M_xO_{9+\delta}$ system

The solid solutions $Bi_2Fe_{4-x}Ga_xO_9$ and $Bi_2Fe_{4-x}Al_xO_9$ are qualitatively similar. Both gallium and aluminum substitute into the $Bi_2Fe_{4-x}M_xO_9$ structure for all values of **x**. The magnetic characteristics of the two systems both display sudden drops in the transition temperature with only small doping levels indicative of magnetic systems with competing interactions. Both systems display spin-glass-like behavior magnetic history dependence upon reaching a critical doping level.

Although the smaller radius of aluminum *vs.* gallium reduces the unit cell parameters slightly, the most important difference between the two systems is the distribution of the cations within the two coordination geometries. In the

case of $Bi_2Fe_{4-x}Ga_xO_9$, iron prefers the octahedral geometry by slightly more than a statistical value, 60%. This distribution was determined independently by both single crystal X-ray structure analysis and Mössbauer spectroscopy. In light of the previously studied $(Ga,Fe)_2O_3$ system,[25-27] this distribution is surprising only in its lack of further segregation by the gallium atoms to the tetrahedral position. In the $Bi_2Fe_{4-x}Al_xO_9$ system, however, the two metal cations share both cation geometries with equal probability. Because aluminum is a smaller, more electropositive metal than gallium, it may be expected to prefer an octahedral coordination more strongly. In fact, in corundum, the stable phase of aluminum oxide, α-Al_2O_3, the aluminum atoms are located in only octahedral sites,[57] while in the stable gallium oxide phase, β-Ga_2O_3, the gallium atoms are in only tetrahedral positions.[58] Furthermore, the crystal chemistry of aluminum and iron is known to be more similar than that of gallium and iron. Iron and aluminum often crystallize in similar structures, and are known to substitute for each other regularly.[47] However, iron and gallium crystallize in different structures, even with the same ions, *e.g.* $YFeO_3$ *vs.* $YGaO_3$.[48]

Only in the $Bi_2Fe_{4-x}Mn_xO_{10}$ system was site-specific substitution actually achieved. Perhaps the crucial difference between coordination sites is electronic in nature, and only in the case of transition metals which use *d*-electrons in bonding in two different coordination geometries could a true site preference be determined between two elements. Since Fe(III), d^5, preferred the octahedral site and Mn(IV), d^3, the square pyramidal, the explanation for this segregation may lie in the number of unpaired *d*-electrons. With five unpaired electrons for all high spin coordinations, Fe(III) realistically, could sit in either site. However, populating the d_z^2 orbital with

the fifth electron in the square pyramid should effect a lengthening and weakening of the apical bond, a characteristic which was not observed. Alternatively, an undistorted octahedral geometry can easily be assumed by high spin iron(III). Manganese(IV), with three unpaired electrons, is a Jahn-Teller ion in square pyramidal coordination, but perhaps the least energy configuration is, in fact, the one with the unpopulated square pyramidal d_z^2 orbital: Fe(III) in octahedral coordination and Mn(IV) in square pyramidal coordination. This view is supported by the fact that the octahedral site is virtually undistorted and the square pyramidal site is not apically distorted as would be predicted. In fact, the lack of bonding *d*-electrons in both aluminum and gallium may be one reason why both these elements are non-specific dopants in the $Bi_2Fe_{4-x}M_xO_{9+\delta}$ systems.

References

(1) Aurivillius, B. Ark. Kemi (1949) **1**, 463.

(2) Aurivillius, B. Ark. Kemi (1949) **1**, 499.

(3) Aurivillius, B. Ark. Kemi (1950) **2**, 519.

(4) Chu, C. W.; Bechtold, J.; Gao, L.; Hor, P. H.; Huang, Z. J. Phys. Rev. Lett. (1988) **60**, 941.

(5) Fukuhara, M.; Bhalla, A. S.; Mulay, L. N.; Newnham, R. E. J. Mater. Res. (1989) **4**, 273.

(6) Goodenough, J. B.; Manthiram, A. J. Solid State Chem. (1990) **88**, 115.

(7) Müller-Buschbaum, H. Angew. Chem. (1989) **101**, 1503.

(8) Raveau, B.; Michel, C.; Hervieu, M.; Groult, D.; Provost, J. J. Solid State Chem. (1990) **85**, 181.

(9) Sleight, A. W. Science (1988) **242**, 1519.

(10) Sharma, V.; Shukla, A. K.; Gopalakrishnan, J. Solid State Ionics (1992) **58**, 359.

(11) Thomas, J.; Anderson, M. E.; Krause, W. E.; zur Loye, H.-C. Mat. Res. Soc. Symp. Proc. (1993) **293**, 295.

(12) Thomas, J.; Krause, W. E.; zur Loye, H.-C. Mat. Res. Soc. Symp. Proc. (1993) **293**, 307.

(13) Kendall, K.; zur Loye, H.-C. Solid St. Ion. (1993) in press.

(14) Aurivillius, B. Phys. Rev. (1962) **126**, 893.

(15) Subbarao, E. C. J. Phys. Chem. Solids (1962) **23**, 665.

(16) Newnham, R. E.; Wolfe, R. W.; Dorrian, J. F. Mat. Res. Bull. (1971) **6**, 1029.

(17) Yee, K. A.; Albright, T. A.; Jung, D.; Whangbo, M. Angew. Chem. Int. Ed. Engl. (1989) **28**, 750.

(18) Maeda, H.; Tanaka, Y.; Fukutomi, T.; Asano, T. Jap. J. Appl. Phys. (1988) **27**, L209.

(19) Le Page, Y.; McKinnon, W. R.; Tarascon, J.-M.; Barboux, P. Phys. Rev. B (1989) **40**, 6810.

(20) Tarascon, J. M.; Miceli, P. F.; Barboux, P.; Hwang, D. M.; Hull, G. W.; Giroud, M.; Greene, L. H.; LePage, Y.; McKinnon, W. R.; Tselepis, E.; Pleizier, G.; Eibschutz, M.; Neumann, D. A.; Rhyne, J. J. Phys. Rev. B (1989) **39**, 11587.

(21) *Crystal Chemistry and Properties of Materials with Quasi-One-Dimensional Structures*; Rouxel, J., Ed.; D. Reidel Publishing Company: Dordrecht, 1986.

(22) Shamir, N.; Gurewitz, E.; Shaked, H. Acta Crystallogr. (1978) **A34**, 662.

(23) Niizeki, N.; Wachi, M. Z. Kristallogr. (1968) **127**, 173.

(24) Tutov, A. G.; Myl'nikova, I. E.; Parfenova, N. N.; Bokov, V. A.; Kizhaev, S. A. Sov. Phys. Solid State (1964) **6**, 963.

(25) Remeika, J. P. J. Appl. Phys. (1960) **31**, 263S.

(26) Abrahams, S. C.; Reddy, J. M. Phys. Rev. Lett. (1964) **13**, 688.

(27) Abrahams, S. C.; Reddy, J. M.; Bernstein, J. L. J. Chem. Phys. (1965) **42**, 3957.

(28) Rado, G. T. Phys. Rev. Lett. (1964) **13**, 335.

(29) Giaquinta, D.; zur Loye, H.-C. J. Alloys and Compounds (1992) **184**, 151.

(30) Giaquinta, D.; zur Loye, H.-C.; Papaefthymiou, G. C.; Davis, W. M. J. Solid State Chem. (1992) **99**, 120.

(31) Cromer, D. T.; Waber, J. T. In *International Tables for X-ray Crystallography Table: 2.2A* The Kynoch Press: Birmingham, England, 1974; Vol. IV.

(32) Walker, N.; Stuart, D. Acta Crystallogr. (1983) **A39**, 158.

(33) Swepston, P. N. In Molecular Structure Corporation: 1985.

(34) Gilmore, C. J. J. Appl. Crystallogr. (1984) **17**, 42.

(35) Cromer, D. T.; Waber, J. T. In *International Tables for X-ray Crystallography, Table: 2.3.1* The Kynoch Press: Birmingham, England, 1974; Vol. IV.

(36) West, A. R. *Solid State Chemistry and its Applications*; Wiley: New York, 1984.

(37) Carlin, R. L. *Magnetochemistry*; Springer-Verlag: Berlin, 1986.

(38) Fisher, M. E. Philos. Mag. (1962) **7**, 1731.

(39) deJonhgh, L. J.; Miedema, A. R. Adv. Phys. (1974) **23**, 1.

(40) Gubbens, P. C. M.; Van Der Kraan, A. M. J. Less-Common Met. (1990) **163**, 165.

(41) Denissen, C. J. M.; De Mooij, B. D.; Buschow, K. H. J. J. Less-Common Met. (1988) **142**, 195.

(42) Sinitsyn, E. V.; Nikolov, O.; Tomov, T.; Ruskov, T.; Ivanov, S. I. Sov. Phys. Solid State (1987) **29**, 573.

(43) Scholl, F.; Binder, K. Z. Physik B (1980) **39**, 239.

(44) Goshen, S.; Mukamei, D.; Shaked, H. J. Appl. Phys. (1969) **40**, 1590.

(45) Larson, A. C.; von Dreele, R. B. In GSAS: General Structure Analysis System, Los Alamos National Laboratory: Los Alamos, NM, 1990.

(46) Greenwood, N. N.; Gibb, T. C. *Mössbauer Spectroscopy*; Chapman and Hall: London, 1971.

(47) Jaffe, H. W. *Crystal Chemistry and Refractivity*; Cambridge University Press: Cambridge, 1988.

(48) Marezio, M.; Remeika, J. P.; Dernier, P. D. Mat. Res. Bull. (1966) **1**, 247.

(49) Dormann, J. L.; Nogues, M. J. Phys.: Condens. Matter (1990) **2**, 1223.

(50) Koizumi, H.; Niizeki, N.; Ikeda, T. Japan J. Appl. Phys. (1964) **3**, 495.

(51) Masuno, K. Nip. Kag. Zasshi (1967) **88**, 726.

(52) Tutov, A. G.; Markin, V. N. Neorg. Mater. (1970) **6**, 2014.

(53) Jimenez, C. M. Bol. Soc. Esp. Ceram. Vidr. (1978) **17**, 365.

(54) Bertaut, E. F.; Buisson, G.; Quezel-Ambrunaz, S. C.R. Acad. Sc. Paris (1964) **258**, 3025.

(55) Bertaut, E. F.; Buisson, G.; Quezel-Ambrunaz, S.; Quezel, G. Solid State Comm. (1967) **5**, 25.

(56) Tarascon, J. M.; LePage, Y.; McKinnon, W. R. Eur. J. Solid State Inorg. Chem. (1990) **27**, 81.

(57) Wells, A. F. *Structural Inorganic Chemistry;* 5th ed.; Clarendon Press: Oxford, 1984.

(58) Tippens, H. H. Phys. Rev. (1965) **140A**, 316.

CHAPTER 3

SYNTHESIS AND CHARACTERIZATION OF NEW MAIN GROUP - TRANSITION METAL OXIDES

Section 3.1: New ternary oxides with new structures

A. Introduction

The synthesis of new materials with new, simple structures is unusual in the study of ternary (ABO_3) transition metal oxides. Since oxides have been studied more often than other solid state materials, such synthesis is uncommon for two reasons, **(1)** it is expected that compounds with simple stoichiometries would have been discovered during previous studies of ternary oxide phase diagrams, and **(2)** it is unusual to discover novel structures in the study of ternary transition metal oxides. More commonly, newly prepared ABO_3 compounds will crystallize in one of the known structure types, such as corundum, bixbyite, or perovskite, depending on the radius ratio of the **A** and **B** cations in question. This will be discussed in Chapter 4. It is therefore of great interest to prepare and study compounds with new stoichiometries and structures simply because **(a)** they are so uncommon, **(b)** the synthesis and characterization of new materials makes it possible to discover new and novel properties, and **(c)** through an analysis of structure, composition, and properties it is possible to determine the underlying principles of structure-property and structure-composition relationships in solid state materials. In this chapter, the structure and magnetic properties of the indium transition metal oxides $InMnO_3$, $InFeO_3$ and their solid solution, $InMn_{1-x}Fe_xO_3$, are described. This is the first reported single crystal structure of a transition metal oxide with this layered, hexagonal structure type as well as the first characterization of their magnetic structures. These materials were characterized by single crystal X-ray diffraction, powder X-ray and neutron diffraction, magnetic susceptibility and Mössbauer spectroscopy.

B. Background

Sesquioxides of indium, manganese, and iron oxides form in both the corundum and C-M_2O_3 structures under the appropriate conditions.[1] Surprisingly, the structure of $InMnO_3$ and $InFeO_3$ is related to neither the corundum nor the C-M_2O_3 structures. Instead, the structure of $InMO_3$, M = Mn, Fe, resembles most closely the hexagonal rare earth manganate and rare earth aluminate structures.[2,3] Although multiphase, polycrystalline samples of $InFeO_3$ have been reported in the literature,[4,5] the single crystal structure has not been previously determined. The existence of $InMnO_3$ was not reported previously.

Structures of ternary compounds may be predicted by several methods including **(a)** extrapolations based on the structure of starting materials and common ternary structure types,[6-14] and **(b)** the calculation of geometric relationships, such as Goldschmidt's tolerance factor,[15] based on the ionic radii of component elements. The two largest $\mathbf{ABO_3}$ structural families are distinguished by (1) **A** and **B** cations of a size suitable to reside in the octahedral interstices of a closest-packed oxygen lattice, and (2) an **A** cation which can form AO_3 closest-packed layers.[1] Oxides of the first group tend to adopt sesquioxide structures,[1,14,16,17] while oxides of the second group form linked BO_6 octahedra and AO_3 closest-packed layers,[6,7,18,19] as well as more unusual structure types.[2,20-22] These structure types will be discussed in greater detail in Chapter 4.

Because the general families of $\mathbf{ABO_3}$ materials are distinguished by a relationship between the sizes of the **B** cation and the **A** cation, radius ratios are helpful in separating the two families of compounds. The Goldschmidt

tolerance factor, $t = (r_A + r_O)/\sqrt{2}(r_B + r_O)$, where r_A, r_B, and r_O are the ionic radii of **A**, **B** and O^{2-} respectively, predicts the perovskite structure for $1 > t > 0.8$, and the ilmenite structure for $0.8 \geq t$. In_2O_3, Mn_2O_3 and Fe_2O_3 are known in both the bixbyite (an anion deficient fluorite structure) and corundum structures and, consequently, one would expect an ABO_3 indium manganese or indium iron oxide to form a derivative of one of those two structure types. Furthermore, the tolerance factor for $InMnO_3$ and $InFeO_3$ is 0.80, confirming that ilmenite, the ordered corundum structure, should form. It is therefore surprising to find $InMO_3$, M = Mn, Fe, in this very simple, yet unusual, layered hexagonal structure with two different cation coordination environments: octahedral and trigonal bipyramidal.

Section 3.2: $InMnO_3$

A. Experimental

1. Preparation of single crystals

Single crystals of $InMnO_3$ were prepared from In_2O_3 (Cerac, 99.99%) and Mn_2O_3 (Cerac 99.99%) in a Bi_2O_3 (Cerac 99.9%) flux. Approximately 3 mmol of the binary oxides were ground together and pelletized. The flux to reactants ratio was 1:1:1. The pellet was heated at 950°C for three days in air on platinum foil and quenched to room temperature. Partial melting of the pellet occurred during the heating cycle and black hexagonal plates of $InMnO_3$ were visible on the surface of the pellet. The flux matrix was weakened with concentrated nitric acid and crystals were mechanically separated. Elemental analysis by energy dispersive spectroscopy (EDS) showed the presence of indium and manganese, while no bismuth impurities were detected. The 1:1 metal ratio was confirmed by wavelength dispersive spectroscopy (WDS).

2. *Crystallographic studies*

Crystals of appropriate quality were chosen for structure solution by first analyzing a complete set of photographs obtained using a Charles Supper Co. precession camera with a crystal to film distance of 60 mm, and a precession angle of 10° mounted on an Enraf-Nonius 581 Diffractis X-ray generator operating at 800W using Mo Kα radiation (λ = 0.71069Å).

A crystal of $InMnO_3$ having the approximate dimensions of 0.100 x 0.100 x 0.020 mm was chosen for the single crystal structure determination. All measurements were made on an Enraf-Nonius CAD-4 diffractometer with graphite monochromated Mo Kα radiation (λ = 0.71069Å). Crystallographic data are summarized in Table 3.2.1.

Cell constants and an orientation matrix for data collection were obtained from a least-squares refinement using the setting angles of 25 centered reflections in the range of $18.0 < 2\Theta < 24.0°$. Based on the systematic absences of $hh2\overline{h}l$: $l \neq 2n$, packing considerations, a statistical analysis of intensity distribution and the successful solution and refinement of the structure, the space group was determined to be $P6_3/mmc$ (No. 194). A total of 778 reflections were collected. The intensities of three representative reflections, measured after every 60 minutes of X-ray exposure time, remained constant throughout data collection indicating crystal and electronic stability. Data were corrected for Lorentz, polarization, absorption,[23,24] and secondary extinction effects.

All calculations were performed on a MicroVAX 3500 with the use of TEXSAN crystallographic software.[25] The structure was solved by direct methods,[26] and refinement was performed using a full-matrix least-squares

TABLE 3.2.1

Summary of Crystallographic data for $InMnO_3$

Empirical Formula	$InMnO_3$
Formula weight	217.76
Crystal color, habit	black, hexagonal
Crystal dimensions (mm)	0.100 x 0.100 x 0.020
Crystal system	hexagonal
Space group	$P6_3/mmc$ (No. 194)
No. reflections used for unit cell	25 (18.0 - 24.0°)
Determination (2Θ range)	
Omega scan peak width at half height	0.32
Lattice parameters (Å)	
a	3.3885 (2)
c	11.4752 (1)
Volume ($Å^3$)	114.87 (1)
Z	2
D_{calc} (g/cm^3)	6.300
F_{000}	196
Diffractometer	Enraf-Nonius CAD-4
Radiation	Mo Kα (λ = 0.71069 Å)
μ (Mo Kα) (cm^{-1})	149.00
Temperature (° C)	23
Scan type	ω
$2\Theta_{max}$	59.8°
No. of Reflections Measured	778
No. Observations (I > 3.00 σ(I))	79
No. Variables	11
Corrections	Lorentz-polarization Absorption (trans. factors: 0.84 - 1.15) Secondary Extinction (coefficient: 0.18292E-04)
Residuals: R; R_W	0.033; 0.035
Goodness of fit Indicator	3.27
Max. Peak in Final Difference Map	1.36 e^-/ $Å^3$

calculation. The final values of the discrepancy factors were R = 0.033 ($R = \Sigma ||F_o| - |F_c|| / \Sigma |F_o| = 0.042$) and $R_w = 0.035$ ($R_w = \{(\Sigma w (|F_o| - |F_c|)^2 / \Sigma w F_o^2)\}^{1/2} = 0.052$), $w = 4F_o^2/s^2(F_o^2)$. The goodness of fit was 3.27 and the highest peak in the final difference map was 1.36 $e^-/Å^3$. The atomic scattering factors were those of Cromer and Waber and corrections for anomalous dispersion were from Cromer.[23,27]

3. Preparation of polycrystalline samples

Polycrystalline samples of $InMnO_3$ were prepared using a nitrate decomposition technique. Using a 10 mmol scale, a slight excess of $In(OH)_3$ (Johnson Matthey, 99.999%) was dissolved in 100 mL of concentrated HNO_3 with Mn(II) acetate tetrahydrate (Johnson Matthey, 99.999%) in a 400 mL beaker. Six mole-percent excess of indium hydroxide was necessary in order to ensure a single product of $InMnO_3$, to compensate for indium lost during the synthesis. If stoichiometric amounts of indium and manganese were used in the preparation of the precursor, the presence of manganese oxide was seen by powder X-ray diffraction.

A beaker of the nitric acid solution was heated on a hotplate at low heat with stirring until the solution became colorless. The temperature of the hotplate was then increased to allow slow evaporation of the liquid. When less than 10 mL of liquid remained, the beaker was removed from the hotplate allowing the remaining liquid to solidify into a clear paste. The beaker was then placed into a box furnace and heated to 550°C for 12 hours during which time the clear precursor turned into a low-density, black solid. The black solid was ground in an agate mortar and sealed in an evacuated quartz tube. The quartz tube was heated to 1000°C for 48 hours resulting in an extremely

crystalline, black product that consisted of small, hexagon-shaped, single crystallites visible under a microscope. It should be noted that the quartz tubes contained excess pressure that was noticeable as an explosive popping when the tube was opened. Polycrystalline samples were structurally characterized by powder X-ray diffraction on a Rigaku RU300 rotating anode diffractometer operating at 10kW with Cu Kα radiation (λ = 1.54184Å).

4. *Magnetic measurements*

Magnetic data were collected on finely ground polycrystalline samples using a Quantum Design MPMS SQUID magnetometer at temperatures ranging from 5 to 300K and applied fields ranging from 0.1 to 40kG. A scan length of 6 cm was used and 20 measurements were performed over the scan length. A total of 3 scans were averaged for each data point. All data were corrected for the diamagnetic contribution on a Kel-F sample holder. Core diamagnetism corrections for the substituent elements were not applied. All samples were zero-field cooled and measured by heating unless otherwise noted.

5. *Neutron diffraction*

Neutron diffraction patterns were collected for $InMnO_3$ at temperatures ranging from 5 to 200K using a constant wavelength source (λ = 2.5040Å) at the AECL Chalk River neutron diffraction facility. The resulting patterns were analyzed for both structural and magnetic reflections at temperatures above and below the magnetic transition temperature. Data were collected by a multi-detector array consisting of 800 detectors over the range of $20 < 2\Theta < 100°$, at a resolution of 0.1° 2Θ.

B. Results

1. Structural

Final atomic positions and anisotropic U values from the single crystal structure solution are listed and Table 3.2.2 and Table 3.2.3, respectively. Selected bond distances and bond angles are listed in Table 3.2.4.

The structure of $InMnO_3$, as determined by single crystal diffraction, Figure 3.2.1, consists of alternating layers of octahedrally coordinated indium and trigonal bipyramidally coordinated manganese. The manganese and indium coordinations are fixed by symmetry (Table 3.2.2) and, consequently, have ideal D_{3h} and near ideal octahedral symmetry, respectively. The structure of $InMnO_3$ may be described as a stuffed delafossite structure[28] in which an extra oxygen, O(2) has been inserted into the manganese plane in Wyckoff position 2b, ($\bar{6}$m2 symmetry). Consequently, instead of the linear coordination of **B** found in the ABO_2 delafossite structure, manganese is trigonal bipyramidally coordinated. Alternatively, the $InMnO_3$ structure may be described in terms of the CdI_2 structure,[1] in which the empty octahedral sites located between the layer of occupied sites has been filled by a Mn-O hexagonal net (6,3).[29] The trigonal bipyramidally coordinated manganese layers repeat with every second layer. The staggered arrangement of the manganese atoms results in a unit cell which contains two layers of indium-oxygen octahedra and two layers of manganese-oxygen trigonal bipyramids before repeating. The indium atoms have two O(2) atoms above and below the plane of InO_6 at a distance of 2.87Å, a nonbonding distance for indium. The manganese-oxygen bonds in the trigonal bipyramids are smaller in the **z**-direction than in the **xy**-plane with an apical bond distance of 1.87Å *vs.* an in-plane distance of 1.96Å.

TABLE 3.2.2

Positional and Isotropic Equivalent Thermal Parameters for $InMnO_3$

Atom	Wyckoff position	x	y	z	B(eq)
In	2a	0	0	0	1.97(5)
Mn	2d	2/3	1/3	1/4	1.05(6)
O(1)	4f	2/3	1/3	0.0871(7)	2.0(2)
O(2)	2b	0	0	1/4	1.5(4)

TABLE 3.2.3

u_{ij} or U values for $InMnO_3$ in $Å^2$

Atom	u_{11} (U)	u_{22}	u_{33}	u_{12}
In	0.013(1)	0.013	0.036(1)	0.007
Mn	0.012(1)	0.012	0.001(1)	0.006
O(1)	0.023(3)	0.23	0.002(4)	0.012
O(2)	0.10(3)	0.10	0.04(2)	0.05

$U_{13}=U_{23}=0$ by symmetry

TABLE 3.2.4

Selected interatomic bond distances and angles for $InMnO_3$

Atom	Atom	distance(Å)	Atom	Atom	Atom	angle(°)
In	O(1)	2.202(3)	O(1)	In	O(1)	101.0(2)
In	O(2)	2.869	O(1)	In	O(1)	79.0(2)
In	In	3.3985(2)	O(1)	In	O(1)	180
In	Mn	3.4756(1)	O(1)	Mn	O(2)	90
Mn	O(1)	1.870(8)	O(2)	Mn	O(2)	120
Mn	O(2)	1.9621(1)				
Mn	Mn	3.3985(2)				

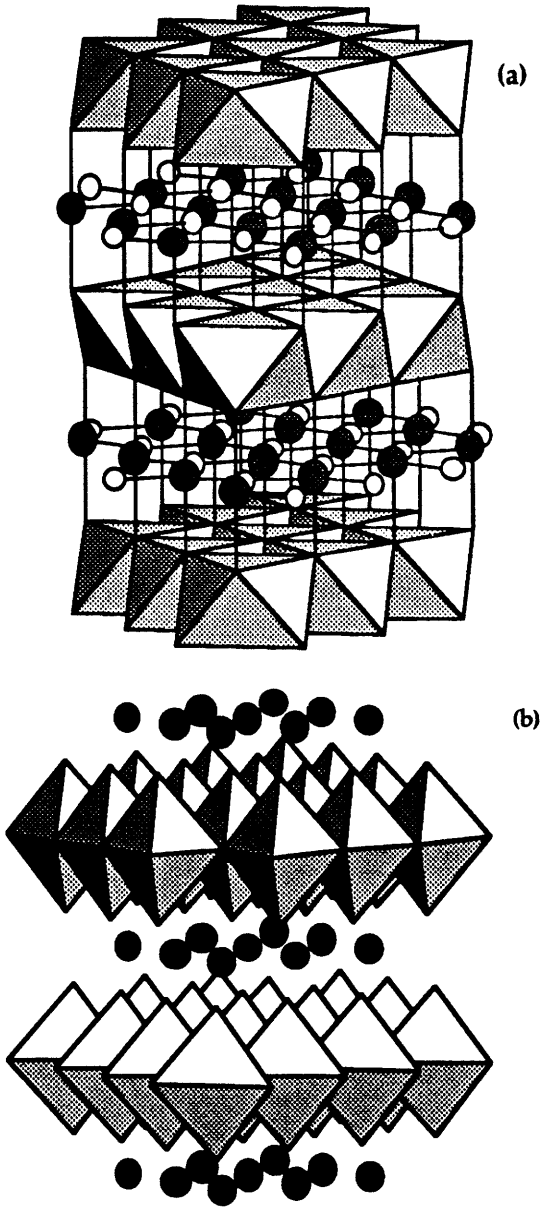

Figure 3.2.1 The $P6_3/mmc$ structure of $InMnO_3$ as determined by single crystal X-ray diffraction. (a) A polyhedral representation of the octahedral coordination of indium. Manganese atoms are represented as filled circles; oxygen atoms are located at the apices of the octahedra and are represented as open circles in the manganese-oxygen plane; (b) A polyhedral representation of the trigonal bipyramidal polyhedra. Manganese is located at the center of the polyhedra; oxygen is located at the apices of polyhedra; indium atoms are represented as filled circles.

The structure of $InMnO_3$ as determined by powder neutron diffraction is slightly different than the structure obtained by single crystal X-ray diffraction. The polycrystalline sample of $InMnO_3$ is isostructural with $YMnO_3$.[30] This related structure (Figure 3.2.2) is a distorted version of the $P6_3/mmc$ structure of $InMnO_3$. Structural determination parameters are listed in Table 3.2.5. The **a**-parameter of the $P6_3cm$ $InMnO_3$ is equal to $\sqrt{3}\mathbf{a}(P6_3/mmc)$ while the **c**-parameter is the same in both compounds. The indium is located in distorted seven-fold coordination. The manganese is located in distorted trigonal bipyramidal coordination (C_s symmetry). Each trigonal bipyramid is canted with respect the **c**-axis.

2. *Magnetism*

a) Magnetic susceptibility

Magnetic measurements, as determined from susceptibility *vs.* temperature plots collected on a SQUID magnetometer, show that $InMnO_3$ orders in an antiferromagnetic-like fashion, $T_N \cong 15K$. The susceptibility *vs.* temperature plot displays a broad maximum at approximately 15K with an applied field of 0.5kG.(Figures 3.2.3 and 3.2.4a) Changes in the inflection of the susceptibility curve are apparent at approximately 40K and 120K. The behavior of $InMnO_3$, however, also displays a complex field dependence.(Figures 3.2.4a-d) Unlike the spin-glass behavior of $Bi_2Fe_{4-x}M_xO_9$ described in Chapter 2, $InMnO_3$ displays behavior reminiscent of a spin-flop, a magnetic system in which antiferromagnetic ordering may be gradually changed to ferromagnetic ordering in the presence of an applied field.[31] The application of an increasing external magnetic field causes the susceptibility below the

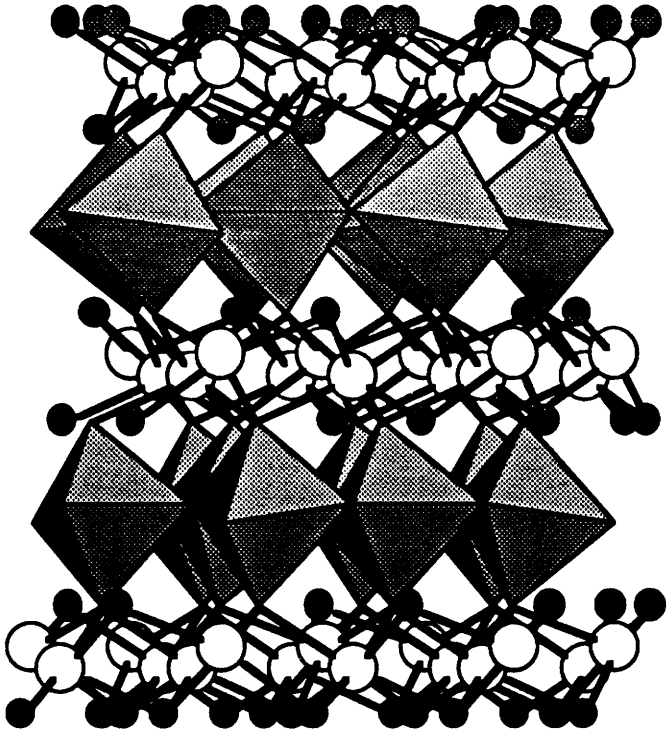

Figure 3.2.2 The $P6_3cm$ structure of $InMnO_3$ as determined by polycrystalline neutron diffraction. Indium is represented as large open circles, manganese is located at the center of the distorted polyhedra, oxygen is represented both as small filled circles and located at the apices of all polyhedra.

TABLE 3.2.5
Structural determination parameters for $InMnO_3$
as determined by powder neutron diffraction

Space group	$P6_3cm$
Lattice parameters (Å)	
a	5.8871(3)
c	11.5015(7)
Volume ($Å^3$)	345.21
Z	6
Diffractometer	Constant wavelength neutron diffractometer
Radiation (Å)	2.5040
Temperature (K)	200
2Θ range	$20 \leq 2\Theta \leq 100°$
Residuals	
R_{wp}	0.084
R_I	0.044
R_E	0.033

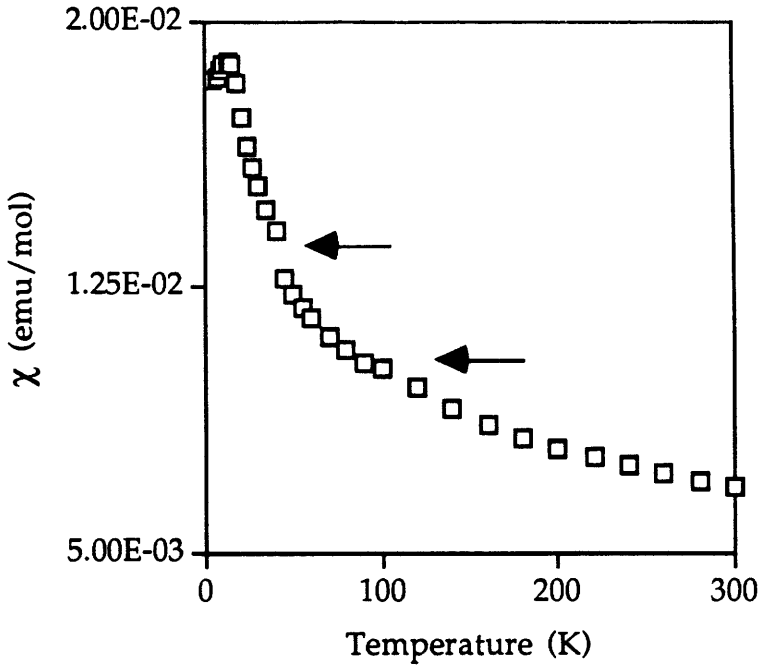

Figure 3.2.3 Magnetic susceptibility *vs.* temperature for $InMnO_3$ at 0.5kG. A transition temperature is present at 15K. Note inflections in the susceptibility curve at 40K and 120K.

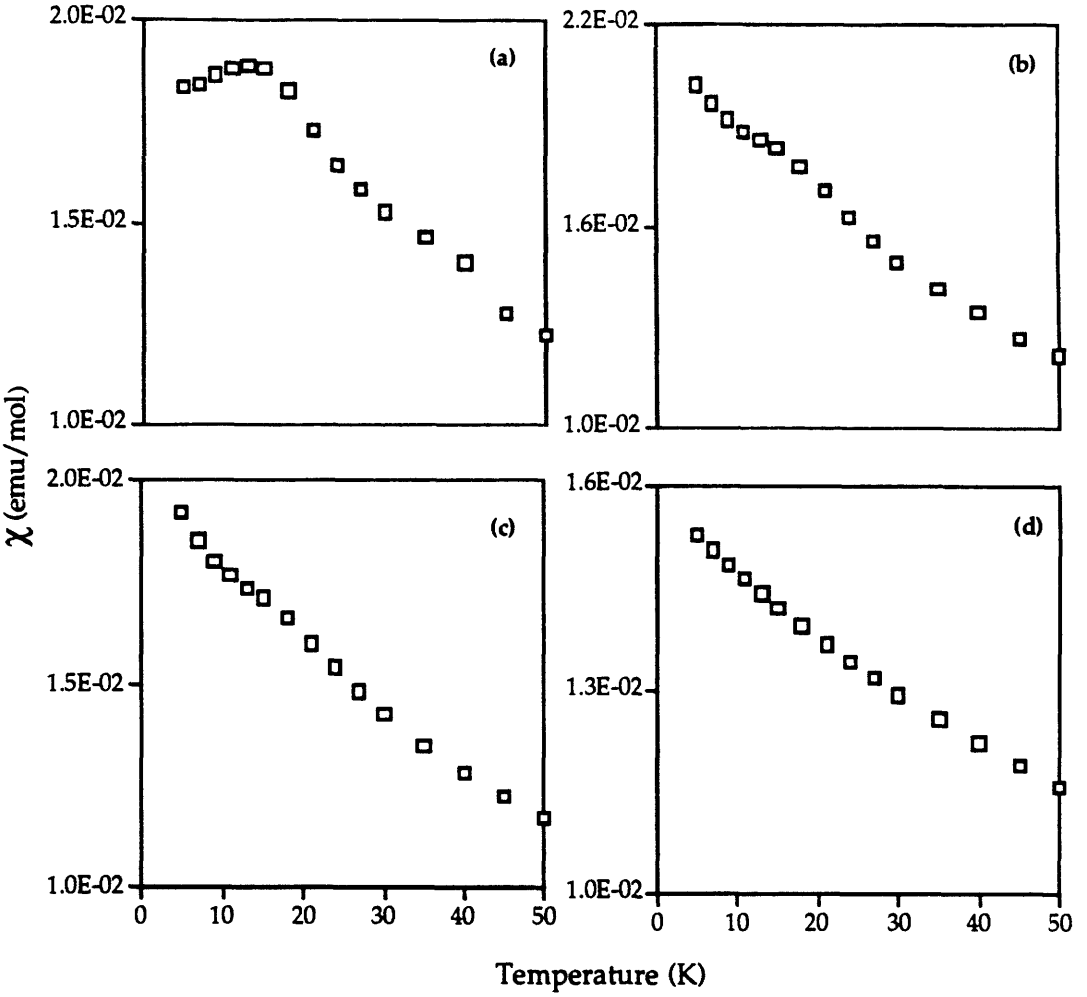

Figure 3.2.4 Magnetic susceptibility *vs.* temperature for $InMnO_3$ at several magnetic fields: (a) 0.5kG; (b) 2.5kG; (c) 5kG; (d) 40kG.

transition temperature to increase with decreasing temperature until the susceptibility plot appears featureless. Although $InMnO_3$ appears to be an antiferromagnet at 0.5kG, Figure 3.2.4a, this behavior gradually changes as a function of applied field.(Figures 3.2.4b-c) As the external field is raised to 40kG, Figure 3.2.4d, all evidence of a magnetic transition at 15K disappears.

b) Neutron diffraction

The magnetic behavior observed by polycrystalline neutron diffraction is indicative of complex magnetic structure. The magnetic unit cell, like the polycrystalline chemical unit cell, has the space group $P6_3cm$, however, the c-parameter of the magnetic unit cell is doubled in respect to the chemical unit cell: **a** = 5.908Å; **c** = 2c(chemical cell)= 22.988Å at 5K. A powder neutron diffraction pattern of $InMnO_3$ at 5K is shown in Figure 3.2.5 and indexed according to the values shown in Table 3.2.6. All magnetic peaks are significantly broader than the resolution-limited value, indicative of short-range magnetic correlations, not long-range order. Unlike the susceptibility *vs.* temperature data, magnetic order according to the neutron diffraction experiment is present until approximately 120K for all magnetic peaks with the exception of the (1 0 0) peak which maintains some intensity above 120K. Intensity *vs.* temperature plots for the (1 0 0) peak and a characteristic peak, (1 0 $^1/_2$), indicative of a transition temperature at 120K are shown in Figure 3.2.6. Magnetic peaks are indexed with respect to the chemical unit cell for consistency, thus non-integral Miller indices are possible for magnetic reflections. The intensity *vs.* temperature behavior for the (h 0 $^n/_2$) family of peaks displays an unusual decrease at low temperatures before increasing to a maximum at approximately 90K. The initial decrease in intensity

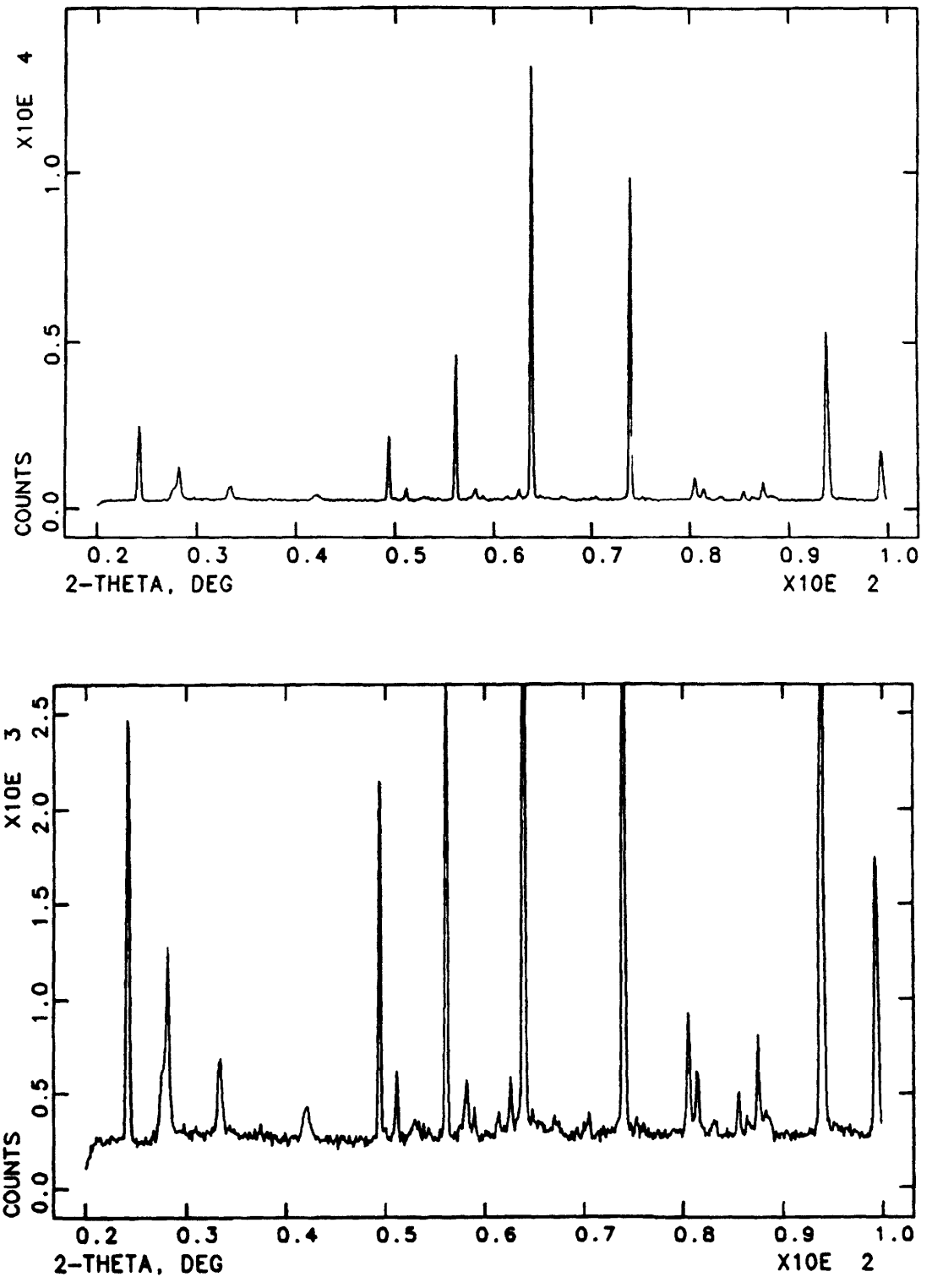

Figure 3.2.5 Powder neutron diffraction pattern of $InMnO_3$ at 5K. The scale of the lower plot is expanded to show low intensity magnetic reflections more clearly. Peak positions for structural and magnetic reflections are listed in Table 3.2.6.

TABLE 3.2.6
Crystallographic and magnetic peak positions for the $P6_3cm$ structure of $InMnO_3$

2Θ(°)	hkl	$FWHM_{(obs)}$(°)	$FWHM_{(res.\ limit)}$(°)
25.22	002		
28.78	100	0.96(3)	0.27
29.04	$10^1/_2$	0.28(2)	0.28
34.04	$10^3/_2$	0.54(2)	0.27
38.41	102		
42.90	$10^5/_2$	0.72(8)	0.23
50.45	110		
51.77	004		
52.20	111		
53.80	$10^7/_2$	0.71(12)	0.23
57.21	112		
58.95	200		
59.06	$20^1/_2$	0.33(1)	0.22
60.15	104		
62.20	$20^3/_2$	0.29(5)	0.24
65.01	113		
66.14	005		
72.46	203		
75.19	114		
81.81	006		
82.27	204		
83.92	$21^3/_2$	0.54	0.31
86.72	212		
87.64	115		
88.78	106		
95.14	300		
100.66	302		

* Magnetic peaks are indexed according to the chemical unit cell. Peak width data is included for magnetic reflections only in order to distinguish between structural and magnetic reflections.

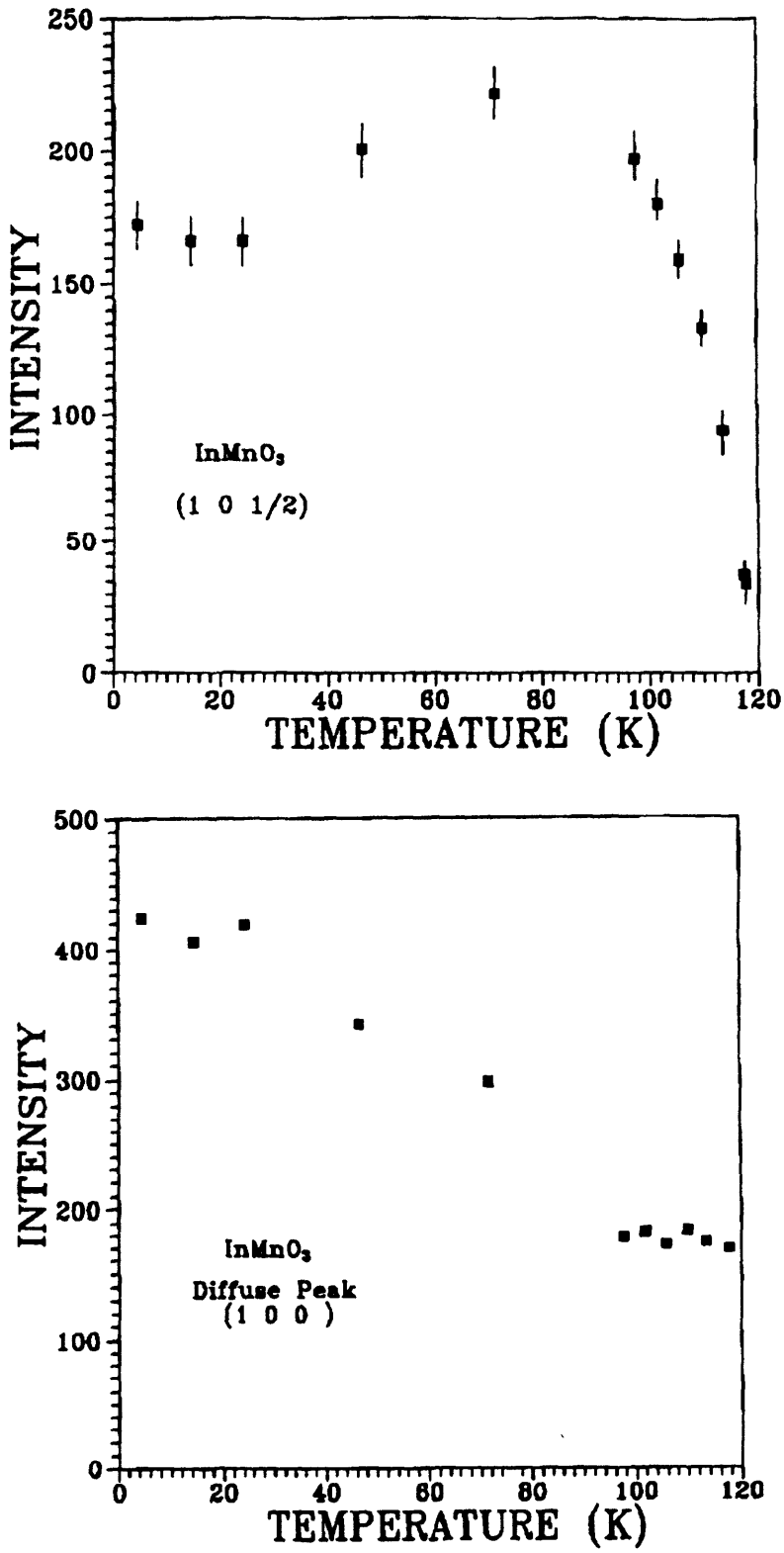

Figure 3.2.6 Intensity *vs.* temperature behavior for the magnetic neutron diffraction reflections (a) (1 0 1/2); and (b) (1 0 0).

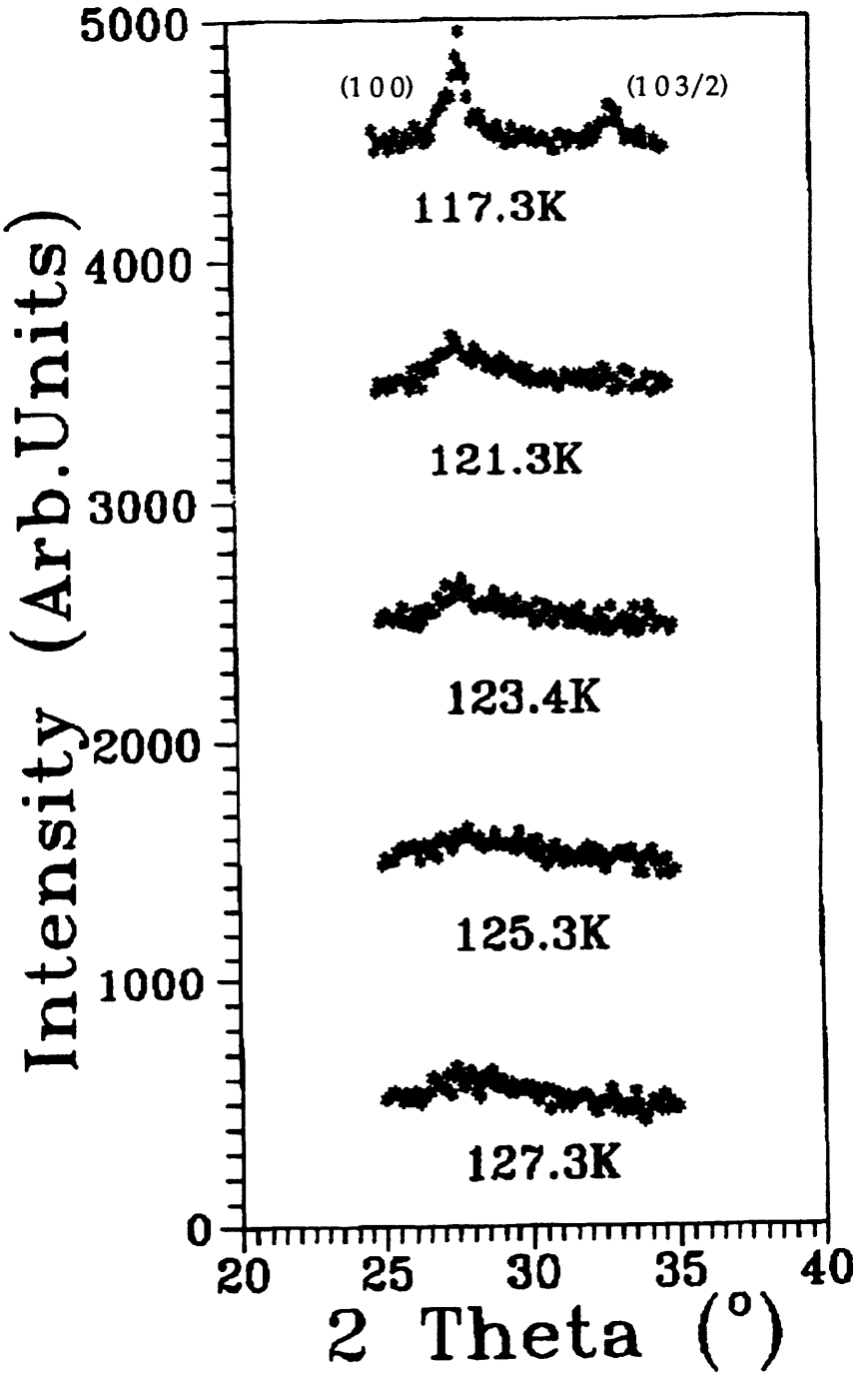

Figure 3.2.7 Intensity *vs.* temperature behavior for the diffuse magnetic reflection (1 0 0). Note that unlike the other magnetic reflections, intensity of the (1 0 0) remains past 120K.(See Figure 3.2.6) The (1 0 $^{3}/_{2}$) reflection, present at 38.4° 2Θ, disappears between 117.3K and 121.3K.

corresponds to the change in inflection in the temperature *vs.* susceptibility plot at 40K. The temperature dependence of the (1 0 0) peak is shown in Figure 3.2.7. The intensity *vs.* temperature behavior of the (1 0 0) peak is unlike behavior of the (h 0 n/2) family of peaks.(Figure 3.2.6) The intensity of the (1 0 0) peak decreases steadily with increasing temperature and stabilizes at approximately 100K, maintaining intensity after the other magnetic reflections have disappeared.(Figure 3.2.6)

C. Discussion

$InMnO_3$ is a low temperature structure and decomposes above 1050°C. The spinel solid solution, $In_{2-x}Mn_{1+x}O_4$,[32] is the stable In-Mn-O structure above 1000°C and forms preferentially if a mixture of In_2O_3 and Mn_2O_3 is ground together and heated in air. Polycrystalline $InMnO_3$ can be prepared, as noted above, *via* a nitrate decomposition route, although care must be taken not to exceed 1050°C, at which point $InMnO_3$ powder decomposes into In_2O_3, Mn_2O_3 and $In_{2-x}Mn_xO_3$.

The structure of $P6_3/mmc$ $InMnO_3$ and $P6_3/mmc$ $(RE)AlO_3$ (RE = Y, Eu, Gd, Tb, Dy, Ho, Er)[3,33] are similar, differing only in the coordination of the indium/yttrium site. In the case of $YAlO_3$, the yttrium is bound by six oxygen atoms at a distance of 2.274Å, and two additional oxygens, at a distance of 2.63Å. The higher coordination of the yttrium site pulls the Al - O layers closer together above and below the plane of the yttrium-oxygen octahedra so that **c** = 10.52Å. In the case of $InMnO_3$, indium has virtually no interaction whatsoever with O(2). The indium-O(2) distance is 2.869Å, longer than the combined van der Waals radii of indium and oxygen. The indium-O(2) distance is more than 0.2Å longer than the yttrium-O(2) distance in $YAlO_3$,

although the ionic radius of indium is 0.1Å less than the ionic radius of yttrium in octahedral coordination. Consequently the c-axis in $InMnO_3$, c = 11.47Å, is almost 1Å longer than the c-axis in $YAlO_3$. The structure of $InMnO_3$ is unique when compared to the $YAlO_3$ structure since the higher coordination of the rare earth site shortens of the c-axis by forming a strong Y-O(2) bond. This difference is seen in the chemical reactivity of rare earth aluminates which transform to the perovskite structure above 1000° C, while $InMnO_3$ decomposes into its constituent binary oxides. The strong yttrium-O(2) bonds effectively hold the basic structure together while the material undergoes a structural phase transition.

The polycrystalline sample of $InMnO_3$ ($P6_3cm$) is isostructural with $YMnO_3$.[30,34] The $P6_3cm$ structure is a distorted version of the $P6_3/mmc$ structure and may be more stable thermodynamically. It has been reported that $YMnO_3$ undergoes a phase change at 1010°C to a hexagonal phase which was reported to be isostructural to the $P6_3/mmc$ structure, although the structure was never solved.[34] $YMnO_3$, like $YAlO_3$, transforms into the perovskite structure at higher temperatures. $YMnO_3$ gains stability from the strong interactions between the A cation and the oxygen framework which may enable the structure to undergo a phase transition without decomposition. The short RE-O(2) interaction may be responsible for the relative stability of $YMnO_3$ and $YAlO_3$ when compared to $InMnO_3$. The structure of $YMnO_3$ and the other $(RE)MnO_3$ compounds is similar to $YAlO_3$ in this sense. The c-axes in these materials are disproportionately smaller compared to expectations based on the ionic radii of the rare earth ions *vs.* indium. The c-axis of $HoMnO_3$ is shorter than that of $InMnO_3$, 11.42Å *vs.*

c = 11.50Å, even though the ionic radius of holmium is more than 10% larger than the ionic radius of indium.

The staggered arrangement of the manganese atoms in $InMnO_3$ should result in only limited communication between the transition metal oxide planes. It has been shown that transition metal structures with low dimensional units have the potential for interesting magnetic and electronic effects.[31,35-39] The low dimensional $InMnO_3$ structure, thus, should give rise to strong intra-layer(2D) manganese-manganese interactions, while oxygen-mediated inter-layer(3D) interactions are not expected to be significant except at very low temperatures. The hexagonal manganese-oxygen plane in $InMnO_3$ may also cause frustration in magnetic ordering due to the competing interactions which will occur when three metal atoms attempt to couple antiferromagnetically in a hexagonal metal-oxygen lattice. The broad transitions in the magnetic susceptibility *vs.* temperature plots may be due to low dimensional behavior and the field dependence of the susceptibility data may be due to competing interactions within the hexagonal metal-oxygen framework.

Magnetic ordering in this structure type may be described according to the following models: **(1)** the spins are aligned perpendicular to the **ab**-plane, **(2)** the spins are aligned parallel to the **ab**-plane, or **(3)** the spins are canted out of the **ab**-plane. If the spins are aligned perpendicular to the **ab**-plane, ferromagnetic ordering is possible. (Figure 3.2.8a) However, as seen in Figures 3.2.8b-c, any antiferromagnetic orientation of the spins perpendicular to the plane will result in uncompensated moments and a frustrated antiferromagnetic ordering. Antiferromagnetic ordering is also possible if

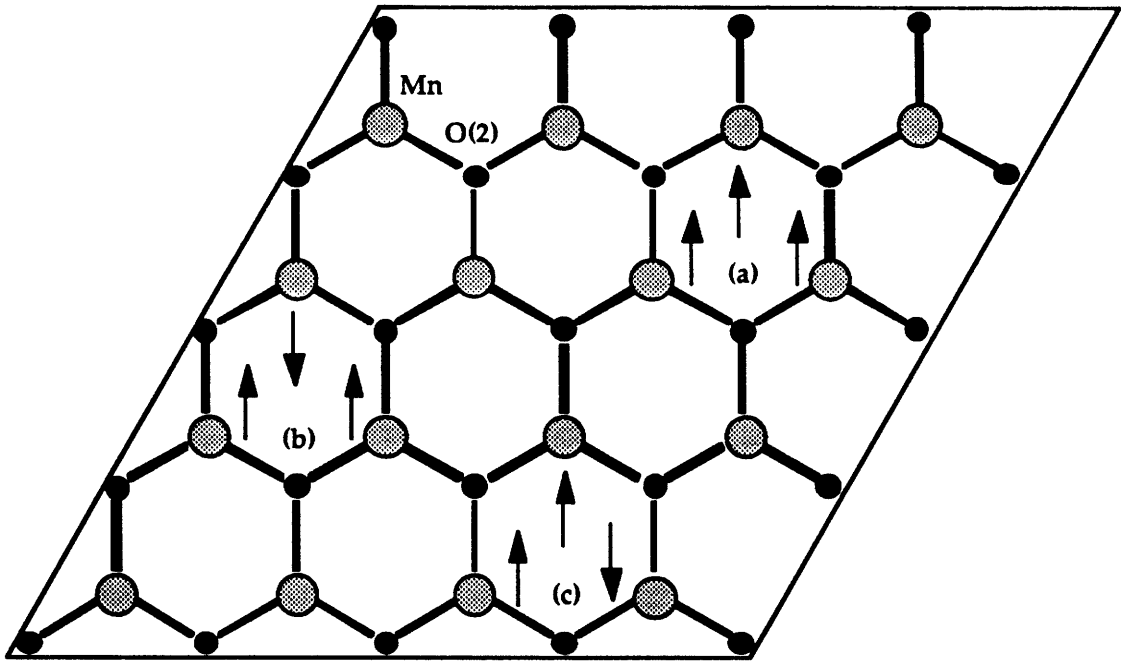

Figure 3.2.8 A perfect hexagonal metal-oxygen lattice with spins parallel to the c-axis. (a) Oxygen-mediated ferromagnetic ordering between three metal ions in an hexagonal net; (b) and (c) Oxygen-mediated antiferromagnetic ordering between three metals in an hexagonal net is not possible within a single plane without frustration.

(1) the spins are aligned parallel to the plane and 120° apart or **(2)** the spins are ferromagnetically ordered within the plane and each plane is arranged in an antiferromagnetic fashion. A more sensitive magnetic probe such as neutron diffraction will allow a more conclusive interpretation.

Although the crystallographic unit cell of $P6_3cm$ $InMnO_3$ is isostructural with $YMnO_3$, the magnetic behavior displayed by $P6_3cm$ $InMnO_3$ is unique. Unlike $YMnO_3$, the magnetic unit cell of $P6_3cm$ $InMnO_3$ cannot be indexed on the chemical unit cell of **a** = 5.8871Å, **c** = 11.5015Å. Instead, the magnetic **c**-axis must be doubled relative to the chemical **c**-axis. In the case of $YMnO_3$, the spins are arranged in a triangular fashion, perpendicular to the hexagonal plane in an orientation such that the spins within the **z** = 0 plane are opposed by the spins in the **z** = $^1/_2$ plane. In this way, the magnetic cell repeats with each chemical unit cell resulting in long range order.[40] Two features of the $P6_3cm$ $InMnO_3$ magnetic structure are in contrast with $YMnO_3$. The magnetic unit cell of $P6_3cm$ $InMnO_3$ requires a doubling of the **c**-axis, **c** = 22.988Å, including four manganese-oxygen planes. The magnetic peaks in $P6_3cm$ $InMnO_3$ are all significantly more broad than the resolution-limited value of the diffractometer, implying short range correlations only, and unlike $YMnO_3$, no true long range order. Since the magnetic spins cannot be perpendicular to the hexagonal plane and since the neutron diffraction data implies only short range order, it is believed that the spins may be canted *vs.* the **c**-axis. One possible canting arrangement is a spin helix in which the throw of the helix repeats every 2 chemical unit cells (23Å) in the **c**-direction. The spins of the helical magnetic structure may be fluxional with respect to temperature. If the spins were not firmly fixed in one direction, the observed field dependent behavior could be a result of a spin rearrangement which

produces more stable spin orientations as the external magnetic field is increased.

The fluxional spin model is supported by the fact that long range magnetic ordering is not visible in the magnetic susceptibility plots until approximately 15K. Since the time scale of magnetic susceptibility is on the order of 1 second while the time scale of neutron diffraction is on the order of 10^{-8} seconds, the magnetic correlations appearing in the neutron diffraction data at 120K may be unresolvable by magnetic susceptibility. The susceptibility discontinuity at 120K corresponds with the onset of magnetic ordering seen by neutron diffraction. The discontinuity at 40K corresponds with variations the intensity *vs.* temperature plots in the neutron pattern.(Figure 3.2.6) Fluctuations involving a rearrangement of spins within an ordered magnetic system would cause unusual intensity *vs.* temperature behavior. Furthermore, the peak shape and intensity *vs.* temperature behavior of the (1 0 0) neutron diffraction peak is characteristic of low dimensional magnetic ordering[41] which maintains intensity to approximately 127K. Thus, the complex overall behavior of the magnetic structure of $InMnO_3$ may be due to the combination of long-range but low dimensional magnetic structure described by the (h 0 0) magnetic diffraction peaks and short range, three-dimensional magnetic structure described by the (h 0 $^{n}/_{2}$) magnetic diffraction peaks.

D. Conclusions

A new main group - transition metal oxide, $InMnO_3$, is reported to have two polymorphs and complex magnetic behavior. The presence of both a centrosymmetric phase ($P6_3/mmc$) and a noncentrosymmetric phase ($P6_3cm$)

has been determined by single crystal X-ray diffraction and polycrystalline neutron diffraction, respectively. Antiferromagnetic behavior, T_N = 15K, was observed by magnetic susceptibility methods but according to neutron diffraction, the magnetic structure was observed to persist above 120K or higher. The difference in the temperature of onset for magnetic ordering is believed due to rapid fluctuations in the spin orientation at temperatures between 120K and 15K such that no magnetic ordering may be observed by magnetic susceptibility. A combination of both three-dimensional short-range magnetic correlations characterized by the (h 0 $^{n}/_{2}$) family of magnetic reflections, and low dimensional long-range ordering characterized by the (h 0 0) reflection peaks is believed responsible for this complex magnetic behavior.

Section 3.3: $InFeO_3$

A. Experimental

1. Preparation of single crystals

Single crystals of $InFeO_3$ were prepared from In_2O_3 (Cerac, 99.99%) and Fe_2O_3 (Cerac 99.99%) in a Bi_2O_3 (Cerac 99.9%) flux. Approximately 3 mmol of the binary oxides were ground together and pelletized. The flux to reactants ratio was 1:1:1. The pellet was heated at 950°C in air on platinum foil to prevent aluminum contamination by the Al_2O_3 crucible. After three days the pellet was quenched to room temperature. Partial melting occurred during the heating cycle resulting in the formation of dark brown hexagonal plates of $InFeO_3$. The flux matrix was weakened with concentrated nitric acid and crystals were separated mechanically. Elemental analysis by EDS showed the

presence of indium and iron, but no bismuth was detected. The metal stoichiometry was confirmed by WDS to be 1:1.

Many attempts were made to prepare polycrystalline $InFeO_3$, however none were successful. The decomposition of hydroxide precursors described in the literature[4,5] could not be reproduced. Other synthetic approaches included the nitrate precursor technique described in Section 3.2 and the use of FeO as an iron source. Temperature and time variations during the both decomposition step and the sintering step were attempted without success.

2. *Crystallographic studies*

Crystals of appropriate quality were chosen for structure solution by first analyzing a complete set of photographs obtained using a Charles Supper Co. precession camera with a crystal to film distance of 60 mm, and a precession angle of 10° mounted on an Enraf-Nonius 581 Diffractis X-ray generator operating at 800W with Mo Kα radiation (λ = 0.71069Å). Photographs of $InFeO_3$ were compared to photos of isostructural $InMnO_3$.

A crystal of $InFeO_3$ having the approximate dimensions of 0.080 x 0.080 x 0.040 mm was chosen for the single crystal structure determination. All measurements were made on an Enraf-Nonius CAD-4 diffractometer with graphite monochromated Mo Kα radiation (λ = 0.71069Å). Crystallographic data are summarized in Table 3.3.1.

Cell constants and an orientation matrix for data collection were obtained from a least-squares refinement using the setting angles of 25 centered reflections in the range of $18.0 < 2\Theta < 24.0°$. Based on the systematic absences of $hh2\bar{h}l$: $l \neq 2n$, packing considerations, a statistical analysis of intensity

TABLE 3.3.1

Summary of Crystallographic data for $InFeO_3$

Empirical Formula	$InFeO_3$
Formula weight	218.67
Crystal color, habit	brown, hexagonal
Crystal dimensions (mm)	0.080 x 0.080 x 0.040
Crystal system	hexagonal
Space group	$P6_3/mmc$ (No. 194)
No. reflections used for unit cell Determination (2Θ range)	25 (18.0 - 24.0°)
Omega scan peak width at half height	0.33
Lattice parameters (Å)	
a	3.3270 (2)
c	12.1750 (1)
Volume ($Å^3$)	116.76 (2)
Z	2
D_{calc} (g/cm^3)	6.219
F_{000}	198
Diffractometer	Enraf-Nonius CAD-4
Radiation	Mo Kα (λ = 0.71069 Å)
μ (Mo Kα) (cm^{-1})	156.63
Temperature (° C)	23
Scan type	ω
$2\Theta_{max}$	59.6°
No. of Reflections Measured	1027
No. Observations (I > 3.00 σ(I))	85
No. Variables	11
Corrections	Lorentz-polarization Absorption (trans. factors: 0.89 - 1.10) Secondary Extinction (coefficient: 0.25452E-04)
Residuals: R; R_W	0.014; 0.021
Goodness of fit Indicator	1.28
Maximum peak in Final Diff. Map	0.54 e^-/ $Å^3$

distribution and the successful solution and refinement of the structure, the space group was determined to be $P6_3/mmc$ (No. 194), the same space group reported for $InMnO_3$ in Section 3.2. A total of 1027 reflections were collected of which 113 were unique. The intensities of three representative reflections, measured after every 60 minutes of X-ray exposure time, remained constant throughout data collection indicating crystal and electronic stability. Data were corrected for Lorentz, polarization, absorption,[23,24] and secondary extinction effects.

All calculations were performed on a MicroVAX 3500 with the use of TEXSAN crystallographic software.[25] The structure was solved by direct methods,[26] and refinement was performed using a full-matrix least-squares calculation. The final values of the discrepancy factors were R = 1.4% ($R = \Sigma \, | \, |F_o| - |F_c| \, | \, / \, \Sigma \, |F_o| = 0.014$) and R_w = 2.1% ($R_w = \{(\Sigma \, w \, (|F_o| - |F_c|)^2 \, / \, \Sigma \, w \, F_o^2)\}^{1/2} = 0.021$), $w = 4F_o^2/s^2(F_o^2)$. The goodness of fit was 1.28 and the highest peak in the final difference map was 0.54 $e^-/Å^3$. The atomic scattering factors were those of Cromer and Waber and corrections for anomalous dispersion were from Cromer.[23,27]

B. Results

1. Structural

The structure of $InFeO_3$ is isostructural with that of $InMnO_3$, described in Section 3.2.(Figure 3.2.1) Positional and isotropic thermal parameters for $InFeO_3$ are listed in Table 3.3.2. Anisotropic U values are listed in Table 3.3.3. Bond distances and angles are listed in Table 3.3.4.

TABLE 3.3.2

Positional and Isotropic Equivalent Thermal Parameters for $InFeO_3$

Atom	Wyckoff position	x	y	z	$B_{(eq)}$
In	2a	0	0	0	0.48(2)
Fe	2d	2/3	1/3	1/4	0.32(3)
O(1)	4f	2/3	1/3	0.0850(3)	0.55(8)
O(2)	2b	0	0	1/4	0.7(1)

TABLE 3.3.3

u_{ij} or U values x 100 for $InFeO_3$ in $Å^2$

Atom	u_{11} (U)	u_{22}	u_{33}	u_{12}
In	0.59(3)	0.59	0.65(4)	0.30
Fe	0.50(4)	0.50	0.21(5)	0.25
O(1)	0.7(2)	0.7	1.0(3)	0.4
O(2)	0.9(1)	0.9	0.3(2)	0.4

$U_{13}=U_{23}=0$ by symmetry

TABLE 3.3.4

Selected interatomic bond distances and angles for $InFeO_3$

Atom	Atom	distance(Å)	Atom	Atom	Atom	angle(°)
In	O(1)	2.182(2)	O(1)	In	O(1)	99.3(1)
In	O(2)	3.044	O(1)	In	O(1)	80.7(1)
In	In	3.3270(2)	O(1)	In	O(1)	180
In	Fe	3.5992(1)	O(1)	Fe	O(2)	90
Fe	O(1)	2.008(4)	O(2)	Fe	O(2)	120
Fe	O(2)	1.9208(1)				
Fe	Fe	3.3270(2)				

The structure may be described as consisting of alternating layers of octahedra and trigonal bipyramids.(Figure 3.2.1) The indium atoms are situated within octahedral interstices of closest-packed O(1) layers. All the octahedral interstices are filled. The O(1) layers are separated by an Fe-O(2) (6,3) hexagonal net.[29] Iron is coordinated in a trigonal bipyramidal fashion. The Fe-O(2) layers are staggered such that they repeat with every other layer. The iron coordination polyhedron has ideal D_{3h} symmetry, as found in the isostructural $InMnO_3$ (Section 3.2).[42]

C. Discussion

The structure of $InFeO_3$ is isostructural with that of $InMnO_3$, described in Section 3.2. Unlike $InMnO_3$, however, the presence of $InFeO_3$ has been reported previously,[4,5] as part of a multi-phase polycrystalline sample. The apical bond in the trigonal bipyramids of $InFeO_3$ is elongated compared to that found in $InMnO_3$; the **c**-axis is also significantly longer although the ionic radii of Mn^{3+} and Fe^{3+} are identical according to Shannon.[43] This elongation of the apical bond, and consequently the **c**-axis, is consistent with the presence of an electron in the d_z^2 orbital for high spin Fe^{3+} (d^5) unlike high spin Mn^{3+} (d^4). Consequently, the difference in **c**-axis lengths between the manganese and iron compounds can be explained by an elongation and weakening of the axial Fe-O bond which effects a lowering in the energy level of the d_z^2 orbital. This results in a Fe-O(1) distance that is 0.14 Å longer than the corresponding Mn-O(1) distance. The in-plane trigonal Fe-O(2) distance is shorter than the apical Fe-O(1) distance in $InFeO_3$, while for $InMnO_3$ the opposite is true. The weakening of the apical Fe-O trigonal bipyramidal bond may cause relative structure instability in comparison to the corundum and bixbyite structures.

This relative instability may be one reason why preparation of single-phase polycrystalline samples is so difficult.

The difference between both $InMnO_3$ and $InFeO_3$, and the related $YAlO_3$[3,33] is even more dramatic. The **a**-axis of $YAlO_3$ is larger than that of either $InFeO_3$ or $InMnO_3$, 3.678Å *vs.* 3.327Å and 3.398Å, respectively, while the **c**-axis is dramatically shorter, 10.52Å *vs.* 12.175Å and 11.48Å, respectively. The Al-O bond lengths in $YAlO_3$, however, are surprisingly similar to the Fe-O bond lengths found in $InFeO_3$ even though the **c**-axis is almost 2 Å shorter. The in-plane trigonal Al-O distances are 2.12 Å, while the apical Al-O distances are 1.82 Å. The contraction of the **c**-axis in $YAlO_3$ is related to the coordination of the rare earth atom. The coordination of yttrium is increases from 6-fold to 8-fold coordination through the **z**-axis contraction which enables the yttrium to bond with two additional next-nearest neighbor O(1) atoms. Indium is commonly found in octahedral coordination, consequently, in $InMnO_3$ and $InFeO_3$, the **z**-axis contraction is unnecessary. This contraction is a function of the ionic radii of the rare earth atom in the **A**-site, thus $InFeO_3$ and $InMnO_3$ are structurally unique compared to $YAlO_3$ and $YFeO_3$.[44]

D. Conclusions

The structure of $InFeO_3$ is isostructural with that of $InMnO_3$.(Section 3.2) One important difference between the two structures should be stressed, however. The **c**-axis of $InFeO_3$ is almost 1Å larger than the **c**-axis of $InMnO_3$, even though the ionic radii of manganese and iron are identical according to Shannon. Since the transition metal coordination is ideal D_{3h}, the occupation of the d_z^2 orbital for high spin Fe(III) requires a weakening and lengthening of the apical bond resulting in the unusually large **c**-axis. The

c-axis of $InFeO_3$ is almost 2Å larger than the c-axis of $YAlO_3$. In this case, the difference in lattice parameters is caused by the higher coordination of yttrium in $YAlO_3$.

Section 3.4: $InMn_{1-x}Fe_xO_3$

A. Experimental

1. Preparation of polycrystalline samples

Polycrystalline samples of the solid solution $InMn_{1-x}Fe_xO_3$, x = 0.25, 0.5, and 0.75, were prepared by the nitrate decomposition technique described in Section 3.2. Using a 10 mmol scale, a stoichiometric amount of $In(OH)_3$ (Johnson Matthey, 99.999%) was dissolved in 150 mL of concentrated HNO_3 with Mn(II) acetate tetrahydrate (Johnson Matthey, 99.999%) and Fe(II) oxalate dihydrate (reagent) in a 400 mL beaker. Excess indium was not required when preparing $InMn_{1-x}Fe_xO_3$.

The beaker of the nitric acid solution was heated on a hotplate at low heat with stirring until the solution became pale yellow to yellow-brown, depending on the value of x. The temperature of the hotplate was then increased to cause slow evaporation of the liquid. All of the acid was evaporated to leave a brown, oily solid. An additional 50 mL of nitric acid was added, redissolving the precursor with stirring. The brown solution was stirred over low heat until approximately 10 mL of liquid remained. The beaker was then removed from the hotplate allowing the brown slurry to partially solidify. The beaker was placed into a box furnace and heated to 400°C for 12 hours during which time the precursor decomposed into a low-density, brown to black solid. The solid was ground in an agate mortar and

sealed in an evacuated quartz tube. The quartz tube was heated to 900°C for 72 hours, grinding every 24 hours, resulting in a crystalline, black product. The excess pressure present during the preparation of $InMnO_3$(Section 3.2) was noticeable less as the value of x becomes larger until no excess pressure is present when x =0.75. For x = 0.5 and 0.75, transparent blue crystals of an unknown phase were present on the interior of the quartz tube. The blue impurity phase was analyzed using precession photography. Polycrystalline samples were structurally characterized by powder X-ray diffraction on a Rigaku RU300 rotating anode diffractometer operating at 10kW with Cu Kα radiation (λ = 1.54184Å).

2. *Magnetic measurements*

Magnetic data were collected on finely ground polycrystalline samples using a Quantum Design MPMS SQUID magnetometer at temperatures ranging from 2 to 300K and applied fields ranging from 0.1 to 50kG. A scan length of 6 cm was used and 20 measurements were performed over the scan length. A total of 3 scans were averaged for each data point. All data were corrected for the diamagnetic contribution on a Kel-F sample holder. Core diamagnetism corrections for the substituent elements were not applied. All samples were zero-field cooled and measured by heating unless otherwise noted.

3. *Mössbauer spectroscopy*

Mössbauer spectra of various iron doping levels of $InMn_{1-x}Fe_xO_3$ between $0.25 \leq x \leq 0.75$ were obtained using a conventional constant acceleration spectrometer. Sample temperatures in the range $4.2K \leq T \leq 300K$ were achieved by the use of a Janis Supervaritemp dewar and a Lake Shore temperature controller. The source was $^{57}Fe(Rh)$ maintained at room

temperature. Isomer shifts are reported relative to metallic iron at room temperature.

B. Results

The members of the solid solution $InMn_{1-x}Fe_xO_3$, where **x** = 0.25, 0.5, and 0.75, were prepared and characterized by powder X-ray diffraction. Samples could be indexed to a cell having the approximate dimensions, **a** = 3.3Å and **c** = 11.75Å, isostructural to the $P6_3/mmc$ version of $InMnO_3$.(Figure 3.2.1) Lattice parameters are shown in Figure 3.4.1. No evidence of the $P6_3cm$ structure was seen in the powder patterns of $InMn_{1-x}Fe_xO_3$. The **a**-axis decreases with increasing **x**, while the **c**-axis increases with increasing **x**. Both axes change in a nonlinear fashion.

The magnetic behavior of the solid solution $InMn_{1-x}Fe_xO_3$ is similar to that observed for $InMnO_3$. There is apparent antiferromagnetic behavior at low temperatures and very low fields for $InMn_{0.75}Fe_{0.25}O_3$.(Figure 3.4.2) With an increasing external field, the material loses its apparent antiferromagnetic transition and begins to flatten out below the previous Néel temperature, 15K.(Figures 3.4.2b,c) Application of higher fields (40kG) results in behavior similar to that seen in $InMnO_3$.(Figure 3.2.4)

When **x** = 0.75, the susceptibility *vs.* temperature plot is different than that observed for either **x** = 0.25 and 0.5.(Figure 3.4.3) For $InMn_{0.25}Fe_{0.75}O_3$, the susceptibility never decreases with decreasing temperature after reaching a susceptibility maximum. Instead, the susceptibility for this material develops a step beginning with a plateau at the approximate temperature where $InMn_{0.75}Fe_{0.25}O_3$ displays a susceptibility maximum. The susceptibility remains stable for approximately ten degrees from 20K to 10K before

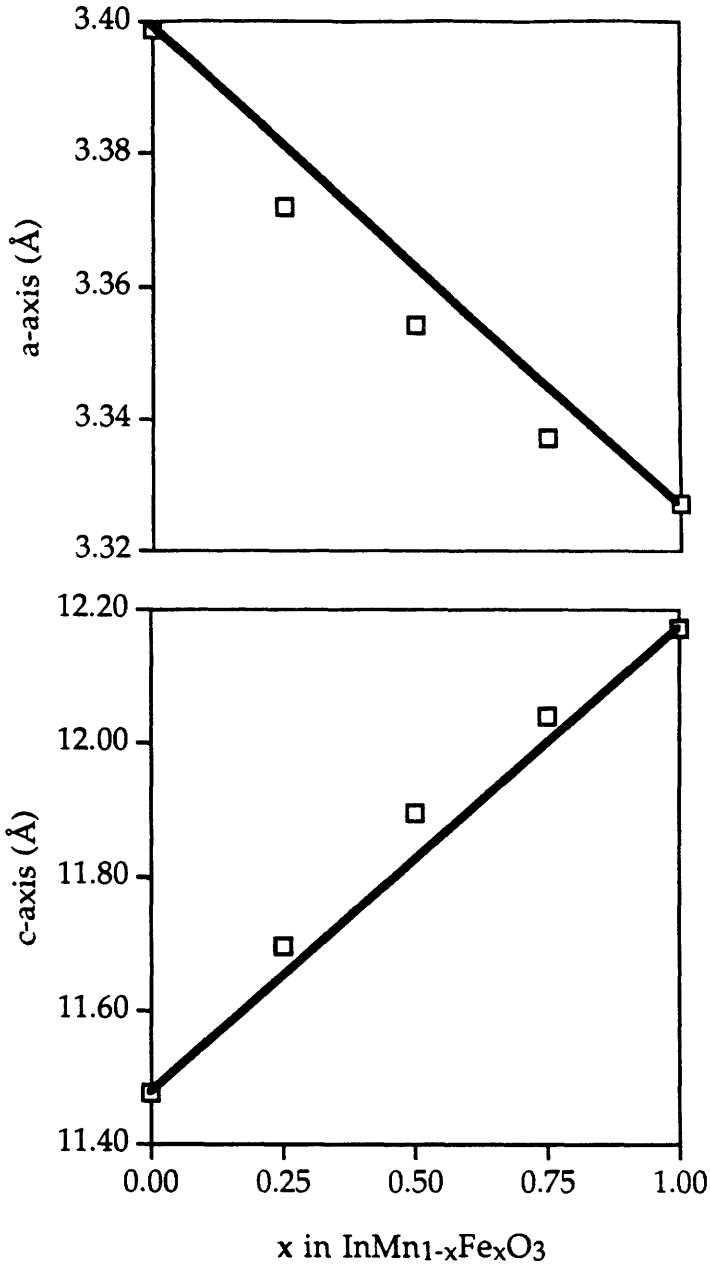

Figure 3.4.1 Change in lattice parameters *vs.* change in stoichiometry of the solid solution $InMn_{1-x}Fe_xO_3$. The solid line is the change lattice parameters expected according to Vegard's Law.

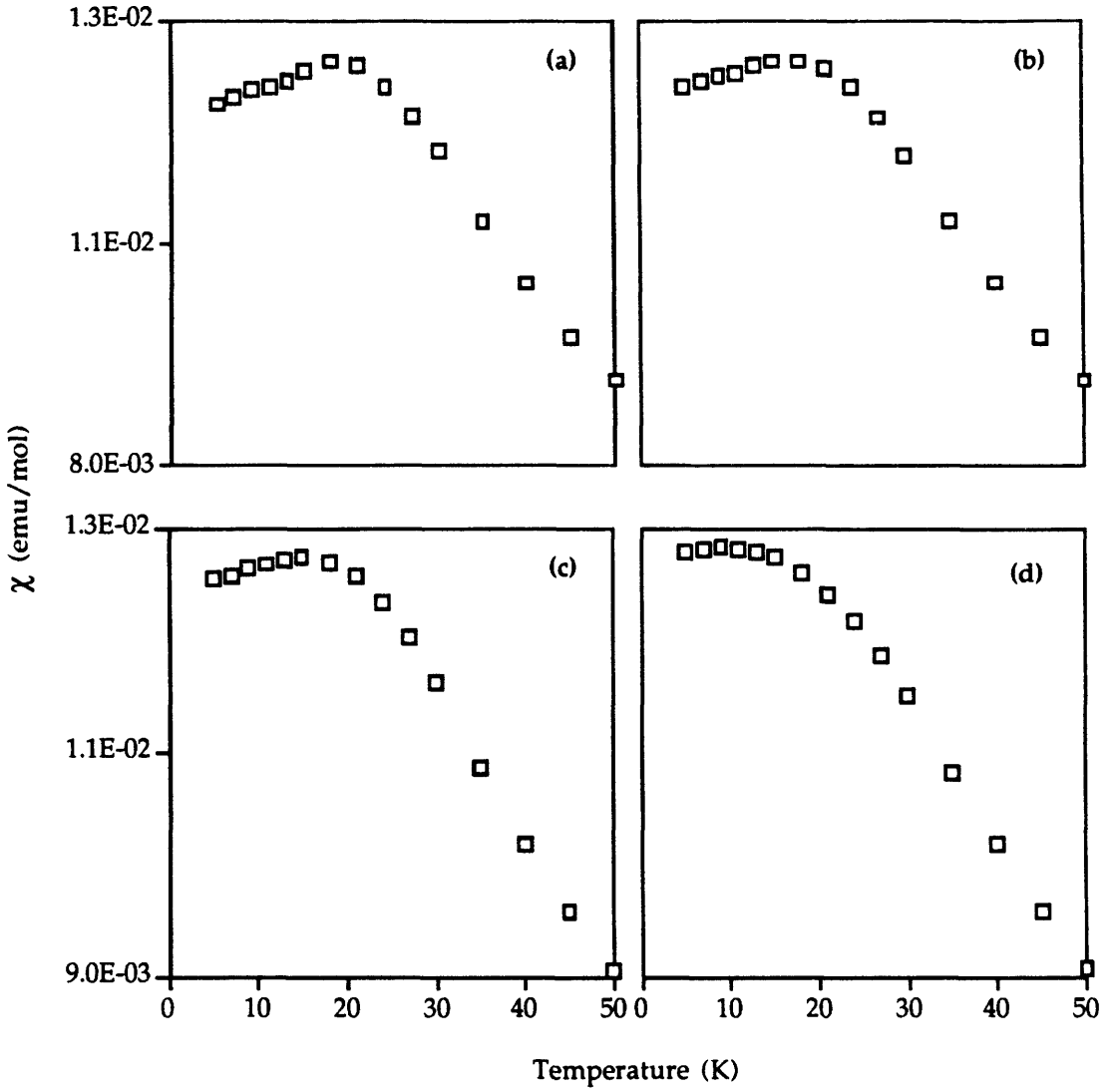

Figure 3.4.2 Magnetic susceptibility *vs.* temperature for $InMn_{0.75}Fe_{0.25}O_3$ at several fields. (a) 0.1kG; (b) 0.5kG; (c) 1kG; (d) 2.5kG.

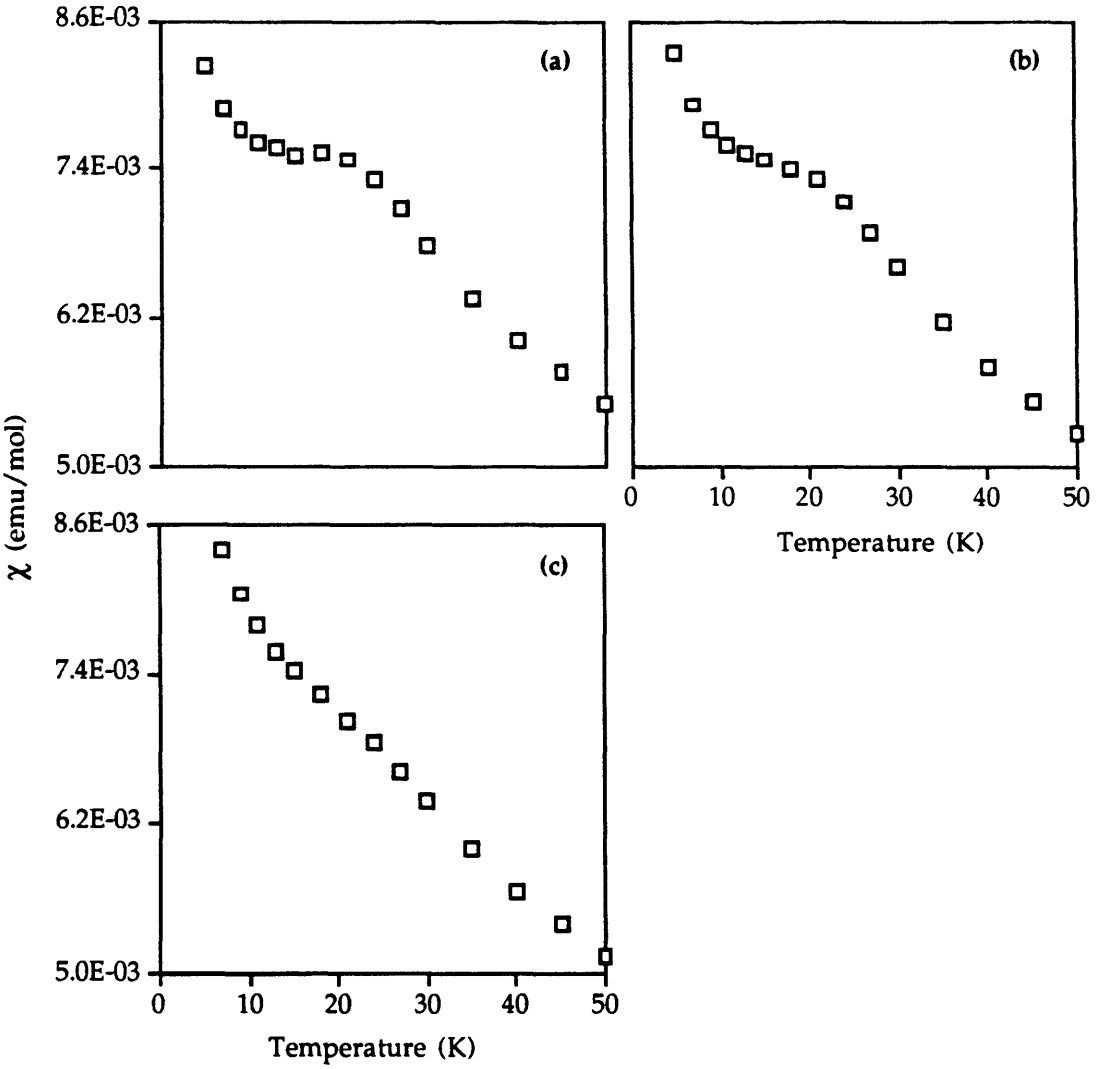

Figure 3.4.3 Magnetic susceptibility *vs.* temperature for $InMn_{0.25}Fe_{0.75}O_3$ at several fields. (a) 0.1kG; (b) 0.5kG; (c) 2.5kG.

continuing to increase with decreasing temperature. Field dependence studies were performed in order to determine whether or not the increasing susceptibility was evidence of a ferromagnetic contribution at temperatures below 15K. The solid solution member $InMn_{0.25}Fe_{0.75}O_3$ does not appear to display ferromagnetic behavior even at fields as high as 50kG. The field *vs.* magnetization plot for $InMn_{0.25}Fe_{0.75}O_3$ does not reach a stable maximum, *i.e.* the magnetic moment of $InMn_{0.25}Fe_{0.75}O_3$ is not fully saturated nor does it closely approach its saturation value.(Figure 3.4.4) If susceptibility *vs.* temperature is plotted for $InMn_{0.25}Fe_{0.75}O_3$, however, several magnetic regimes are apparent.(Figure 3.4.5) At low temperatures and low fields (Figure 3.4.5a) the susceptibility increases with increasing field until approximately 1kG, after which the susceptibility steadily decreases with increasing field. At higher temperatures, (Figures 3.4.5b,c), the susceptibility decreases with increasing field until stabilizing at high fields.

The Mössbauer spectra of the solid solution displays behavior similar to that seen in $InMnO_3$ by neutron diffraction. Magnetic ordering is readily apparent above 100K.(Figure 3.4.6) At 150K, the Mössbauer spectrum clearly shows the presence of only one iron coordination site with an isomer shift consistent with the value reported for $InFeO_3$.[5] When the temperature reaches 100K, the 6-line spectrum characteristic of magnetic ordering is clearly present. Figure 3.4.7 show the room temperature spectra for $InMn_{1-x}Fe_xO_3$ for **x** = 0.25, 0.5, and 0.75. The quadruple splitting value for $InMn_{1-x}Fe_xO_3$ increases in a linear fashion as **x** changes from 0.25 to 1.(Figure 3.4.8)

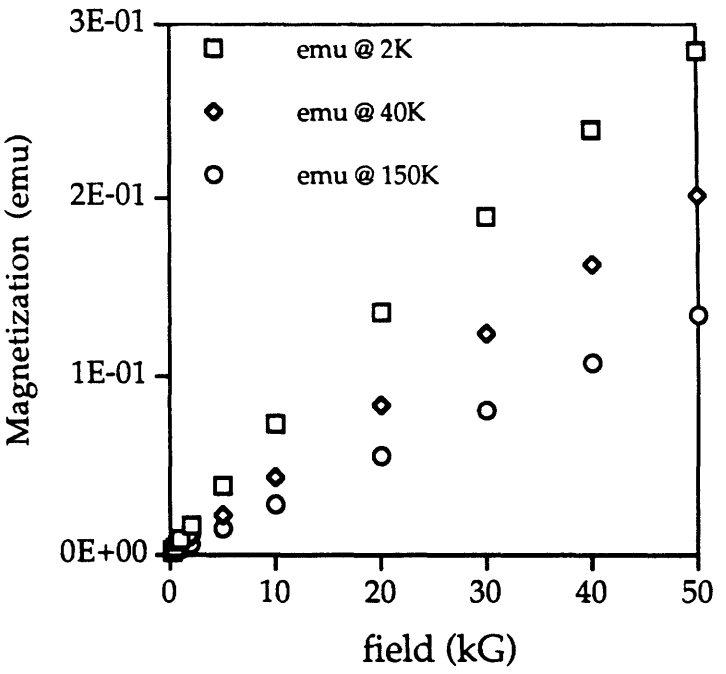

Figure 3.4.4 Magnetization *vs.* external field for $InMn_{0.25}Fe_{0.75}O_3$ at several temperatures. The magnetization curve does not reach saturation.

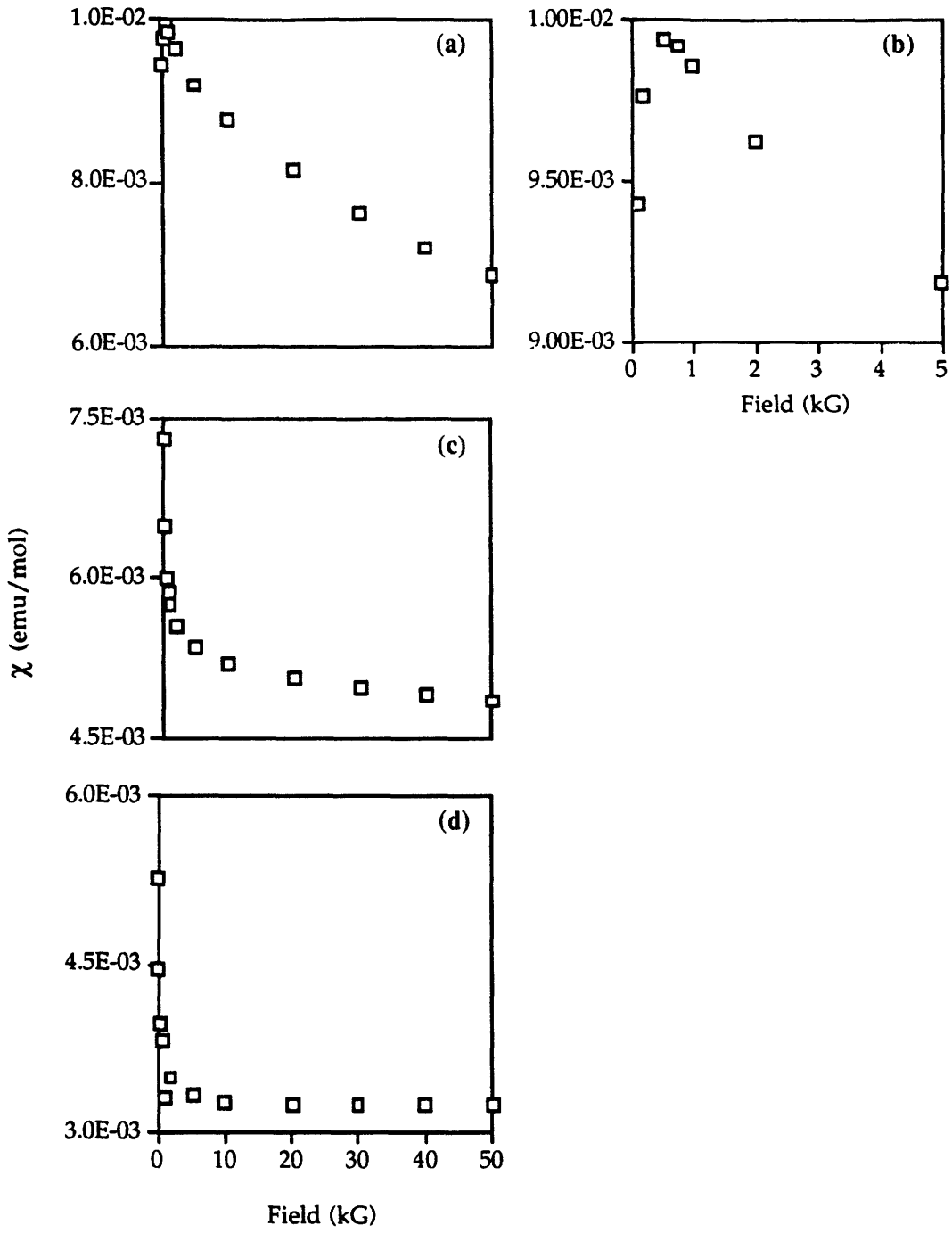

Figure 3.4.5 Susceptibility *vs.* external applied field for $InMn_{0.25}Fe_{0.75}O_3$ at several temperatures, (a) 2K, (b) 2K, low field values, (c) 40K, (d) 120K.

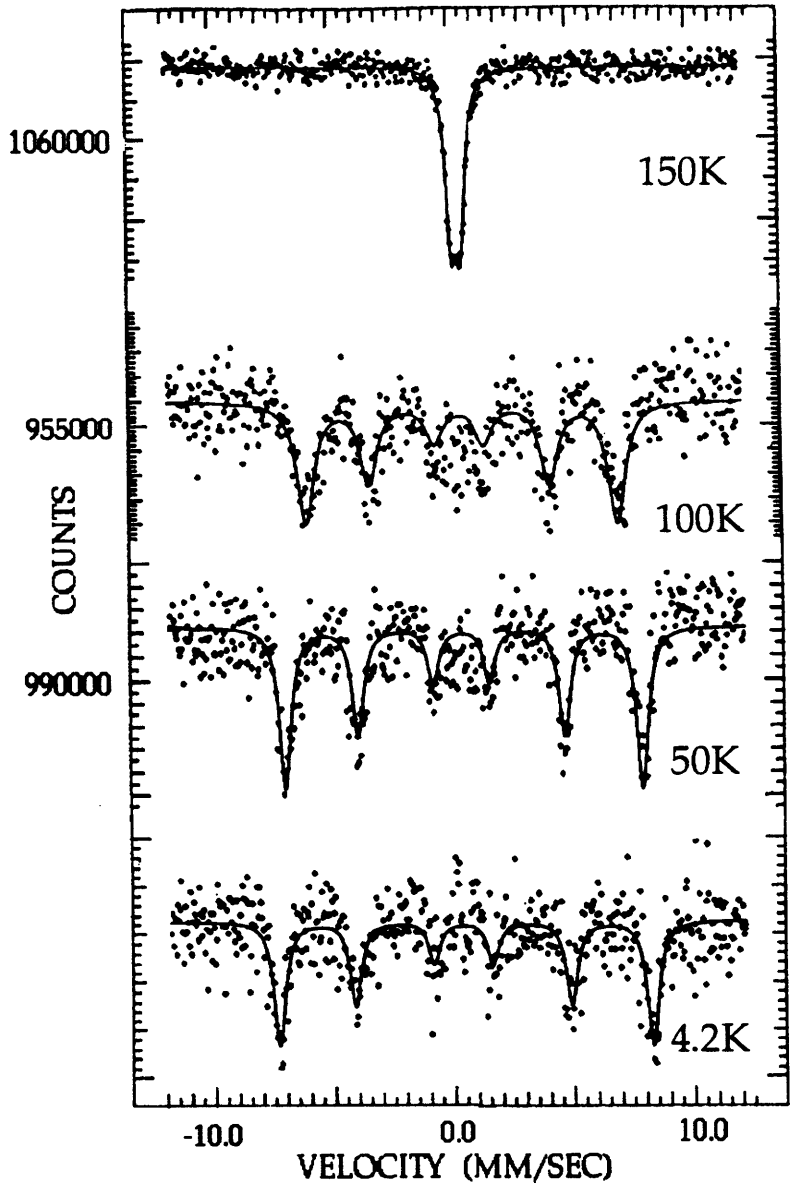

Figure 3.4.6 Mössbauer spectra for $InMn_{0.75}Fe_{0.25}O_3$ at several temperatures.

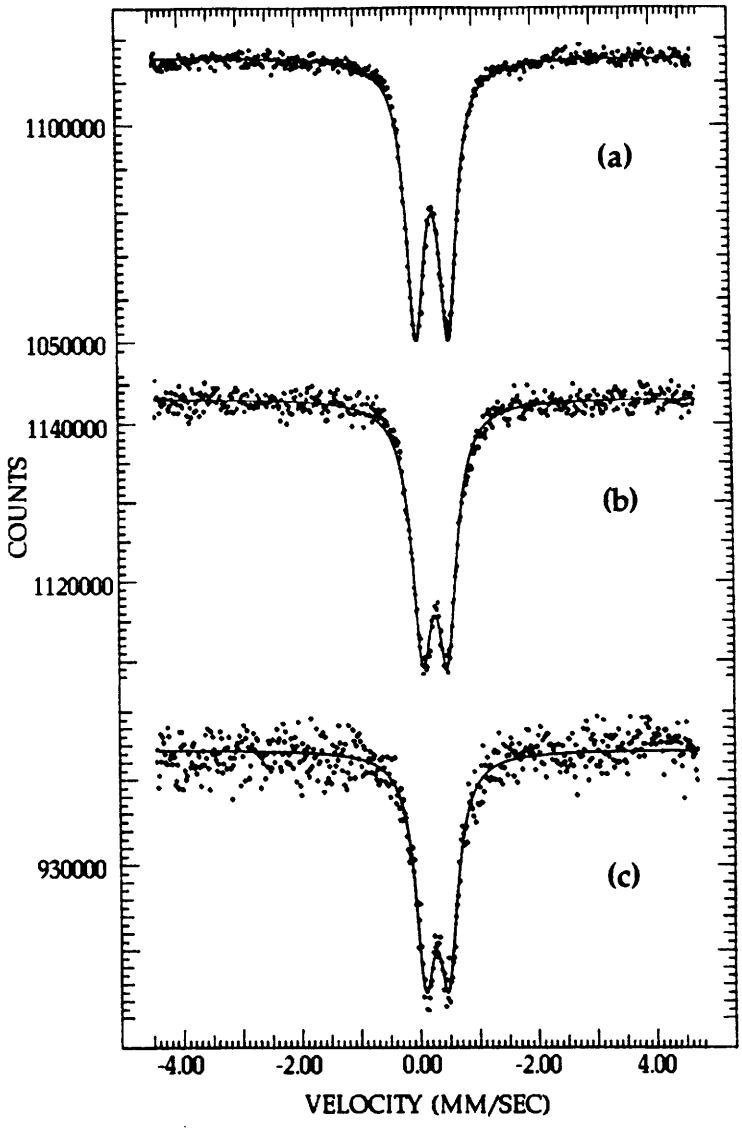

Figure 3.4.7 Room temperature Mössbauer spectra of $InMn_{1-x}Fe_xO_3$, (a) x = 0.75, (b) x = 0.5, (c) x = 0.25.

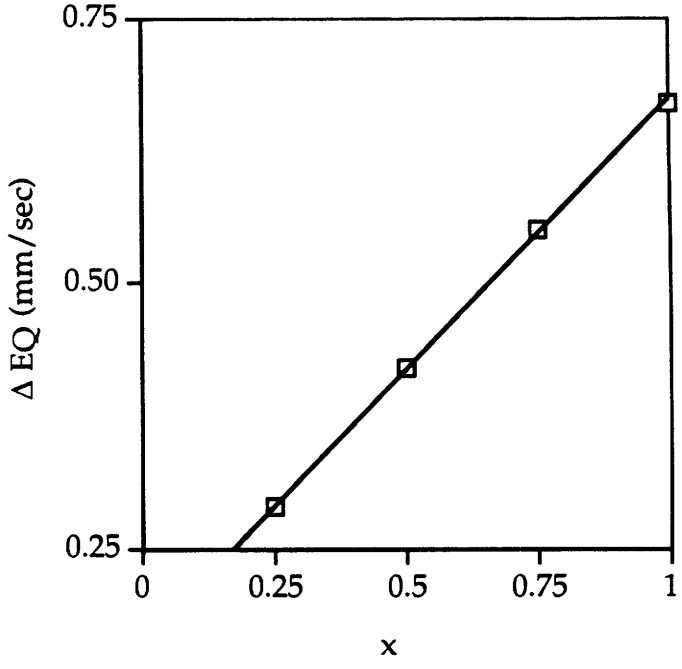

Figure 3.4.8 The relationship of the quadruple splitting, ΔE_Q, with the change in x for the solid solution $InMn_{1-x}Fe_xO_3$.

C. *Discussion*

According to powder X-ray diffraction, the members of the solid solution $InMn_{1-x}Fe_xO_3$ are isostructural with the single crystal structure of $InMnO_3$ and the previously reported structure of $InFeO_3$.[5,45,46] The acentric $P6_3cm$ structure(Section 3.2) is not formed, although the synthetic procedure for the preparation of polycrystalline $InMn_{1-x}Fe_xO_3$ and $InMnO_3$ is the same. Polycrystalline samples of $InFeO_3$ have never been reported as a single phase, perhaps due to the relative instability of this unusual hexagonal structure *vs.* the more stable sesquioxide structures, corundum and bixbyite. Considering this, the presence of iron and the electronic effects of a d^5 transition metal in trigonal bipyramidal coordination may preclude the formation of the acentric structure. Nevertheless, the presence of both manganese and iron allows the $P6_3/mmc$ structure to form preferentially.

The transparent blue crystals which crystallize when $x = 0.5$ and 0.75 have been tentatively assigned to the triclinic crystal class according to analysis by precession photography. No further identification procedures have been performed.

The lattice parameters of $InMn_{1-x}Fe_xO_3$ do not change in the manner expected according to Vegard's Law. The nonlinear change in the c-axis is most likely the result of the gradual filling of the d_z^2 orbital with its corresponding electronic effect. As iron is doped for manganese, a fraction of the d_z^2 orbitals are filled causing a gradual elongation of the trigonal bipyramidal apical bond and the c-axis. Since the c-axis of $InMn_{0.75}Fe_{0.25}O_3$ is already slightly larger than expected according to Vegard's Law, stabilization

due to the lengthening of the transition metal-oxygen apical bond seems to occur with only a small level of iron doping.

According to the Mössbauer spectra, magnetic order is present at significantly higher temperatures than seen by magnetic susceptibility measurements. This is analogous to the magnetic behavior seen in $InMnO_3$ by neutron diffraction. Since the Mössbauer effect, like neutron diffraction, occurs on a rapid time scale, we believe that the solid solution $InMn_{1-x}Fe_xO_3$ displays magnetic ordering at approximately 120K but that the magnetic correlations are visible only with regard to a very rapid time scale. Considering these similarities, it seems likely that the general magnetic structural characteristics of $InMnO_3$, including lack of long-range order in three dimensions and long range order within the transition metal-oxygen plane, are not disrupted by the replacement of manganese with iron. In fact, the presence of iron and the consequential lengthening of the c-axis may diminish the possibilities for long range order. The increase in susceptibility with decreasing temperature seen in $InMn_{0.25}Fe_{0.75}O_3$ is consistent with the susceptibility *vs.* field plots which clearly show the presence of a ferromagnetic contribution at low fields and low temperatures. This is likely due to additional frustration in the magnetic lattice as $^3/_4$ of the magnetic ions have five unpaired electrons while $^1/_4$ have only four. As the magnetic system attempts to order in an antiferromagnetic manner, frustration caused by the triangular metal-oxygen lattice and the difference in spin may result in ferrimagnetic ordering with a remnant of uncompensated spins. This behavior was seen in Chapter 2 when iron was replaced by diamagnetic gallium and aluminum resulting in uncompensated spins and a ferrimagnetic magnetic structure. The uncompensated spins in Chapter 2, however, were observed in addition to

long-range antiferromagnetic ordering, while in $InMnO_3$ and $InMn_{1-x}Fe_xO_3$ no true long-range order exists.

The linear change in the quadruple splitting value across the solid solution is indicative of a distortion in the iron coordination symmetry as x increases from 0.25 to 1. This is consistent with the $P6_3/mmc$ crystal structures of $InMnO_3$ and $InFeO_3$. The trigonal bipyramid in $InFeO_3$ is tetragonally distorted relative to the trigonal bipyramid in $InMnO_3$. The fact that the coordination symmetry is higher for $x = 0.25$ than for $x = 1$ confirms that the $P6_3/mmc$ structure is present for the members of the solid solution. The coordination symmetry of the transition metal in the $P6_3cm$ structure is significantly lower, C_s *vs.* D_{3h}

E. Conclusions

The solid solution $InMn_{1-x}Fe_xO_3$ has been characterized by powder X-ray diffraction, magnetic susceptibility, and Mössbauer spectroscopy. The solid solution crystallizes in the centrosymmetric structure of both end members, $InMnO_3$ and $InFeO_3$, and not the noncentrosymmetric structure displayed by the polycrystalline sample of $InMnO_3$ and other rare earth manganates. When compared with the neutron diffraction data, the magnetic structure of $InMn_{1-x}Fe_xO_3$ is believed similar to $InMnO_3$ with a lack of true long-range magnetic correlations.

References

(1) Wells, A. F. *Structural Inorganic Chemistry;* 5th ed.; Clarendon Press: Oxford, 1984.

(2) Geller, S.; Curlander, P. J.; Jefferies, J. B. Acta Crystallogr. (1975) **B31**, 2770.

(3) Bertaut, F.; Mareschal, J. Compt. rend. (1963) **275**, 867.

(4) Gerardin, R.; Aqachmar, E. H.; Alebouyeh, A.; Evrard, O. Mat. Res. Bull. (1989) **24**, 1417.

(5) Nodari, I.; Alebouyeh, A.; Brice, J. F.; Gerardin, R.; Evrard, O. Mat. Res. Bull. (1988) **23**, 1039.

(6) Galasso, F. S. *Structure, Properties and Preparation of Perovskite Type Compounds*; Pergamon Press: Oxford, 1969.

(7) Goodenough, J. B.; Longo, J. M. *Landolt-Bornstein Tabellen, New Series, III;* 1970; Vol. 4a.

(8) Goodenough, J. B. Prog. in Solid State Chem. (1971) **5**, 145.

(9) Rao, C. N. R. Annu. Rev. Phys. Chem. (1989) **40**, 291.

(10) Smyth, D. M. Ann. Rev. Mater. Sci. (1985) **15**, 329.

(11) Yakel Jr., H. L. Acta Crystallogr. (1955) **8**, 394.

(12) Mouron, P.; Choisnet, J.; Abs-Wurmach, I. Eur. J. Solid State Inorg. Chem. (1989) **26**, 35.

(13) Norrestam, R. Acta Chem. Scand. (1967) **21**, 2871.

(14) Schneider, S. J.; Roth, R. S.; Waring, J. L. J. Research NBS (1961) **65A**, 345.

(15) Goldschmidt, V. M. Mat.-Naturv. Kl. (1926) **2**, 117.

(16) Newnham, R. E.; Fang, J. H.; Santoro, R. P. Acta Crystallogr. (1964) **17**, 240.

(17) Chamberland, B. L.; Sleight, A. W.; Weiher, J. R. J. Solid State Chem. (1970) **1**, 512.

(18) Takeda, Y.; Kanamaru, F.; Shi Madra, M.; Koizumi, M. Acta Crystallogr. (1976) **B32**, 2464.

(19) Burbank, R.; Evans Jr., H. Acta Crystallogr. (1948) **1**, 330.

(20) Longo, J. M.; Raccah, R. M.; Goodenough, J. B. Mater. Res. Bull. (1969) **4**, 191.

(21) Goodenough, J. B.; Kafalas, J. A. J. Solid State Chem. (1973) **6**, 493.

(22) Hong, H. Y.; Kafalas, J. A.; Goodenough, J. B. J. Solid State Chem. (1974) **9**, 345.

(23) Cromer, D. T.; Waber, J. T. In *International Tables for X-ray Crystallography, Table: 2.2A* The Kynoch Press: Birmingham, England, 1974; Vol. IV.

(24) Walker, N.; Stuart, D. Acta Crystallogr. (1983) **A39**, 158.

(25) Swepston, P. N. In Molecular Structure Corporation: 1985.

(26) Sheldrick, G. M. *Crystallographic Computing;* Oxford University Press: 1985; Vol. p. 175.

(27) Cromer, D. T.; Waber, J. T. In *International Tables for X-ray Crystallography, Table: 2.3.1* The Kynoch Press: Birmingham, England, 1974; Vol. IV.

(28) Shannon, R.; Rogers, D.; Prewitt, C. Inorganic Chem. (1971) **10**, 719.

(29) Wells, A. F. *Three-Dimensional Nets and Polyhedra;* Wiley: New York, 1977.

(30) Yakel, H. L.; Koehler, W. C.; Bertaut, E. F.; Forrat, E. F. Acta Crystallogr. (1963) **16**, 957.

(31) Carlin, R. L. In *Magnetochemistry* Springer-Verlag: Berlin, 1986; pp 163.

(32) Kimizuka, N.; Mohri, T. J. Solid State Chem. (1989) **78**, 98.

(33) Bertaut, E. F.; Buisson, G.; Durif, A.; Mareschal, J.; Montmory, M. C.; Quezel-Ambrunaz, S. B. S. chim. Fr. (1965) 1132.

(34) Lukaszewicz, K.; Karut-Kalicinska, J. Ferroelectrics (1974) **7**, 81.

(35) Murphy, D. W.; Schneemeyer, L. F.; Waszczak, J. V. In *Chemistry of High-Temperature Superconductors II* American Chemical Society: Washington, DC, 1988; Vol. Chapter 24; pp 315.

(36) Müller-Buschbaum, H. Angew. Chem. (1989) **101**, 1503.

(37) Ramos, E.; Veiga, M. L.; Fernández, F.; Sáez-Puche, R.; Pico, C. J. Solid State Chem. (1991) **91**, 113.

(38) Cyrot, M.; Lambert-Andron, B. J. Solid State Chem. (1990) **85**, 321.

(39) De Jongh, L. J.; Miedema, A. R. Advances in Physics (1974) **23**, 1.

(40) Bertaut, E. F.; Mercier, M.; Pauthenet, R. J. Physique (1964) **25**, 550.

(41) Wright, A. C.; Wagner, C. N. J. J. Non-Cryst. Solids (1988) **106**, 85.

(42) Giaquinta, D. M.; zur Loye, H.-C. J. Amer. Chem. Soc. (1992) **114**, 10952.

(43) Shannon, R. D. Acta Crystallogr. (1976) **A32**, 751.

(44) Yamaguchi, O.; Takemura, H.; Yamashita, M.; Hayashida, A. J. Electrochem. Soc. (1991) **138**, 1492.

(45) Gérardin, R.; Aqachmar, E. H.; Alebouyeh, A.; Evrard, O. Mat. Res. Bull. (1989) **24**, 1417.

(46) Giaquinta, D. M.; zur Loye, H.-C. Acta Crystallogr. (1993) **49C**, in press.

CHAPTER 4

STRUCTURAL PREDICTION WITHIN THE ABO_3 PHASE DIAGRAM

Section 4.1: Structural prediction methods

A. Introduction

The rational design of materials assumes an understanding of the correlation between basic crystal chemistry and simple structure-property relationships. Implicit in such a relationship is an understanding of the connection between chemical composition and crystal structure in solid state materials. Parameters such as electronegativity, radii, valence electron count, and principal quantum number may help to establish a link between composition, structure and properties for different classes of materials. Establishing such a link is particularly difficult due to the large number of parameters which affect structures, *e.g.* the charge and coordination preference of metals, the existence of energetically close-lying structure types, as well as synthetic parameters such as temperature. The use of high pressure or low temperature synthesis further complicates the problem because of kinetic considerations and the synthesis of metastable phases. Numerous attempts have been made to correlate structural stability with chemical or physical variables derived from atomic properties of the constituent elements, and for different classes of materials, different atomic properties must be used to achieve good correlation.[1]

Thus, structural prediction for previously unprepared compounds based on easily obtainable parameters remains an important problem in the preparation of new materials with extended structures. Structure-types of new compositions often may be predicted accurately if the synthesis involves a cationic, isovalent substitution in a known structure, see Chapter 2, however, structural prediction for new combinations of elements, both

cations and anions, remains troublesome. The problem of structural prediction has been addressed by many researchers[2-17] who have employed coulombic, geometric, and quantum mechanical parameters in attempts to model known structures accurately and to predict the structures of as of yet unprepared compounds. Although the method based on pseudopotential radii and electronegativity described by Villars[14-17] has proven quite successful for intermetallic compounds, a different type of technique is necessary to deconvolute the complex interactions that determine the structure of compounds with mixed ionic-covalent character, for example, transition metal oxides.

The problem of structural prediction is particularly acute for transition metal oxides due to the large degree of ionic-covalent bonding present in such materials and due to competing interactions that this type of bonding generates. These interactions include lattice energies, a coulombic contribution;[18] crystal-field stabilization energies, an electronic contribution;[19] and geometric packing effects, a steric contribution. Because of this complexity, competing structures may have energy differences on the order of only 0.1 eV/atom.[20] Different structure types may be energetically very similar, therefore predicting into which structure group a certain stoichiometry will crystallize is quite difficult. Consequently, while accurate predictive methods exist for organic compounds, inorganic molecular complexes,[19] metals and alloys,[3,6,16] the many competing interactions that contribute to the final structure of an ionic-covalent crystal lattice leaves the area of ionic compounds without an equally reliable technique. Thus, in the analysis of transition metal oxides, as discussed in this chapter, there is difficulty both **(a)** in the accurate prediction of structures and **(b)** in the

rationalization of structures after they are determined. Although several techniques do exist, *vide infra*, each has noticeable shortcomings. In this chapter a new method for structural prediction using a combination of ionic radii and bond ionicities is described. Although related to an earlier method described by Mooser and Pearson,[8] the use of ionic radii instead of principal quantum number should give more specific information concerning the influence of the ionic bonding known to exist in oxides. Particularly through the combination of ionic radii and valence-specific electronegativity,[21] the subtle differences between the oxidation states of a given element can be exploited in the attempt to structurally segregate $\mathbf{ABO_3}$ compounds. The use of oxidation state-specific electronegativities and ionic radii for a given element is crucial since many examples exist where a simple metal oxide crystallizes in unrelated structures for each oxidation state, *e.g.* the corundum structure of Ti_2O_3 *vs.* the rutile structure of TiO_2. Using the combination of ionic radii and bond ionicities, the $\mathbf{ABO_3}$ structural phase diagram is discussed, particularly as it applies to the two new indium transition metal oxides, $InMnO_3$ and $InFeO_3$, that were described in Chapter 3. Using the previously developed prediction techniques in conjunction with the method described below, more insight may be gained on the $\mathbf{ABO_3}$ structural phase diagram than with either used alone.

B. Background

In the past, relationships between structure and composition have been based primarily on close-packing or non-directional ionic bonding using space filling, symmetry, and connectivity arguments.[7] Structural arguments based on the simple theory of coulombic interactions inevitably leads to radius-ratio rules. Radius-ratio rules, in spite of some shortcomings, have enjoyed much

popularity[2] due to the ease with which they provide structural predictions from readily available factors. This approach was limited to simple, strictly ionic compounds and, consequently, the directionality of bonding was introduced to establish improved relationships between structure and elemental composition. Early examples include the Hume-Rothery rules,[6] the Brewer-Engel theory,[3] and more recently, the quantum structural diagrams by Villars which systematize the relationship between composition and structure for intermetallic compounds with good success.[15]

To generalize directional bonding arguments successfully, the problem of identifying parameters that accurately represent the character and directionality of bonding becomes acute. One obvious parameter giving information regarding the character of a bond is electronegativity. The larger the difference in electronegativity ($\Delta\chi$) between two bonded atoms, the greater the ionicity of the bond, while a smaller electronegativity difference indicates greater covalency or metallic character. A second parameter providing a more direct connection to the directionality of a bond is given by **n**, the principle quantum number of an atom. As **n** increases, the atomic orbitals involved in bond formation become more diffuse and consequently the bonds lose their directional character. This concept of directionality was utilized by Mooser and Pearson to predict structures for $\mathbf{A_aB_b}$ semiconductors containing main group and transition metals.[8] Using an average quantum number, $\overline{n}$, Mooser and Pearson applied the bond directionality principle and demonstrated that different $\mathbf{A_aB_b}$ structures fall into distinct $\overline{n}$ *vs.* $\Delta\chi$ regions. This approach was successful for binary main group as well as binary transition metal compounds.

A more recent refinement introduced by Phillips and Van Vechten[9,10,12,13] uses a spectroscopically defined ionicity for chemical bonds in $\mathbf{A^N B^{8-N}}$ compounds with great accuracy. The need for spectroscopic measurements, however, decreases the ability to use this method in a predictive fashion.

Another approach for predicting intermetallic compounds was taken by Villars[14-17,20,22,23] who used three-dimensional structural stability diagrams to correlate structures with atomic properties. Villars plotted pseudopotential radius sums *vs.* an average valence electron count *vs.* differences in the Martynov-Batsanov[21] electronegativities. This approach works well for binary, ternary and quaternary intermetallic compounds and achieves good separation between different structures. Pseudopotential radii, however, are atomic parameters highly correlated with atomic number. Pseudopotential trends in radius ratios are significantly different than trends for ionic radii, and differences due to oxidation state are entirely absent. Consequently, pseudopotential radii are not useful when describing ionic materials.[24]

While the above approaches have been successful for intermetallic materials, the approach must be modified when analyzing oxides. Different properties are indicative of the basic characteristics of an ionic *vs.* an intermetallic structure. For ternary ionic structures, the different properties of the **A** and **B** cations should be treated separately rather than averaged, and furthermore, for ionic materials, the properties of cations and anions must be considered separately. Compounds containing regions with differing ionicities are also a consideration, particularly compounds with low dimensional structural units which contain non-interpenetrating slabs of **A-O** and **B-O**, such as the structures of $InMnO_3$ and $InFeO_3$.(Chapter 3)[25,26] Roth, who investigated the structures of $\mathbf{A^{3+}B^{3+}O_3}$ compounds,[11,27-29] used the concept of radius ratios to

deal with both cations independently, and plotted the radius of **A** *vs.* the radius of **B**. This approach, shown in Figure 4.1.1, separates the main structure types: A-M_2O_3 and B-M_2O_3, perovskite, bixbyite (C-M_2O_3), and corundum (α-Al_2O_3).[29-39] Although materials crystallizing in the ilmenite structure are generally $\mathbf{A^{2+}B^{4+}O_3}$, this structure type has been included for completeness. This method has proven useful for gross structural separations, however, the regions bordering different structural types are not well defined, particularly in the area of the corundum, ilmenite and bixbyite structures, *i.e.* when both the **A** and **B** cations are fairly small.

Other methods, including those of Villars,[17] have been applied to the problem of ternary and quaternary ionic compounds, however, the Villars method requires the averaging of atomic properties of the metals present. In the case of a compound with low-dimensional structural units, averaging would, by necessity, conceal the differences between metals that may be responsible for the formation of a layered structure. By treating each metal separately, the differences between metals can be directly observed using a combination of bond ionicities and ionic radii.

In the following sections, ideas concerning structural stability diagrams of $\mathbf{ABO_3}$ materials are presented. The common $\mathbf{ABO_3}$ structure types are described and compared with the $InMO_3$ structure type. (Chapter 3) Using a combination of radius ratios and bond ionicities the existence of the $InMO_3$ structure type is discussed within the context of the common $\mathbf{ABO_3}$ structure types, perovskite, corundum, ilmenite, and bixbyite (C-M_2O_3).

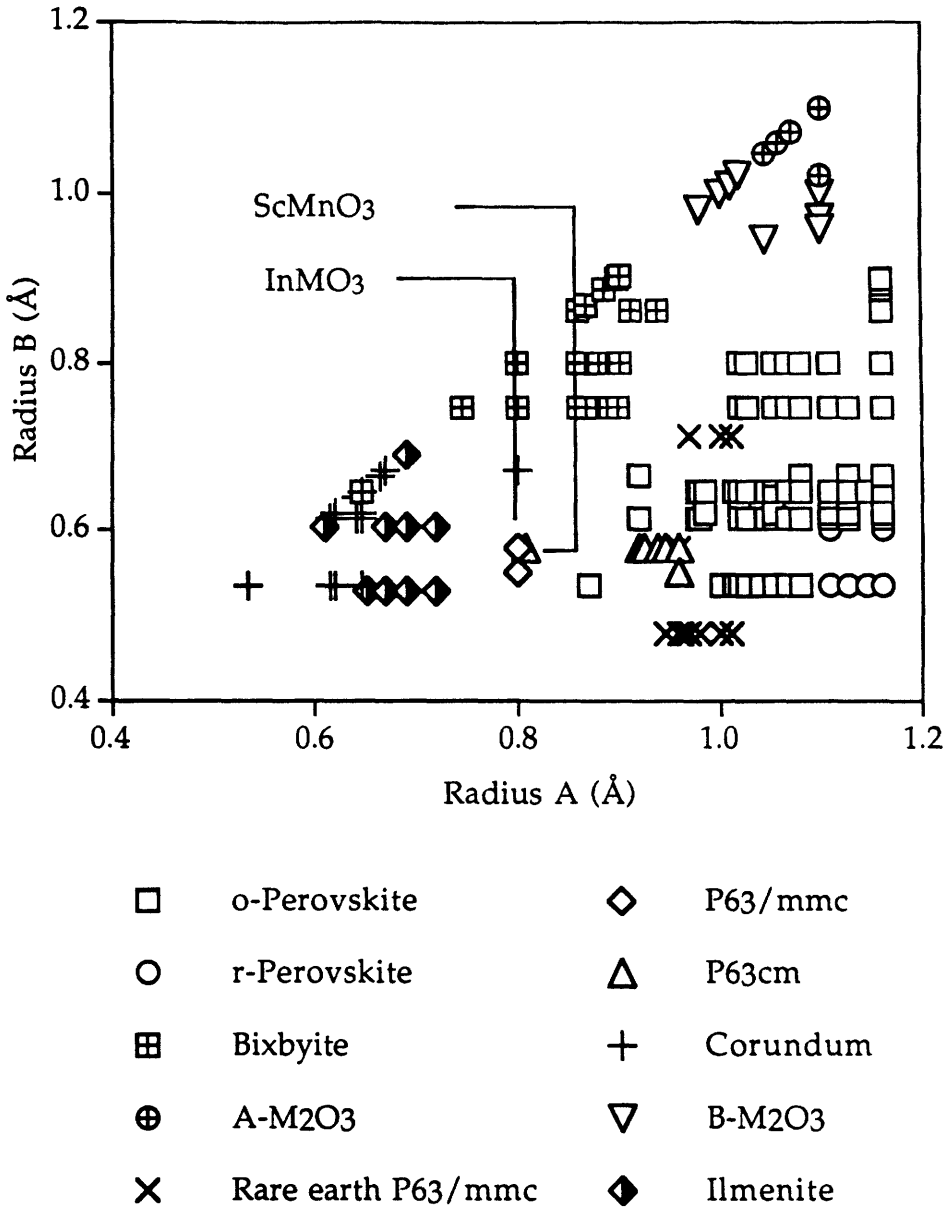

Figure 4.1.1 Ionic radii **A** *vs.* ionic radii **B** for compounds of the common ABO_3 structure types.(After Roth[11]) Included compounds are listed in Table 4.1.1.

C. *Discussion of ABO_3 structures*

Ionic solids can be discussed using a combination of electrostatic and geometrical arguments which lead to general approaches for predicting and rationalizing structures based on valence, coordination number, and ionic radii of the cations and anions. Generally, for trivalent $\mathbf{ABO_3}$ structures, there exist two extreme cases: (1) **A** and **B** cations of approximately equal size and of a size suitable for coordination within the octahedral interstitial site of a closest-packed oxide framework, and (2) an **A** cation comparable in size to $\mathbf{O^{2-}}$ which together with oxygen can form $\mathbf{AO_3}$ closest-packed layers with high coordination numbers in the **A** site.[40] Oxides of the first group tend to adopt sesquioxide structures, such as corundum (α-Al_2O_3),[29,40] or ilmenite,[38,39] while oxides of the second group form linked $\mathbf{BO_6}$ octahedra and $\mathbf{AO_3}$ closest-packed layers, such as perovskite,[30,31] $BaNiO_3$,[41] or hexagonal $BaTiO_3$ type structures.[42] Uncommon structure types, *e.g.* $PbReO_3$,[43] the tunnel structure of $KSbO_3$,[44,45] $InMnO_3$,[25] and $LuMnO_3$,[46] often crystallize on or near the border between the sesquioxide structures and the linked $\mathbf{BO_6}$ structures.

The corundum structure, α-Al_2O_3, (Figure 4.1.2) is formed by cations having the same oxidation state and/or similar radii, and consists of a hexagonal closest-packed oxygen framework in which the trivalent cations are randomly distributed in two thirds of the available octahedral interstices. The regular cation arrangement of the ilmenite structure, on the other hand, is preferred by cations having different oxidation states and/or different radii. According to geometric arguments, the octahedral interstices in close-packed oxygen layers will accommodate ions with radii approximately equal to $(\sqrt{2}-1)\,\mathbf{r}$ or $0.414\mathbf{r}$ where **r** is the radius of $\mathbf{O^{2-}}$, 1.38Å. This relationship, however, is an

approximation, and a certain degree of deviation from the ideal close-packed state may be expected.

The idealized perovskite structure (Figure 4.1.3) is cubic with the **A** cation in 12-fold coordination and the **B** cation in 6-fold coordination. The **A**-site is located at the body center of the cube, the **B**-site at each of the 8 corners, and the oxygen atoms at each of the centers of the 12 edges. Perovskite and distorted perovskite-type structures form for trivalent **A** and **B** cations having a range of radii, provided the **A** cation is large enough to form close-packed layers with O^{2-}, and the **B** cation is small enough to adopt an octahedral oxygen coordination environment. Under pressure, however, the stability range of the perovskite structure for smaller **A** cations can be increased. As the radius of the **A** cation decreases, the **A** and **B** cations will ultimately adopt a different crystal structure, often the corundum structure, which can better accommodate cations that are both smaller and closer in size to one another.

In the cation size regime bracketed by the lower stability range of the perovskite structure and the upper radius limitations of the corundum structure, the cubic rare earth structure, C-M_2O_3, or bixbyite,[47] often forms (Figure 4.1.4). The bixbyite structure is related to that of fluorite (CaF_2) and may be derived from the fluorite structure by the removal of one quarter of the anions and subsequent rearrangement. Two types of cation coordination environments are generated, both of which have six instead of eight neighbors at the vertices of a cube; two anions are missing at the ends of a body diagonal and two at the end of a face diagonal, respectively.

To predict which one of the above mentioned structures will be favored for a given pair of cations, the radius ratio or a more complex radius relationship

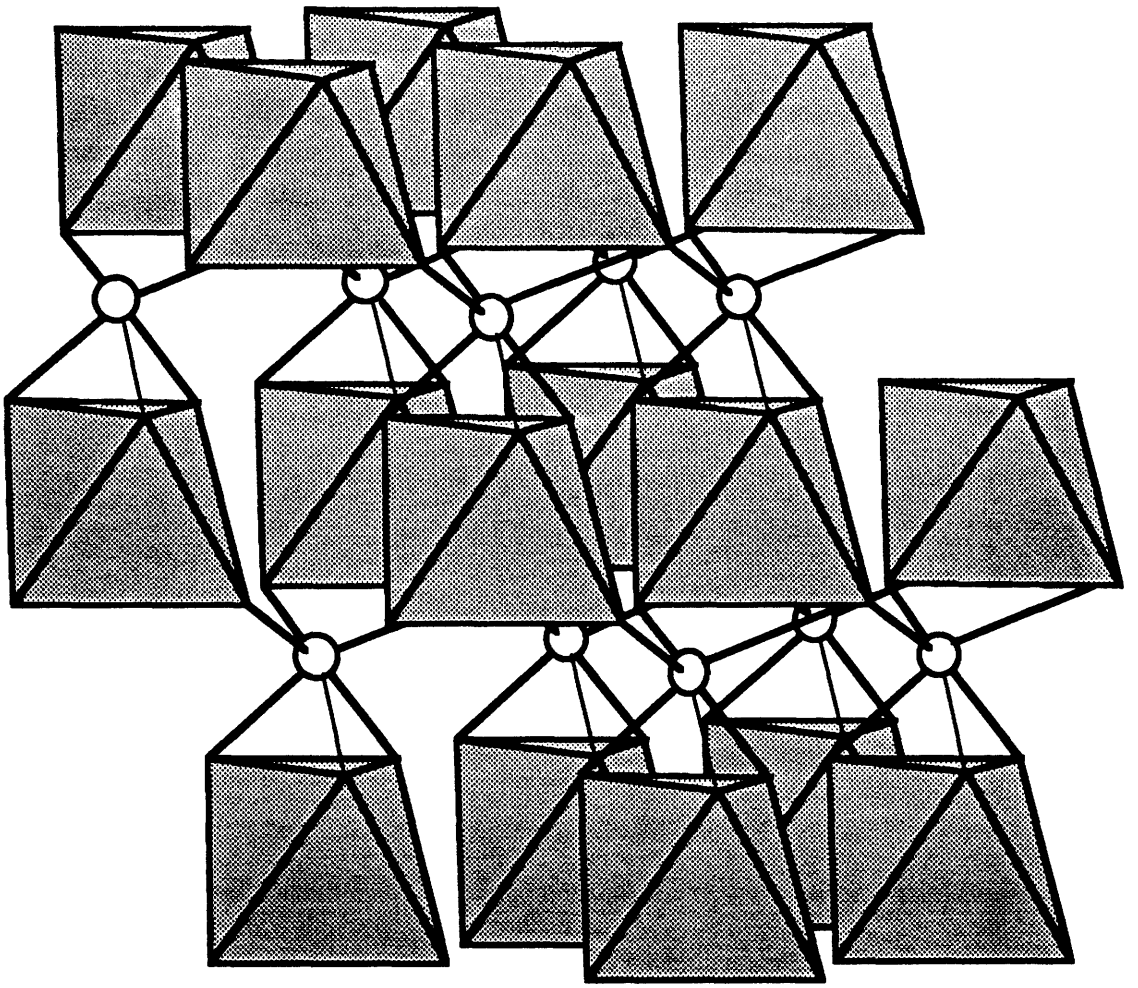

Figure 4.1.2 The corundum structure if both polyhedra and circles represent the same element or a statistical distribution of different elements; the ilmenite structure if the polyhedra and circles represent different elements in an ordered arrangement.

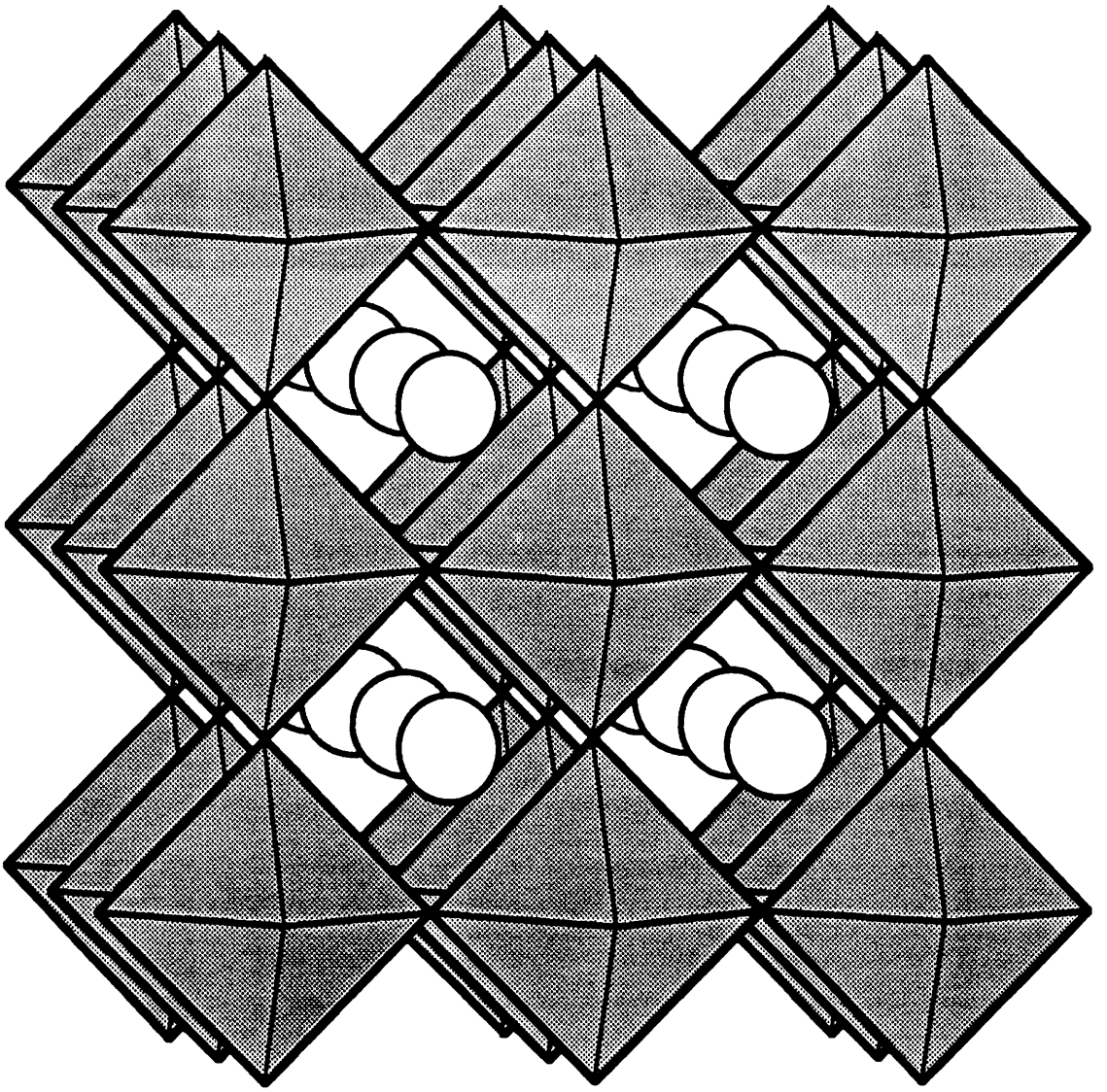

Figure 4.1.3 The perovskite structure. The **A** cations are represented by circles and the **B** cations are located at the center of the polyhedra; oxygen atoms are located at the apices of the polyhedra.

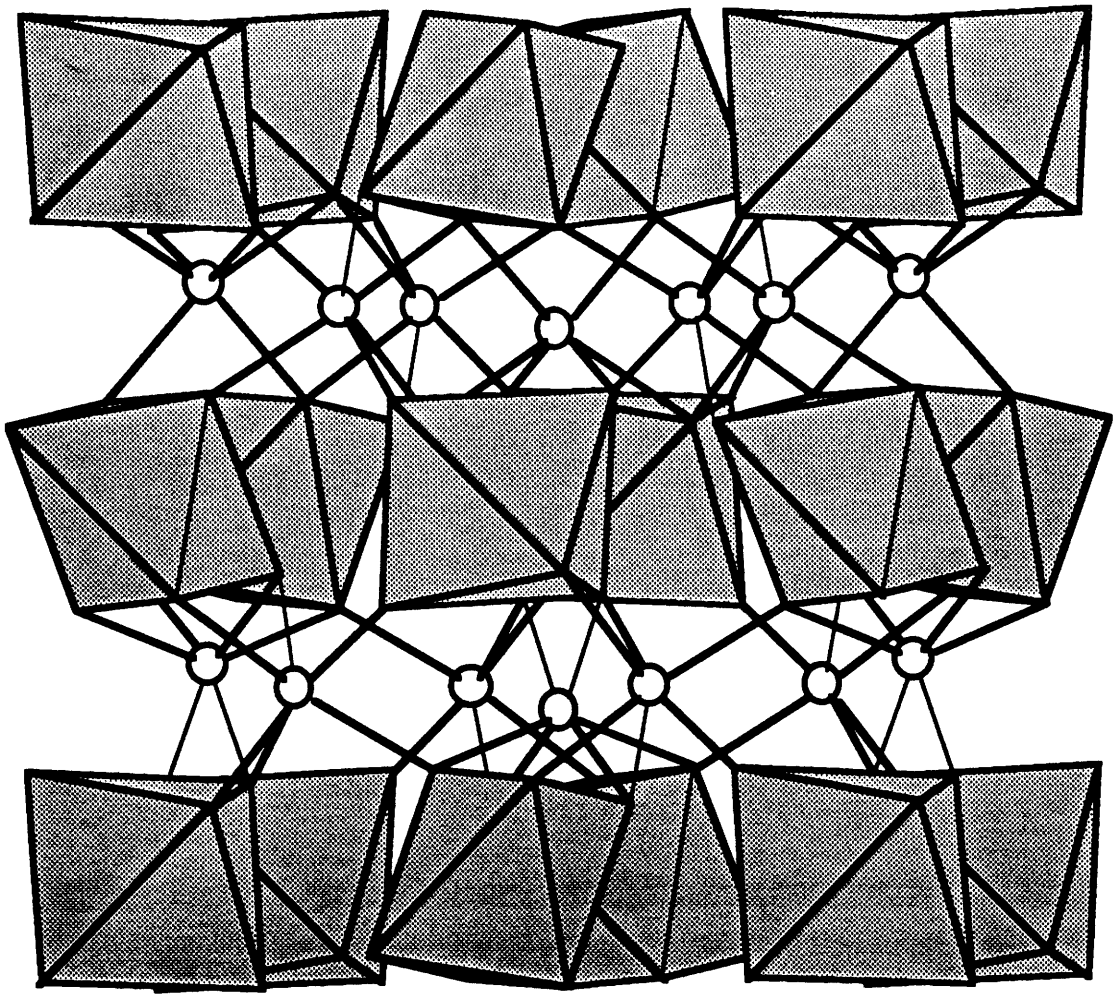

Figure 4.1.4 The bixbyite structure. One cation coordination site is represented as a circle and one cation coordination site is located at the center of the polyhedra. Oxygen atoms are located at the apices of the polyhedra.

that include structure-specific geometric arguments must be calculated. One such relationship is the Goldschmidt tolerance factor.[4]

$$t = \frac{(r_A + r_O)}{\sqrt{2}(r_B + r_O)}$$

The calculation of tolerance factors can be predictive as to which structure type should form. The Goldschmidt tolerance factor was calculated to determine the geometric constraints necessary for the formation of the perovskite structure. However, as previously mentioned, when the perovskite structure does not form, generally sesquioxide structures are stable. For example, for $1 > t > 0.8$, the perovskite structure should form, while for $0.8 \geq t$ the sesquioxide structures form. The radii used for these calculations, however, are very susceptible to coordination number. Consequently, the addition of pressure may increase the coordination of certain atoms and alter the stability range of a given structure type.

In the absence of applied pressure, combinations of many trivalent first row transition metal oxides, including those of iron(III) and manganese(III), and rare earth oxides form the orthorhombic or rhombohedral form of the perovskite structure as the thermodynamically stable phase.[11,29,48-56] The application of pressure enables smaller **A** cations, such as scandium and indium, to crystallize in the perovskite structure.[57-60] Low temperature, kinetic phases also exist, particularly for the rare earth manganates and the small rare earth ferrates,[51,61-69] where a hexagonal phase forms below 1000°C, but which converts to the perovskite structure at high temperatures and pressures. The rare earth aluminates form a different but related hexagonal phase[64,70] which also converts to the perovskite structure above 900°C.

Unlike the high temperature thermodynamic phases studied by Roth,[11,29] low temperature phases containing cations whose radius ratio places them near the bixbyite and ilmenite regions in the trivalent ABO_3 structural phase diagram (Figure 4.1.1) have been relatively unstudied. This middle region, where the radii of **A** and **B** are too different for the corundum structure to form, or where **A** is too small to form AO_3 layers, and yet too large to enter interstitial sites in closest-packed oxygen layers, can give rise to many interesting low temperature phases.[25,26,51,61-71] Due to the many competing interactions that determine the final structure for a given cation pair, kinetic factors can play a crucial role by favoring some of the interactions at the expense of others, thereby favoring structure types that might not form under strictly thermodynamic control.

D. Discussion of the $InMnO_3$ and $InFeO_3$ structure: Comparison with the related $YAlO_3$ structure

The structure of $InMO_3$ consists of alternating layers of octahedrally coordinated indium and trigonal bipyramidally coordinated transition metal atoms.[25,26] (Figure 4.1.5) The transition metal and indium coordinates are fixed by symmetry and, consequently, have ideal D_{3h} and near ideal octahedral symmetry, respectively. The indium is located in CdI_2-like[40] octahedral interstices between two closest-packed oxygen layers, resulting in edge-shared indium octahedra whose three-fold axis runs parallel to the **c**-direction of the hexagonal unit cell. The three-fold axis of the trigonal bipyramids also runs parallel to the **c**-direction in a staggered arrangement, such that transition metal layers repeat with every second layer.

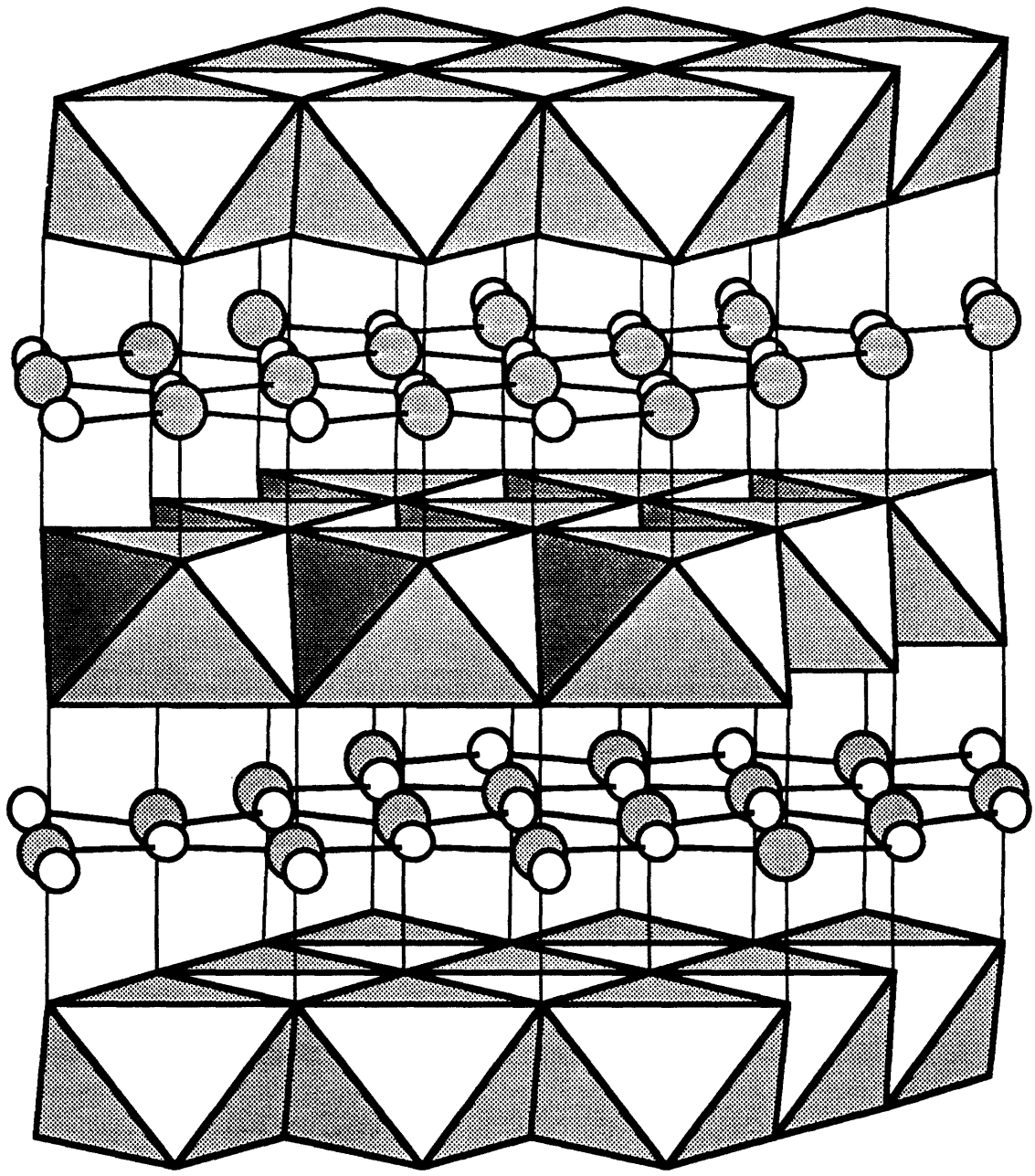

Figure 4.1.5 The $InMO_3$ structure. Indium atoms are located at the center of the polyhedra; the M atom site, M = Fe, Mn, is represented as a large circle at the center of a trigonal bipyramid of oxygen. Oxygen located with the plane of the M cation are represented as small open circles while the remainder of the oxygen atoms are located at the apices of the polyhedra.

There are unexpected structural differences between $InMnO_3$ and $InFeO_3$ which cannot be attributed to size or geometry arguments alone. According to Shannon's atomic radii tables,[72] the ionic radius of both Mn(III) and Fe(III) in five-fold coordination is 0.58 Å. Considering that the positions of the transition metal atoms and the indium atoms are fixed in x,y,z and considering that $InMnO_3$ is only slightly larger in the a-plane than $InFeO_3$, the fact that $InFeO_3$ is 0.7Å taller, 12.175Å *vs.* 11.475Å, in the z-direction may be due to electronic differences. This difference most likely results from the electronic configurations of high spin Mn(III), d^4, and high spin Fe(III), d^5, and the filling of the d_z^2 orbital. Since the symmetry of the transition metals is ideal D_{3h}, the energy levels of the 2:2:1 splitting of the d-orbitals must adapt to accommodate both d^4 and d^5 ions.(Figure 4.1.6) Consequently, the difference in c-axis lengths between the manganese and iron compounds can be explained by a weakening and elongation of the axial Fe-O bond to effect a lowering in the energy level of the d_z^2 orbital. This results in a Fe-O(1) distance that is 0.18Å longer than the corresponding Mn-O(1) distance, as well as an in-plane trigonal Fe-O(2) distance that is shorter than the apical Fe-O(1) distance in $InFeO_3$, while for $InMnO_3$ the opposite is true.

The difference between both $InMnO_3$ and $InFeO_3$, and the related $YAlO_3$[64,70] is even more dramatic. $YAlO_3$ is larger than $InMnO_3$ in the a-plane, 3.678 Å *vs.* 3.398 Å, however, the c-parameter is dramatically shorter, 10.52Å *vs.* 11.48Å. The Al-O bond lengths in $YAlO_3$ are surprisingly similar to the Fe-O bonds found in $InFeO_3$, *i.e.* short apical bonds and long in-plane bonds, even though the c-axis is almost 2 Å shorter, 10.52Å *vs.* 12.18Å. The in-plane trigonal Al-O distances are 2.12Å, while the apical Al-O distances are 1.82Å. The contraction

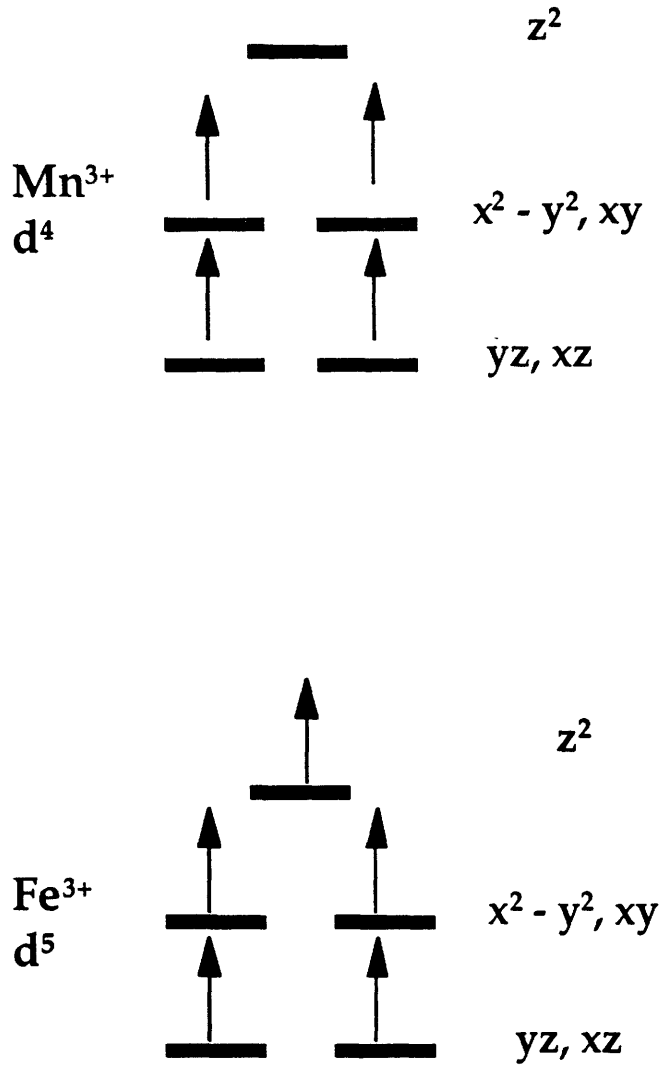

Figure 4.1.6 *d*-orbital splitting patterns for ideal D_{3h} trigonal bipyramidal symmetry for Mn(III), d^4, and Fe(III), d^5.

of the **c**-axis in $YAlO_3$ seems to be related to the coordination of the rare earth atom. Yttrium increases its coordination from 6- to 8-fold coordination because the **z**-axis contraction enables the yttrium to bond with two additional next-nearest neighbor oxygens. In the case of indium, however, this contraction is not necessary as indium is content in 6-fold coordination and the oxygen atoms in question are beyond the combined van der Waals radii of indium and oxygen. This contraction is a function of the rare earth atom in the **A**-site, and consequently, the **A**-cation coordination in $InMO_3$ different than $YAlO_3$ and $YFeO_3$.[73] The only reported isostructural material is $InGaO_3$,[71] a high pressure phase.

E. Discussion of the $A^{3+}B^{3+}O_3$ structural phase diagram

The Goldschmidt tolerance factor, **t**, calculated for $InMnO_3$ and $InFeO_3$ is 0.8, placing these compounds at the border of the perovskite, the corundum/ilmenite and the bixbyite structures. Size and ionicity arguments are presented to rationalize the existence of these phases, as well as to predict other $\mathbf{ABO_3}$ materials which may form with this hexagonal structure type. According to the existing structural phase diagram for trivalent $\mathbf{ABO_3}$ compounds (Figure 4.1.1), these unusual hexagonal phases are unexpected. Furthermore, there are other low temperature hexagonal phases that cannot be accommodated in the high temperature $\mathbf{ABO_3}$ phase diagram, namely rare earth manganates, ferrates, and chromates with the related $LuMnO_3$ structure.[51,61-69]

The $LuMnO_3$ structure, (Figure 4.1.7) unlike $InMnO_3$ or $InFeO_3$, has a very distorted trigonal bipyramidal coordination site and, consequently, can accommodate Jahn-Teller ions such as Cr(III) d^3, which are not electronically

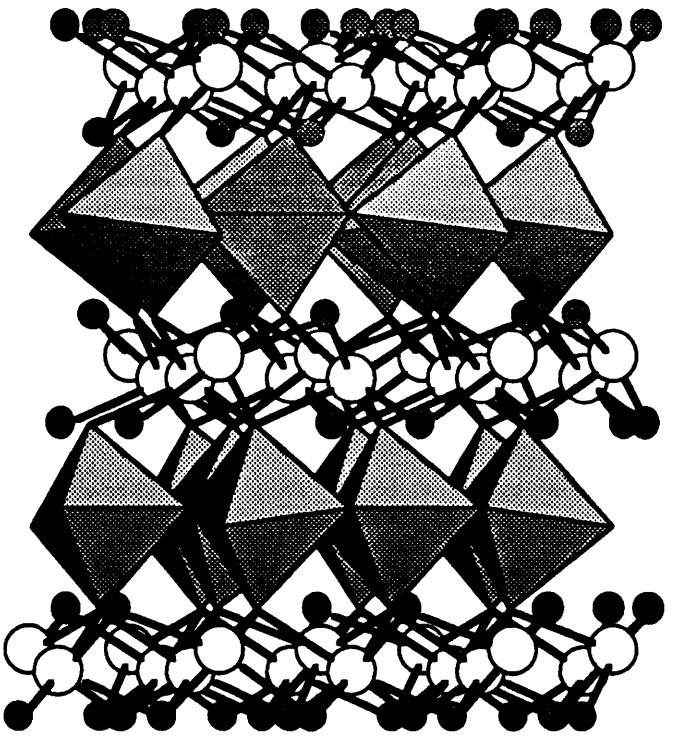

Figure 4.1.7 The structure of $LuMnO_3$. The rare earth atoms are 7-coordinate and are represented as white circles. The manganese atoms are in distorted trigonal bipyramidal coordination, represented as polyhedra. Oxygen atoms are represented as shaded circles and are located at the apices of polyhedra.

allowed in the ideal D_{3h} coordination site in the $InMO_3$ structure. The fact that Mn(III) also exists in this distorted configuration suggests the presence of mixed valency for manganese, a possibility that has been previously suggested.[69,74] Compounds having the $LuMnO_3$ structure convert to either the orthorhombic or rhombohedral distortion of the perovskite structure above 1000°C, unlike both $InMnO_3$ and $InFeO_3$, which decompose to binary oxides. Perhaps In(III) is too small to allow the transformation into the perovskite structure with Mn(III) and Fe(III) at ambient pressure. Perovskite compounds of iron and manganese usually have a tolerance factor of 0.89, while the indium-transition metal oxides have tolerance factors of 0.79. If the radii of indium and iron or manganese were much closer, either the corundum structure or the bixbyite structure might crystallize. As they are, however, the small tolerance factor of indium with most 3+ transition metals precludes both the corundum and the perovskite structure from forming except under high pressure. At high temperatures and pressures, the stability range of the perovskite structure is increased, allowing some compounds to be stable, *e.g.* $InRhO_3$,[60] which under pressure crystallizes in the perovskite structure even though t = 0.80.

A modification of the structural phase diagram used by Roth is presented in Figure 4.1.8 and a general structure map of the $\mathbf{ABO_3}$ phase diagram is presented in Figure 4.1.9. Rather than simply plotting the radius of **A** *vs.* **B**, the axes are modified to include the bond ionicities of the **A** and **B** cations. As shown by Mooser and Pearson,[8] the bond ionicity can be modeled by the difference in the electronegativity of **A** and **B**. Accommodating $\mathbf{ABO_3}$ compounds necessitates the plotting of parameters associated with the character of **A-O** bonding *vs.* parameters associated with the character of **B-O**

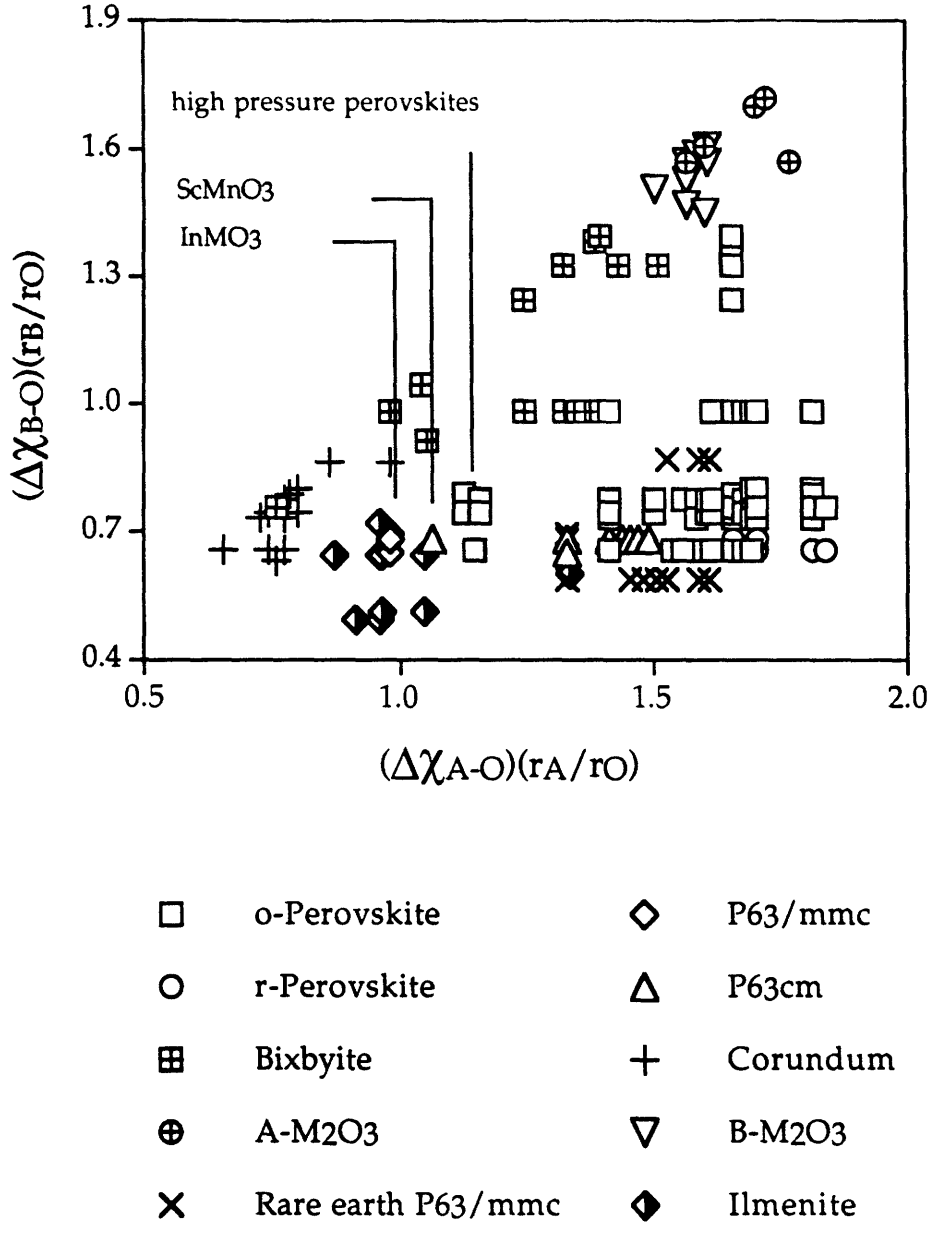

Figure 4.1.8 Ionicity graph of the ABO_3 structural phase diagram for common structure types of the compounds listed in Table 4.1.1.

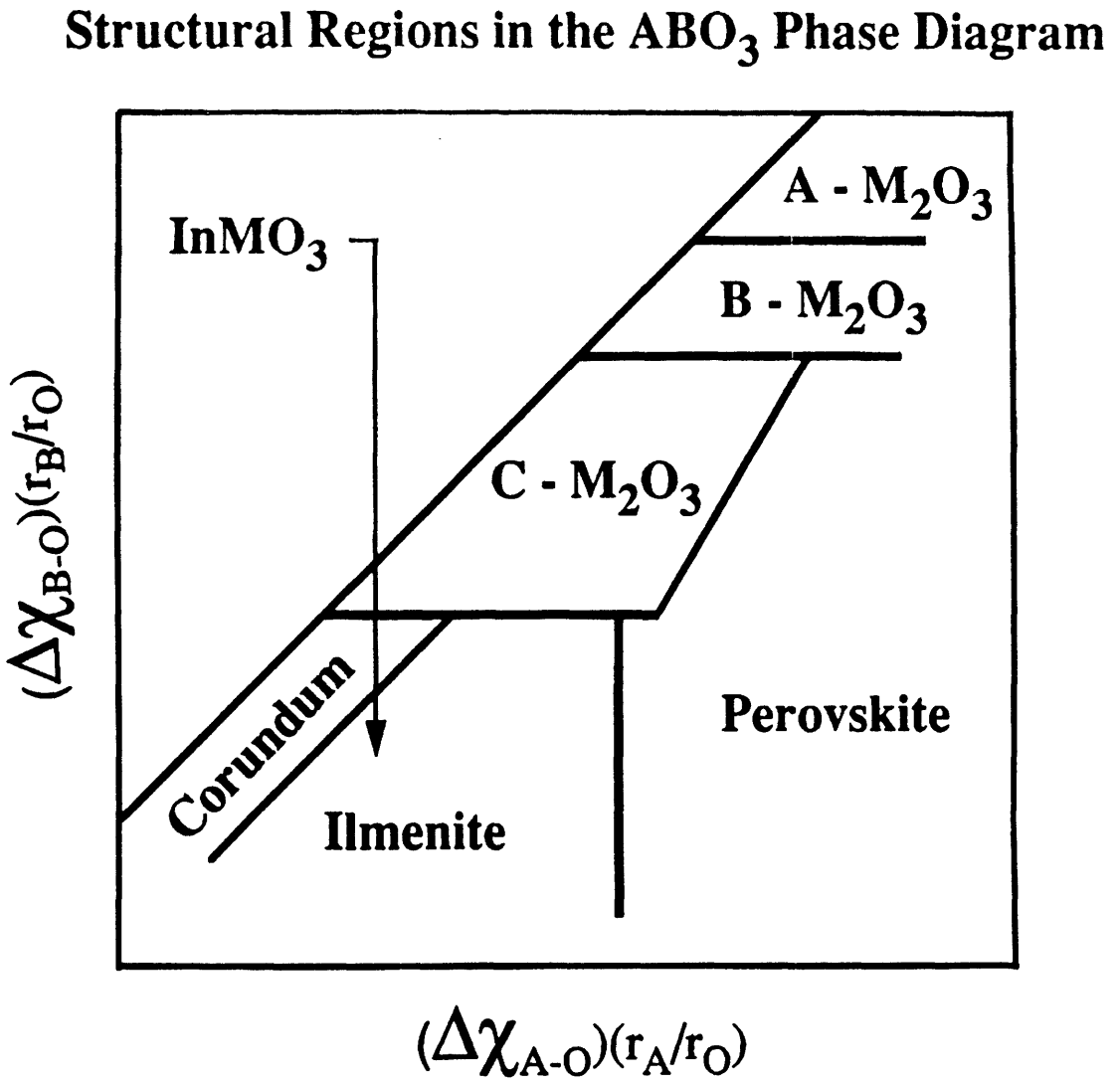

Figure 4.1.9 Structural regions within the ABO_3 phase diagram.

bonding. The approach used by Roth, while quite successful in predicting the most common structure types, is able neither to predict the $InMO_3$-type structures nor to accommodate materials such as those with the $LuMnO_3$ structure which convert to the perovskite structure at high temperatures. Using the difference in electronegativity of **A-O** and **B-O** and multiplying them by r_A/r_O and r_B/r_O, respectively, introduces the concept of bond ionicity into the Figure 4.1.8, and possibly generalizes this concept for materials with anions other than oxygen, *e.g.* nitrides, chalcogenides, or halides.

It has been argued for intermetallic systems that it is not possible to accurately differentiate between structure types using less than three dimensional plots.[1] In case of ABO_3 structures, however, it is possible to use two-dimensional structure-composition diagrams. To include quaternary systems, such as $ABCO_x$, on the other hand, a three-dimensional diagram would undoubtedly achieve better structural separation than an averaged two-dimensional one.

The distribution of structures in Figures 4.1.8 and 4.1.9 show the corundum region well separated from the bixbyite region and both apart from the perovskite region. Unlike Figure 4.1.1, where $InMnO_3$ and $InFeO_3$ fall too close to the corundum and bixbyite regions to be distinguished based on their radii alone, in Figure 4.1.8, the $InMO_3$ structure type is clearly within the ilmenite region. Thus, by combining the bond ionicities with the cation ratios, we see that an $A^{3+}B^{3+}O_3$ phase which according to size and ionicity ratios, falls into the $A^{2+}B^{4+}O_3$ ilmenite region requires a new structure type to gain stability. Apparently, in the intermediate regime where the **A** cation fits into the bixbyite region and the **B** cation into the corundum structure, conditions are favorable for the formation of the $InMO_3$ structure. The

segregation of compounds in this manner is possible only through the use of oxidation state-specific electronegativities. Using only ionic radii, the $InMO_3$ structures do not fit into the ilmenite structural region, Figure 4.1.1. The combination of size and electronegativity, however, places the $InMO_3$ materials squarely within the ilmenite region.

The $InMnO_3$ structure is separated from the perovskite region by other compounds having unexpected structures, including $ScMnO_3$ and perovskites such as $InRhO_3$, which can only be synthesized at high pressures to force indium to take on a coordination higher than six. The perovskite region in the ionicity diagram appears quite complicated, however, it should be noted that all of the non-perovskite phases which appear in the perovskite region will convert to the perovskite structure at high temperatures, *e.g.* $LuMnO_3$ and rare earth aluminate phases.

It should be noted that for compounds in which both the **A** and **B** cations are rare earth elements, the ionicity structure map is no longer useful. (See rare earth regions in Figure 4.1.1 and 4.1.8) In this case the use of only ionic radii and radius ratio rules is more advantageous for structural prediction. This is due to the fact that unlike both the *d*-block and the *p*-block elements, the electronegativity of the *f*-block elements does not change regularly as one goes from the left side of the periodic table to the right. Instead, the electronegativities of the rare earth elements fluctuate across the row and because of this, the addition of electronegativity to ionic radii cancels out changes that occur in the ionic radii (the lanthanide contraction) across the periodic table. Consequently, use of ionicity to predict the structure of solely *f*-block compounds is not advantageous.

The most useful information is obtained by using the bond ionicity diagram (Figure 4.1.8) in conjunction with the ionic radii diagram (Figure 4.1.1). The diagram constructed from only ionic radii is quite successful in segregating the major structure types into general areas, particularly for high temperature phases. The bond ionicity diagram (Figure 4.1.8) complements the ionic radii diagram with features that the ionic radii diagram lacks. Specifically, certain structural areas are more effectively separated in the ionicity diagram, *e.g.* the corundum region and the ilmenite region. The ionicity diagram also places low temperature structures and exceptional structures closer to their expected locations, *e.g.* the (RE)AlO_3 structures, high pressure perovskites, and $ScMnO_3$.

The utility of structure-composition diagrams, such as the diagrams shown in Figures 4.1.1 and 4.1.8, lies not so much in the rationalizing of existing structures, but rather in predicting the structures of new compositions. For example, based on the diagrams shown in Figures 4.1.1 and 4.1.8, it becomes possible to predict other phases which may crystallize in the $InMO_3$ structure. Considering both the geometric and electronic requirements of the $InMO_3$ materials *vide supra*, several other compounds may be stable in this structure. For example, $InVO_3$ containing V(III) d^2, which is not a Jahn-Teller ion in D_{3h} symmetry, and $InRhO_3$, containing low-spin Rh(III), may both expected to form in the $InMO_3$ structure type. Compounds containing Ni(III) in the **B**-cation site are electronically feasible as well. Also, compounds in which scandium or gallium has replaced indium may crystallize in this structure type provided that the proper synthetic techniques are employed. The proximity of the $InMO_3$ structure to the corundum, bixbyite, and perovskite structures emphasizes the delicate nature of the low temperature

synthesis which must be performed in order to favor the $InMO_3$ structure over other possibilities.

F. Conclusions

The structures of $InMnO_3$ and $InFeO_3$ are unusual and unexpected within the context of the common $\mathbf{ABO_3}$ structure types. Using a new method for structural prediction which combines bond ionicities with ionic radii, the $\mathbf{ABO_3}$ structural phase diagram has been reanalyzed, and the $InMO_3$ structure has been shown to appear in the $\mathbf{A^{2+}B^{4+}O_3}$ ilmenite structural region along with several other unusual $\mathbf{A^{3+}B^{3+}O_3}$ materials. The new method, together with previously described methods, enable the researcher to obtain some predictive intuition regarding new structures in the $\mathbf{ABO_3}$ structural phase diagram. Several new materials with the $InMO_3$ structure were predicted.

TABLE 4.1.1

Examples of the Common Structures in the ABO_3 Phase Diagram

o-perovskite	reference	$P6_3/mmc$	reference
$PrScO_3$	(29)	$InGaO_3$	(71)
$NdScO_3$	(29)	$InFeO_3$	(26)
$GdScO_3$	(29)	$InMnO_3$	(25)
$ScAlO_3$	(59)		
$YGaO_3$	(57)		
$InRhO_3$	(60)	r-perovskite	reference
$LaMnO_3$	(68)		
$YAlO_3$	(52)	$LaAlO_3$	(49)
$EuAlO_3$	(49)	$LaGaO_3$	(53)
$GdAlO_3$	(49)	$CeAlO_3$	(29)
$TmAlO_3$	(29)	$PrAlO_3$	(49)
$DyAlO_3$	(29)	$NdAlO_3$	(49)
$HoAlO_3$	(29)	$LaNiO_3$	(48)
$ErAlO_3$	(29)	$NdNiO_3$	(77)
$YMnO_3$	(50)	$SmAlO_3$	(53)
$YFeO_3$	(52)		
$LaFeO_3$	(29)		
$YCrO_3$	(52)	$P6_3cm$	reference
$GdFeO_3$	(29)		
$EuFeO_3$	(29)	$YMnO_3$	(67)
$SmFeO_3$	(29)	$ScMnO_3$	(65)
$NdFeO_3$	(29)	$LuMnO_3$	(67)
$PrFeO_3$	(29)	$TmMnO_3$	(67)
$LaCrO_3$	(29)	$ErMnO_3$	(67)
$PrCrO_3$	(29)	$YGaO_3$	(66)
$NdCrO_3$	(29)	$HoMnO_3$	(67)
$LaGaO_3$	(29)	$YbMnO_3$	(67)
$PrGaO_3$	(29)		
$NdGaO_3$	(29)		
$GdVO_3$	(53)	bixbyite	reference
$NdVO_3$	(53)		
$PrVO_3$	(53)	$ScFeO_3$	(29)
$YScO_3$	(53)	Sc_2O_3	(59)
$SmAlO_3$	(49)	Y_2O_3	(59)
$SmCrO_3$	(29)	Mn_2O_3	(59)
$LaInO_3$	(29)	In_2O_3	(59)
$NdInO_3$	(29)	Tl_2O_3	(59)
$SmInO_3$	(29)	$YScO_3$	(29)

TABLE 4.1.1 cont.

o-perovskite	reference
$EuCrO_3$	(29)
$GdCrO_3$	(29)
$DyCrO_3$	(29)
$ErCrO_3$	(29)
$LuCrO_3$	(29)
$DyFeO_3$	(29)
$HoFeO_3$	(29)
$ErFeO_3$	(29)
$YbFeO_3$	(29)
$LuFeO_3$	(29)
$LaScO_3$	(29)
$SmScO_3$	(29)
$EuScO_3$	(29)
$DyScO_3$	(29)
$LaErO_3$	(27)
$LaTmO_3$	(27)
$LaYbO_3$	(27)
$LaLuO_3$	(27)
$LaRhO_3$	(76)
$NdRhO_3$	(75)
$LaYO_3$	(11)
$DyInO_3$	(60)
$TlFeO_3$	(60)
$TlCrO_3$	(60)
$GdInO_3$	(60)
$EuInO_3$	(60)
$YInO_3$	(60)
$InCrO_3$	(60)
$YbGaO_3$	(57)
$GdGaO_3$	(57)
$CeMnO_3$	(68)
$PrMnO_3$	(68)
$NbMnO_3$	(68)
$SmMnO_3$	(68)

A-M_2O_3	reference
Ce_2O_3	(27)
Pr_2O_3	(27)
Nd_2O_3	(27)
$LaSmO_3$	(28)

bixbyite	reference
$ErScO_3$	(29)
$YbScO_3$	(29)
$ScInO_3$	(29)
$HoInO_3$	(29)
$ErInO_3$	(29)
$TmInO_3$	(29)
$YbInO_3$	(29)
$YInO_3$	(11)
$LuScO_3$	(29)
$LuInO_3$	(29)
Lu_2O_3	(27)
Yb_2O_3	(27)
Ho_2O_3	(27)
$GdLuO_3$	(28)
$DyLuO_3$	(28)

corundum	reference
V_2O_3	(40)
Cr_2O_3	(40)
Fe_2O_3	(40)
Rh_2O_3	(40)
Al_2O_3	(40)
Ga_2O_3	(40)
$CrAlO_3$	(29)
$FeCrO_3$	(29)
$FeAlO_3$	(11)
$AlGaO_3$	(11)
$CrVO_3$	(56)
$GaFeO_3$	(29)
Ti_2O_3	(40)
$InTiO_3$	(56)

B-M_2O_3	reference
Eu_2O_3	(27)
Gd_2O_3	(27)
$LaGdO_3$	(28)
Sm_2O_3	(27)
$LaDyO_3$	(28)

TABLE 4.1.1 cont.

A-M_2O_3	reference	B-M_2O_3	reference
La_2O_3	(27)	$LaHoO_3$	(28)
		$NdErO_3$	(28)

RareEarth $P6_3/mmc$	reference	Ilmenite	reference
$YAlO_3$	(70)	$CdTiO_3$	(58)
$EuAlO_3$	(70)	$CdSnO_3$	(58)
$GdAlO_3$	(70)	$NiMnO_3$	(58)
$TbAlO_3$	(70)	$MgGeO_3$	(58)
$DyAlO_3$	(70)	$CoMnO_3$	(58)
$HoAlO_3$	(70)	$NiTiO_3$	(58)
$ErAlO_3$	(70)	$MgTiO_3$	(58)
$EuInO_3$	(61)	$FeTiO_3$	(58)
$GdInO_3$	(61)	$MnGeO_3$	(58)
$DyInO_3$	(61)	$MnTiO_3$	(58)
$YMnO_3$	(62)		
$YFeO_3$	(73)		

References

(1) Kiselyova, N. N. MRS Bulletin (1993) **18**, 40.

(2) Adams, D. M. *Inorganic Solids*; John Wiley & Sons: London, 1974; Vol. Ch. 5 p.105.

(3) Brewer, L. Science (1968) **161**, 115.

(4) Goldschmidt, V. M. Mat.-Naturv. Kl. (1926) **2**, 117.

(5) Gorter, E. W. J. Solid State Chem. (1970) **1**, 279.

(6) Hume-Rothery, W. *Electrons, Atoms, Metals and Alloys*; 3rd ed.; Dover: New York, 1963.

(7) Laves, F. *Theory of Alloy Phases*; American Society for Metals: Cleveland, 1955; Vol. p. 124.

(8) Mooser, E.; Pearson, W. B. Acta Crystallogr. (1959) **12**, 1015.

(9) Phillips, J. C.; Van Vechten, J. A. Phys. Rev. B (1970) **2**, 2147.

(10) Phillips, J. C. Rev. Mod. Phys. (1970) **42**, 317.

(11) Roth, R. S. J. Research NBS (1957) **58**, 75.

(12) Van Vechten, J. A. Phys. Rev. (1969) **187**, 1007.

(13) Van Vechten, J. A.; Phillips, J. C. Phys. Rev. B (1970) **2**, 2160.

(14) Villars, P. J. Less Common-Met. (1986) **119**, 175.

(15) Villars, P.; Hulliger, F. J. Less-Common Met. (1987) **132**, 289.

(16) Villars, P.; Mathis, K.; Hulliger, F. In *Structures of Binary Compounds*; F. de Boer and D. Pettifor, Ed.; North-Holland: Amsterdam, 1989; Vol. 2.

(17) Villars, P.; Phillips, J. C.; Rabe, K. M.; Brown, I. D. Ferroelectrics (1992) **130**, 129.

(18) Greenwood, N. N. *Ionic Crystals, Lattice Defects, and Nonstoichiometry*; Butterworths: London, 1968.

(19) Orgel, L. E. *Transition-Metal Chemistry: Ligand-Field Theory*; Methuen: London, 1963.

(20) Villars, P. J. Less-Common Met. (1983) **92**, 215.

(21) Martynov, A. I.; Batsanov, S. S. Russ. J. Inorg. Chem. (1980) **25**, 1737.

(22) Villars, P. J. Less Common-Met. (1984) **102**, 199.

(23) Villars, P. J. Less-Common Met. (1984) **99**, 33.

(24) Zunger, A. In *Structure and Bonding in Crystals*; M. O'Keefe and A. Navrotsky, Ed.; Academic Press: New York, 1981.

(25) Giaquinta, D. M.; zur Loye, H.-C. J. Amer. Chem. Soc. (1993) **114**, 10952.

(26) Giaquinta, D. M.; Davis, W. M.; zur Loye, H.-C. Acta Crystallogr. (1993) **C49**, in press.

(27) Roth, R. S.; Schneider, S. J. J. Research NBS (1960) **64A**, 309.

(28) Schneider, S. J.; Roth, R. S. J. Research NBS (1960) **64A**, 317.

(29) Schneider, S. J.; Roth, R. S.; Waring, J. L. J. Research NBS (1961) **65A**, 345.

(30) Galasso, F. S. *Structure, Properties and Preparation of Perovskite Type Compounds*; Pergamon Press: Oxford, 1969.

(31) Goodenough, J. B.; Longo, J. M. *Landolt-Bornstein Tabellen, New Series, III*; 1970; Vol. 4a.

(32) Goodenough, J. B. Prog. in Solid State Chem. (1971) **5**, 145.

(33) Smyth, D. M. Ann. Rev. Mater. Sci. (1985) **15**, 329.

(34) Rao, C. N. R. Annu. Rev. Phys. Chem. (1989) **40**, 291.

(35) Yakel Jr., H. L. Acta Crystallogr. (1955) **8**, 394.

(36) Mouron, P.; Choisnet, J.; Abs-Wurmach, I. Eur. J. Solid State Inorg. Chem. (1989) **26**, 35.

(37) Norrestam, R. Acta Chem. Scand. (1967) **21**, 2871.

(38) Newnham, R. E.; Fang, J. H.; Santoro, R. P. Acta Crystallogr. (1964) **17**, 240.

(39) Chamberland, B. L.; Sleight, A. W.; Weiher, J. R. J. Solid State Chem. (1970) **1**, 512.

(40) Wells, A. F. *Structural Inorganic Chemistry;* 5th ed.; Clarendon Press: Oxford, 1984.

(41) Takeda, Y.; Kanamaru, F.; Shi Madra, M.; Koizumi, M. Acta Crystallogr. (1976) **B32**, 2464.

(42) Burbank, R.; Evans Jr., H. Acta Crystallogr. (1948) **1**, 330.

(43) Longo, J. M.; Raccah, R. M.; Goodenough, J. B. Mater. Res. Bull. (1969) **4**, 191.

(44) Hong, H. Y.; Kafalas, J. A.; Goodenough, J. B. J. Solid State Chem. (1974) **9**, 345.

(45) Goodenough, J. B.; Kafalas, J. A. J. Solid State Chem. (1973) **6**, 493.

(46) Geller, S.; Curlander, P. J.; Jefferies, J. B. Acta Crystallogr. (1975) **B31**, 2770.

(47) *Structure Reports*; Hermann, C.; Lohrmann, O.; Philipp, H., Ed.; Verlag: Leipzig, 1928-1932; Vol. 2, p. 38.

(48) Wold, A.; Post, B.; Banks, E. J. Amer. Chem. Soc. (1957) **79**, 4911.

(49) Geller, S.; Bala, V. B. Acta Crystallogr. (1956) **9**, 1019.

(50) Wood, V. E.; Austin, A. E.; Collings, E. W.; Brog, K. C. J. Phys. Chem. Solids (1973) **34**, 859.

(51) Quezel, S.; Rossat-Mignod, J.; Bertaut, E. F. Solid State Comm. (1974) **14**, 941.

(52) Geller, S.; Wood, E. A. Acta Crystallogr. (1956) **9**, 563.

(53) Geller, S. Acta Crystallogr. (1957) **10**, 243.

(54) Dalziel, J. A. W. J. Chem. Soc. (1959) 1993.

(55) Wood, E. A. Acta Crystallogr. (1951) **4**, 353.

(56) Keith, M. L.; Roy, R. Amer. Mineral. (1954) **39**, 1.

(57) Marezio, M.; Remeika, J. P.; Dernier, P. D. Mat. Res. Bull. (1966) **1**, 247.

(58) Reid, A. F.; Ringwood, A. E. J. Geophys. Res. (1969) **74**, 3238.

(59) Reid, A. F.; Ringwood, A. E. J. Geophys. Res. (1975) **80**, 3363.

(60) Shannon, R. D. Inorganic Chemistry (1967) **6**, 1474.

(61) Schneider, S. J. J. Research NBS (1961) **65A**, 429.

(62) Lukaszewicz, K.; Karut-Kalicinska, J. Ferroelectrics (1974) **7**, 81.

(63) Koehler, W. C.; Yakel, H. L.; Wollan, E. O.; Cable, J. W. Phys. Lett. (1964) **9**, 93.

(64) Bertaut, E. F.; Buisson, G.; Durif, A.; Mareschal, J.; Montmory, M. C.; Quezel-Ambrunaz, S. B. S. chim. Fr. (1965) 1132.

(65) Komissarova, L. N.; Pokrovskii, B. I.; Shaplygin, I. S. Neorg. Mater. (1966) **2**, 275.

(66) Geller, S.; Jeffries, J. B.; Curlander, P. J. Acta Crystallogr. (1975) **B31**, 2770.

(67) Bertaut, E. F.; Mercier, M.; Pauthenet, R. J. Physique (1964) **25**, 550.

(68) Pauthenet, R.; Veyret, C. J. Physique (1970) **31**, 65.

(69) Yakel, H. L.; Koehler, W. C.; Bertaut, E. F.; Forrat, E. F. Acta Crystallogr. (1963) **16**, 957.

(70) Bertaut, F.; Mareschal, J. Compt. rend. (1963) **275**, 867.

(71) Shannon, R. D.; Prewitt, C. T. J. Inorg. Nucl. Chem. (1968) **30**, 1389.

(72) Shannon, R. D. Acta Crystallogr. (1976) **A32**, 751.

(73) Yamaguchi, O.; Takemura, H.; Yamashita, M. J. Electrochem. Soc. (1991) **138**, 1492.

(74) Gallagher; McCarthy; Penn State University, JCPDS Grant-in-Aid-Report (1973).

(75) Wold, A.; Arnott, R. J.; Croft, W. Inorganic Chemistry (1963) **2**, 972.

(76) Wold, A.; Post, B.; Banks, E. J. American Chem. Soc. (1957) **79**, 6365.

(77) Vassiliou, J. K.; Hornbostel, M.; Ziebarth, R.; DiSalvo, F. J. J. Solid State Chem. (1989) **81**, 208.